Thermal and State-of-Charge Balancing of Batteries using Multilevel Converters

Faisal Altaf

Thermal and State-of-Charge Balancing of Batteries using Multilevel Converters
Faisal Altaf

Department of Signals and Systems
Chalmers University of Technology
SE–412 96 Göteborg
Sweden

Telephone: +46 (0)31 – 772 1000

Email: faisal.altaf@chalmers.se

To my whole family

Abstract

Driven by the needs to reduce the dependence of fossil fuels and the emissions of conventional vehicles there has in recent years been an increasing interest in battery-powered electrified vehicles (xEVs). In xEVs, the battery pack, built from many small cells, is one of the most expensive components in the powertrain. As a result, the battery lifetime is an important factor for the success of xEVs. However, the battery pack lifetime is severely affected by the State-of-Charge (SOC) and thermal imbalance among its cells, which is inevitable in large automotive batteries. Therefore, thermal and SOC balancing is quite important to enhance their life-time.

In this thesis, the use of a multi-level converter (MLC) as an integrated cell balancer and motor driver is investigated for application in xEVs. The MLC has a special modular structure which distributes a large battery pack into smaller units, enabling an independent cell-level control of a battery system. This extra degree-of-freedom enables the potential non-uniform use of cells, which along with brake regeneration phases in the drive cycle is exploited by MLC to achieve simultaneous thermal and SOC balancing.

An MLC-based optimal control policy (OP) has been formulated, assuming dc machine as a load, which uses each cell in a battery submodule according to its SOC and temperature to achieve thermal and SOC balancing by optimally redistributing the power losses among the cells. Results show that OP reduces temperature and SOC deviations significantly compared with the uniform use of all cells.

However, in applications involving three-phase ac machine, the MLC, in addition to its great balancing potential, also poses serious issues of extra battery heating and of extra ampere-hour throughput due to dc-link current ripple. These extra effects may accelerate the battery ageing if not compensated. A simple passive compensation method based on dc-link capacitor has been investigated, but it turns out that the size of the required capacitor is too big for automotive applications. Thus, it is concluded that, from battery's health viewpoint, it is unpromising to promote 3-ϕ MLC as an integrated cell balancer and a motor driver in xEVs, unless some other more advanced active compensation technique is used.

Keywords: Multilevel converter, Battery control, Cell balancing, Thermal balancing, Convex optimization, Battery ripple, Hybrid electric vehicles.

ii

Acknowledgments

List of publications

This thesis is based on the following appended papers:

Paper 1

F. Altaf, L. Johannesson, B. Egardt, "On Thermal and State-of-Charge Balancing using Cascaded Multi-level Converters," *Journal of Power Electronics*, vol. 13, Issue 4, pp. 569-583, 2013.

Paper 2

F. Altaf, L. Johannesson, B. Egardt, "Feasibility Issues of using Three-Phase Multilevel Converter based Cell Balancer in Battery Management System for xEVs," In *IFAC Symposium on Advances in Automotive Control*, pp. 390-397, Sep. 2013, Tokyo.

Other publications

In addition to the appended papers, the following papers by the thesis author are related to the topic of the thesis but not included:

Faisal Altaf, Lars Johannesson, and Bo Egardt. "Evaluating the Potential for Cell Balancing Using a Cascaded Multi-Level Converter Using Convex Optimization," In *IFAC Workshop on Engine and Powertrain Control, Simulation and Modeling*, vol. 3, no. 1, pp. 100-107, Oct. 2012, Paris.

Faisal Altaf, Lars Johannesson, and Bo Egardt. "Performance Evaluation of Multilevel Converter based Cell balancer with Reciprocating Air Flow," In *Vehicle Power and Propulsion Conference (VPPC), 2012 IEEE*, pp. 706-713, 9-12 Oct. 2012, Seoul.

vi

Contents

II   Included papers

Part I

Introductory chapters

Chapter 1

Introduction

The discovery of fossil fuel in the late 19th century and the emergence of the internal combustion engine (ICE) as a dominant design for automobiles and industrial machines played a major role in significantly increasing CO_2 emissions into the environment during 20th century. There is now a consensus about the negative impact of carbon emissions on the globe's temperature. Thus, driven by the needs to reduce the dependence of fossil fuels and the environmental impact of transportation, many alternative technologies are being investigated today for future transportation. These alternatives primarily include battery powered electrified vehicles, hydrogen-powered ICE vehicles, fuel-cell powered electric vehicles, bio-fuels and solar-powered vehicles. All of these have their own pros and cons, but they are all strong competitors. The tank-to-wheel emission of all these designs is significantly lower than conventional ICE-based automobiles, but the big question in all these designs is the well-to-wheel emissions. All the processes involved in the development of these vehicles should be environmentally clean in order to categorize them as pure green cars, but unfortunately we have not come this far yet.

1.1 Electric Vehicles and Batteries

There has in recent years been an increasing interest in battery-powered electrified vehicles. The battery is a key component in these vehicles which helps to downsize or completely eliminate the ICE and may contribute to save fuel cost and reduce emissions. In a conventional vehicle, the kinetic (when going downhill) and braking energies of a vehicle get wasted. However, instead of wasting, the battery-powered electrified vehicles store these regenerative energies in the battery and use it later for the propulsion. Thus, the electrification of transportation is believed to have a positive social im-

pact due to significant economic and environmental benefit.

There are various kinds of electrified vehicles, namely pure electric vehicles (EVs), hybrid electric vehicles (HEV) and plug-in hybrid electric vehicles (PHEV). The EV is purely electric without ICE, whereas HEVs and PHEVs use both electric machine (EM) and ICE in a blended fashion to power the wheels. The PHEV has one extra feature: it can be charged from the grid. The mild electrification of vehicles ((P)HEVs) may not be a long-term solution because of their dependence on fossil fuel which, according to some predictions, will become very scarce by 2050. However, they can definitely be advocated as a viable solution during a transition phase between fossil fuel era and post fossil fuel era. The (P)HEVs are, currently, more sustainable designs compared to EVs, which are facing some serious issues due to immaturity of battery technology, resulting in a lower life-time and short electric-range problems. In EVs/HEVs/PHEVs (xEVs), the battery pack, built from many small cells, is one of the most expensive components in the powertrain, contributing largely to the total vehicle cost. As a result, the battery lifetime is an important factor for the success of xEVs. Thus, enhancing the life-time of large battery pack in xEVs using *active control* and *performance optimization* of the *battery system* will contribute, at least for a short and intermediate term, to achieve the common goal of cleaner environment and enhanced utility while reducing the consumption of natural resources for sustainable future.

This thesis deals with the topic of *cell balancing in large battery packs* which is an important topic in the emerging area of *battery system and control* [1]. The battery pack lifetime is severely affected by the State-of-Charge (SOC) and thermal imbalance among its cells. Therefore, to ensure the uniform life-time of all cells in a large battery pack, it is important for the battery management system to utilize each cell so that the SOC and temperature of the cells remain almost balanced. SOC balancing can be achieved using various types of dedicated SOC balancers [2], whereas thermal balancing can be achieved using reciprocating coolant flow as suggested in [3]. However, in this thesis, we particularly aim to investigate the performance of a certain power electronic topology, known as cascaded h-bridge multi-level converter (CHB-MLC), as an *integrated cell balancer and motor driver*. The purpose is to drive an electric machine and to achieve simultaneous thermal and SOC balancing using single hardware. The MLC has a special modular structure which distributes a large battery submodule (BSM) into smaller cells and thus enables the independent cell-level control of the BSM. This investigation highlights the potentials and pitfalls of this modular topology for a BSM. The *maximum potential* of MLC-based cell balancer, in a dc machine application, has been evaluated in Paper 1 by

devising an optimal control policy using convex optimization approach. In applications involving three-phase ac machines, the MLC due to its modularity generates a low frequency dc-link current ripple. This poses *serious issues* of extra battery heating and of extra ampere-hour throughput. These issues have been investigated in detail in Paper 2 and Appendix A.

1.2 Need of Thermal and SOC Balancing

The battery pack of xEVs consists of long strings of hundreds of series-connected cells in order to meet the traction power demand. Due to manufacturing tolerances, the cells used in these strings are not exactly identical in terms of their performance characteristics like actual capacity and internal resistance. Even if the cells are exactly identical initially, they may still develop differences due to their nonuniform ageing behavior, both during storage and cycling, which is inevitable because of variability in their operating conditions and the environment. These variations in cell actual capacities, cell leakage currents, and operating conditions cause SOC imbalance in cell strings. The SOC and capacity imbalance in turn results in depth-of-discharge (DOD) imbalance. Similarly, variations in cell internal resistance and temperature gradient in the coolant, which is not negligible in the battery packs of xEVs [3–6], causes thermal imbalance in the string. The SOC-level and temperature of each individual cell in a string during storage and cycling has a great impact on its electrochemical ageing, whereas the DOD affects the cycle life of a cell. The cells in a string being stored or cycled at higher SOC, DOD and temperature age faster than those at lower SOC, DOD, and temperature [7–12]. Thus, the battery pack of xEVs faces a serious issue of nonuniform ageing due to SOC, DOD and thermal imbalance. The pack may reach its end-of-life sooner due to premature failure of only one cell in the string, regardless of the high state-of-health (SOH) of other cells. The analysis of nonuniform ageing in lithium-ion battery packs is given in [13]. The need of thermal and SOC balancing is also discussed at length in Chapter 3.

The SOC and DOD imbalances are mitigated using external circuits called *cell SOC balancers*, whereas the thermal imbalance *may be* reduced using the reciprocating air-flow as suggested in [3]. There are two broad classes of cell SOC balancers, namely passive and active cell balancers. The passive balancer achieves cell balancing by burning the excess energy of cells, which have higher SOC, using over-charge method. The active balancers achieve SOC balancing by transferring the charge from cells having higher SOC to cells having lower SOC through lossless switched energy storage elements. Various topologies of switched capacitive and inductive circuits

act as intermediate storage banks, see [2, 14–17] for more details. The significance of cell SOC balancing in large BSMs has been thoroughly studied in the literature, see [18–21].

The SOC imbalance has a detrimental impact not only on the BSM ageing but also on its total capacity. This aspect has been thoroughly discussed for unbalanced, passively balanced, and actively balanced BSMs in Chapter 3. In short, the *unbalanced BSM* is the worst case, because the total capacity of this BSM is a function of initial cell SOCs which can vary a lot and thus can greatly reduce the total capacity of a BSM. The capacity of a *passively balanced BSM* is entirely defined by the weakest cell in the string. On the other hand, the capacity of an ideal *actively balanced BSM* is always given by the mean value of the cell capacities. Therefore, the actively balanced BSM would have higher total as well as remaining dischargeable capacity at any time compared with both unbalanced and passively balanced BSMs. Moreover, the cells of unbalanced and passively balanced BSMs may cycle at different DODs contrary to the cells of actively balanced BSM which cycle at the same DOD window regardless of their capacity variations. Hence, the cells of both unbalanced and passively balanced BSMs also suffer from non-uniform ageing, whereas the cells of actively balanced BSM age more uniformly. Therefore, the actively balanced BSM is able to deliver relatively higher Ah-throughput before its end-of-life. Thus, in order to maximize the capacity and to decelerate the ageing of the BSM, the *use of an active balancer is desirable.*

1.3 MLC—An Integrated Balancer and Driver

The previous section highlighted the importance of thermal and SOC balancing for enhancing the lifetime and usable capacity of a BSM. The SOC balancing can be achieved using SOC balancers, whereas the thermal uniformity can possibly be achieved using reciprocating air-flow (RF). However, as will be shown in our study, the RF alone cannot solve the problem of temperature non-uniformity, especially in the long battery strings with cell resistance variations. In our study, instead of using separate SOC balancer and RF, we focus on achieving *simultaneous thermal and SOC balancing* using a single active balancer. However, a special hardware technology with modular architecture is needed to achieve these tightly coupled and somewhat conflicting objectives. The MLC [22, 23], which provides enough degree-of-freedom to control the BSM at cell level, has been used in our study for this purpose. The MLC, contrary to two-level converter, consists of n series-connected power cells (PCs), where each PC contains an h-bridge and the isolated battery cell. Each PC can be independently controlled us-

ing *three-level modulation* to produce three different output voltage-levels. The MLC provides a large redundancy in synthesizing the output voltage, which gives extra degree-of-freedom in control. The MLC enables to distribute and modularize the BSM into smaller cells. Thus, the MLC cannot only act as a driver to generate a smoother output voltage waveform for EM, but it can also act as a balancer to simultaneously control the *modularized and distributed BSM* on a cell level. This motivates the name integrated balancer and driver. See Chapter 4 for more details on MLC.

Case 1: DC Applications

The MLC is commonly operated using phase-shifted pulse width modulation (PS-PWM), which uniformly uses all cells of the BSM inside the MLC. However, this scheme does not make the best use of the MLC for achieving the objectives of thermal and SOC balancing. The optimal strategy is to use each cell inside the BSM according to its internal state, resulting in a *nonuniform use of cells* depending upon the *degree of nonuniformity* among them. In *Paper 1*, we have formulated such an optimal policy, which uses each cell in the BSM according to its SOC level and temperature. The optimal policy is calculated in a convex optimization problem based on the assumption of dc machine as a load and perfect information of the SOC and temperature of each cell as well as of the future driving. A snapshot of these results is presented in Chapter 5.

Case 2: Three-phase AC Applications

In xEVs, three-phase (3-ϕ) permanent magnet synchronous machine (PMSM) is generally used, requiring a 3-ϕ voltage inverter. The 3-ϕ MLC has been proposed as an alternative to 3-ϕ two-level converter[1] to directly drive 3-ϕ PMSM, [24]. The authors motivated for 3-ϕ MLC based on its benefits of low-harmonics for EM, low inverter losses, and battery control due to the modularity offered by the MLC. This modularity and extra degree-of-freedom, similar to dc applications, can indeed be exploited to achieve cell level control and optimization of battery packs in 3-ϕ applications. However, in this thesis we have shown that this modularity in 3-ϕ ac applications has some other serious repercussions for the BSM. An *ideal 3-ϕ inverter, for a given load power, should only draw a constant dc current from the battery pack* as the ripple superimposed on the dc-level always increases losses in the cells. For example, the 3-ϕ two-level converter under ideal conditions draws almost constant power from a BSM, see [25], [26]. However, the BSM modularity offered by 3-ϕ MLC brings with it a major disadvantage

---

[1]we will also use the term 'inverter' alternatively in the context of ac applications.

of high-level low-frequency dc-link ripple which is a function of power factor angle θ. This ripple cannot be easily filtered without using an unreasonably big shunt-capacitor, which is infeasible for vehicle applications. Thus, this ripple would cause significant additional losses inside each cell and increase the overall temperature of the BSM. The ripple may also cause the flow of bidirectional power between the BSM and the load and may thus accelerate its capacity fading. Therefore, there is a big drawback of 3-ϕ MLC circuit topology from battery's point of view. These aspects have been investigated in detail in *Paper 2* and Appendix A. A short preview of these results is also presented in Chapter 5.

1.4 Thesis Contributions

The main contributions of this thesis are in short:

- An average state-space electro-thermal model of a BSM under the switching action of MLC has been developed. The model is presented in Paper 1.

- The thermal and SOC balancing problem has been formulated as a convex optimization problem, based on the assumption of perfect information of the SOC and temperature of each cell as well as of the future driving. The convex optimization problem formulation and the solution are given in Paper 1.

- The performance of MLC-based optimal policy under reciprocating air-flow has been compared with that under unidirectional air-flow. The conclusion is that using reciprocating air-flow has no significant benefit when using MLC-based optimal policy. These results are also presented in Paper 1.

- The issue of additional battery heating caused by the dc-link ripple in the battery of three-phase MLC has been thoroughly analyzed and the results have been compared to the case of three-phase two-level converter. The dc-link current spectrum has been computed using double Fourier series approach and the additional battery losses have been analyzed with respect to various circuit parameters and operating conditions. The size of a shunt-capacitor for the passive compensation has also been evaluated under nominal operating conditions. These results are presented in Paper 2.

- The issue of additional battery capacity fading caused by the dc-link ripple has also been thoroughly analyzed. These results are presented

in Appendix A with a short preview in Chapter 5.

1.5 Thesis Outline

Part I of this thesis serves as an introduction and provides some background information. Chapter 2 reviews the basic working principle of a lithium-ion battery (LIB) and its equivalent circuit electro-thermal model. We also discuss the LIB ageing mechanisms, common factors affecting the life-time, and the cycle-life model. In Chapter 3, the need of thermal and SOC balancing is discussed in the context of its impact on LIB ageing and the total capacity of a BSM. In Chapter 4 an overview of the functionality of MLC is given, the switched and averaged electro-thermal models of the battery under the action of MLC are presented, and the PS-SPWM algorithm is discussed. Chapter 5 gives a preview of the balancing potential of MLC. Chapter 6 gives a brief introduction to main mathematical tools that we have employed in the analysis. The issue of additional capacity fading due to dc-link ripple is analyzed in Appendix A with a short preview in Chapter 5. Appendix B gives a review of some important battery related terms. A summary of the scientific papers that constitute the base of this thesis is provided in Chapter 7, while complete versions of the papers are appended in Part II. Finally, Chapter 8 closes Part I with concluding remarks.

Chapter 2

Lithium Ion Batteries

The electrical energy can be stored in various forms. A battery stores energy in the form of chemical energy contained in the atomic bonds of its active materials and converts it to electrical energy by the mean of electrochemical redox reaction, which occurs on two electrodes when the external circuit is connected between them [27]. The basic terminology and main components of a battery are reviewed in appendix B. There are various kinds of batteries with main differences in their active materials and performance characteristics. The most common types of rechargeable batteries are lead-acid, nickel-cadmium (NiCd), nickel-metal hydride (NiMH), and lithium-ion (LIB) batteries. This chapter reviews only the LIB.

2.1 Automotive Batteries

The battery is a key to the success of electrification of vehicles. However, the batteries not only add significant extra cost, weight and volume but they also introduce some new safety hazards due to their low thermal stability especially during direct impact or some other abuse. Another disadvantage is the degradation in performance due to relatively fast ageing of batteries which may cripple the whole vehicle and may add the significant extra replacement cost during the life-time of a vehicle. Thus, the requirements for batteries in automotive applications are much more stringent than those in consumer electronics. The US Advanced Battery Consortium (US-ABC) has set separate performance goals for EVs(2020), HEVs(2010) and PHEVs(2015) [28–30]. Some of these performance goals are listed in the Table 2.1. These are quite high goals and only few battery chemistries of today can meet some of them. Currently, both NiMH and LIB are being used in commercial xEVs. Although none of these two meet all USABC requirements today, these two have the potential to meet the requirements in

future. The NiMH has been successfully employed in HEVs (Toyota Prius). However, the LIB, due to its relatively higher specific energy, higher energy density, and the long deep cycle-life, is surfacing as an alternative choice for all kinds of xEVs, especially for PHEVs and EVs. See [30–33] for further discussion on battery requirements for xEVs.

Table 2.1: USABC Battery Performance Goals for HEV, PHEV and EV

Goals at EOL	HEV (10)	PHEV (15)	EV (20)
Cost ($/system)	$500 - 800$	$1700 - 3400$	4000
Pulse Disch. Power (kW)	$25 - 40$	$38 - 50$	80
Avail. Energy (kWh)	$0.3 - 0.5$	$3.5 - 11.6$	$30 - 40$
Cycle-life	300000	$3000 - 5000$	750
Calendar-life @30° (yrs)	15	15	10
Operat. Temp. ($°C$)	-30 to $+52$	-30 to $+52$	-40 to $+50$
Battery Sys. Wt. (kg)	60	70	200
Battery Sys. Vol. (L)	45	46	133
Max. Self-discharge	50 Wh/day	50 Wh/day	$< 15\%$/mon

2.2 Basic Working Principle

The LIB consists of negative and positive porous electrodes, also known as anode and cathode respectively, the porous separator, the concentrated solution of electrolyte, and the current collectors. The most commonly used negative electrode is the lithiated graphite (LiC_6) and the most commonly used positive electrodes are metal oxides such as $LiCoO_2$, $LiMn_2O_4$, and $LiFePO_4$ etc. The most commonly used electrolyte consists of the solution of lithium salt ($LiPF_6$) in a mixed organic solvent. This organic liquid electrolyte is embedded into the porous electrode. The copper and aluminium are commonly used as current collectors for negative and positive electrodes respectively. The LIB works based on intercalation reaction, which is briefly described below, see [1, 27, 34, 35] for details.

Intercalation reaction, a type of insertion reaction, is the process of moving *guest ions* (Li^+ in the LIB case) into and out of the interstitial sites in the *host lattice*. The electrodes which can store charged species through intercalation process are called intercalation (or insertion) electrodes. The intercalation electrodes commonly have layered structure and the charged species gets sandwiched between these layers during the intercalation process. In the LIB, the charged species which intercalates in the electrodes

are lithium-ions (Li^+) and that is why they are named as lithium-ion batteries. The capacity of intercalation electrodes is limited by the number of interstitial sites, which can be occupied by charged species, in their lattice structure. Thus, the intercalation-based LIBs have less capacity than lithium-metal batteries. However, the great advantage with LIBs is that the host material does not suffer from any major structural changes during intercalation process. Thus, LIBs have much higher cycle life compared to lithium-metal batteries. Moreover, due to the absence of pure lithium metal (which is highly reactive and inflammable) inside the cell, LIBs are much safer than lithium-metal batteries.

In a LIB both electrodes can act as hosts to store lithium ions. During charging process, the oxidation reaction occurs at the positive electrode and consequently the lithium atom stored in the positive electrode increases its oxidation state by losing an electron to the external circuit. The lithium-ions move out of the interstitial sites of the positive electrode and travel, through the electrolyte phase by the process of diffusion and ionic conduction, into the interstitial sites of the negative electrode and the electrons, on the other hand, move through the external circuit to the negative electrode. On the negative electrode, the lithium-ions get reduced and intercalated in the graphite to form Li_yC_6. During discharging, the whole process is reversed. Thus, in the fully charged state all the lithium-ions are hosted in the negative electrode and in the discharged state they are all hosted inside the positive electrode. The total energy stored in the LIB at any time instant is given by the difference in energy of intercalated lithium in positive and negative electrodes. The following reactions occur at the electrodes of any LIB. Note that, in these reactions, $LiMO_2$ represents some lithium metal oxide positive material such as $LiCoO_2$ (M=Co) and C represents some carbonaceous negative material such as graphite (C_6).

Positive Electrode Reaction:

$$LiMO_2 \underset{\text{Discharge}}{\overset{\text{Charge}}{\rightleftharpoons}} Li_{1-x}MO_2 + x\,Li^+ + x\,e^-$$

Negative Electrode Reaction:

$$C + y\,L^+ + y\,e^- \underset{\text{Discharge}}{\overset{\text{Charge}}{\rightleftharpoons}} Li_yC$$

Total Cell Reaction:

$$LiMO_2 + \frac{x}{y}C \underset{\text{Discharge}}{\overset{\text{Charge}}{\rightleftharpoons}} \frac{x}{y}Li_yC + Li_{1-x}MO_2$$
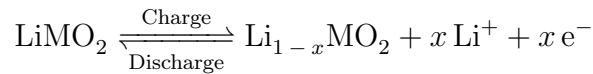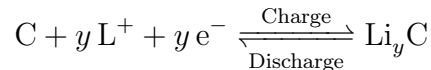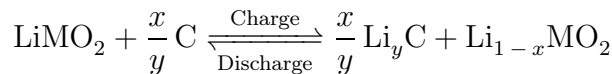
2.3   Electrical Modeling

There are two major types of battery models, namely physics-based electro-chemical models and grey-box models. The physics-based dynamic models are purely based on actual physical and chemical processes occurring inside a cell, whereas in the grey-box type models, the input-output experimental data of a cell is fitted to a parameterized model with known model structure. The concentration of lithium-ion in the electrodes is one of the states in the physics-based models and thus they give more accurate picture of a cell SOC. However, they pose very high computational burden, due to the system of coupled partial differential equations, which renders them useless for real-time control applications. The enthusiastic reader is referred to some great references [34–38] for further study on physics-based models. In the following, we present one type of grey-box model, the equivalent circuit models.

In most of battery management functions it suffices to know the response of battery SOC and terminal voltage to changes of the external input current. Therefore, the equivalent circuit modeling approaches commonly suffice. The battery characteristics are distributed in nature. However, the electrical I-V characteristics of a battery cell can be approximated fairly well by using lumped component modeling approach. In this approach, the various processes inside the battery are represented by lumped electrical components. The enhanced Thevenin equivalent circuit model, see [39–41], shown in Figure 2.1 is one such possible equivalent circuit representation of any Cell$_i$ in the BSM. The dynamic model of this circuit is given by

$$\dot{V}_{i1} = -a_{ei1}V_{i1} + b_{ei1}i_{Bi} \tag{2.1}$$

$$\dot{V}_{i2} = -a_{ei2}V_{i2} + b_{ei2}i_{Bi} \tag{2.2}$$

$$\dot{\xi}_i = -b_{ei3}i_{Bi} \tag{2.3}$$

$$V_{Bi} = f(\xi_i) - V_{i1} - V_{i2} - b_{ri}i_{Bi} \tag{2.4}$$

where i_{Bi} is the current flowing through the battery Cell$_i$ and ξ_i is the normalized SOC of Cell$_i$. Note that $\xi_i \in [0, 1]$ is a unit-less quantity. The
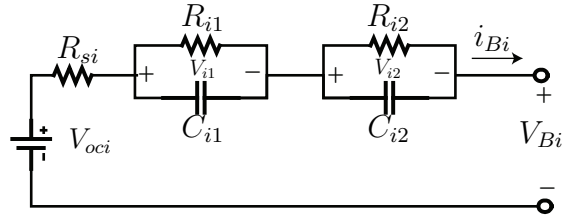
Figure 2.1: Electrical Model of Battery Module

voltages V_{i1} and V_{i2}, across capacitors C_{i1} and C_{i2}, and $V_{si} = i_{Bi}R_{si}$ models the losses due to activation, concentration and ohmic polarization respectively, and V_{Bi} is the output voltage of Cell$_i$. The SOC dependent open circuit voltage is given by $V_{oci} = f(\xi_i)$ where $f : [0,1] \rightarrow \mathbb{R}_0^+$ is a function of SOC. The parameter values are estimated based on the experimental battery data logged under controlled test conditions. In general, these parameter values are nonlinear functions of SOC and cell temperature. However, in this thesis, they will be assumed constant.

2.4 Thermal Modeling

The cell temperature dynamics in an air-cooled battery pack depends on many factors like coolant properties, cell material properties, cell placement and pack configuration. The forced-convection cooled BSM has been modeled in [3] using a *lumped-capacitance thermal modeling* and *flow network modeling* (FNM) approach. The lumped-capacitance thermal model assumes uniform temperature inside a cell and approximates the whole heat generation inside a cell by a lumped thermal source. The FNM is a general methodology that represents the flow system as a network of components and fluid flow paths to approximate the temperature distribution inside it [42]. The coolant flow inside the BSM has been modeled in [3] using the network of fluid temperature nodes where each Cell$_i$ exchanges heat with the coolant fluid, in the upstream and the downstream direction, through two fluid temperature nodes '$i-1$' and 'i' respectively whereas each temperature node is shared between two consecutive cells. Now assuming that the coolant flow direction is from Cell$_{i-1}$ to Cell$_i$, the dynamics of the Cell$_i$ temperature is given by [3]

$$\dot{T}_{si} = -a_{si}T_{si} + b_{si}i_{Bi}^2 + a_{si}T_{fi-1} \tag{2.5}$$

where the coefficients a_{si} and b_{si} are defined in Table 1 in Paper 1 and the T_{fi-1} is the temperature of upstream fluid node '$i-1$' of Cell$_i$ and it is related to the temperature T_{fi} of downstream fluid node 'i' of Cell$_i$ by

$$T_{fi} = \frac{(T_{si} + \beta_i\, T_{fi-1})}{\alpha_i} \tag{2.6}$$

where α_i and β_i are defined in Table 1 of Paper 1. Given that T_{f0} is a known quantity, then by a forward recursion of equation (2.6), any T_{fi} can be expressed as a function of inlet fluid temperature T_{f0} and the temperatures T_{s1} to T_{si} of Cell$_1$ to Cell$_i$ respectively.

2.5   Cell Ageing

Lithium-ion batteries (LIBs), like all other battery types, age with time both during storage and cycling. The ageing processes inside a cell result in energy capacity fade, power fade, and increase in self-discharge rates [1, 7, 12]. The capacity and power fades are defined below.

- Capacity fade is the loss of ability of an electrode's active mass to store or deliver the electrical charge. The capacity fade in LIBs is primarily caused by the loss of cyclable active lithium and reduction in interstitial sites in the lattice structure of the active material due to structural degradation, mainly, of anode [12, 43].

- Power fade is primarily caused by the internal resistance growth of a cell. There are various kinds of resistances in a cell and the resistance increase may be in one or all of them. The resistance may grow due to many mechanisms including degradation of current collectors, degradation of coating (which is used for electronic conduction in active mass), the degradation of binding interface between electrode and current collectors, the growth of extra resistive passivation film on electrodes, and loss of ionic conductivity in the electrolyte.

The capacity and power fade, though have some common electrochemical and mechanical causes as well, however have different origins in general. The actual degradation mechanisms behind these effects are very complex, tightly coupled and still not very well understood. The ageing rate is highly dependent on electrode materials and the properties of electrolyte and additives.

2.5.1   Types of Ageing Mechanisms

The ageing mechanisms on anode and cathode are different [7]. There are various reasons of ageing but one main cause is the electro-chemical side reactions which occur inside a cell in addition to the main intercalation reactions. These side reactions result in side-products, which consume the active material of a cell [44]. Some of these side reactions are completely reversible whereas others are irreversible. The irreversible side reactions result in the permanent power and energy capacity fade of the battery and occur both on anode and cathode. In the following, we give a brief overview of the most important ageing mechanisms in anode and cathode and the various factors that accelerate the cell ageing. For details see [7–11].

Ageing Effects on Anode

The thermodynamical stability of anode is the most critical factor for battery ageing. The lithiated graphite (LiC_6) anode lies below the lower limit of thermodynamic stability window of organic electrolytes [44]. It results in the strong reactivity between anode and the electrolyte which makes the organic electrolyte solvents highly susceptible to side reduction reaction at anode. This side reaction is on the form [8, 10, 45]

$$S + Li^+ + e^- \longrightarrow P \tag{2.7}$$

where S refers to the solvent species and P is the product of this side reaction. The side reaction (2.7) is irreversible and thus results in capacity fade due to the loss of cyclable lithium. This side reaction occurs first during the cell formation process and forms a passivation film by depositing P on the solid-electrolyte interface (SEI) [10]. This initial passivation film is called *SEI layer*. The thickness of SEI layer should not increase, as it increases the ohmic resistance and results in power fade. In order to prevent the side reaction (2.7) from continuing further, the electrons from anode must not reach the molecules of electrolyte. Thus, the SEI layer must be fully permeable to lithium-ions but must act as a perfect electronic insulator. However, due to defects in SEI layer, the side reaction may continue on anode. This deposits precipitates on initial SEI layer and increases its thickness. This extra resistive film on SEI layer results in power fade. The side reaction also causes the corrosion of lithium in the anode which results in the capacity fade due to irreversible loss of cyclable lithium. Thus, the side reaction (2.7) is believed to be one of the main ageing mechanism on the negative electrode. Therefore, the ageing and proper operation of a LIB is highly dependent on the *stability of SEI layer*. The extra resistive film formed on SEI has temporal and spatial variations. The film growth rate is a function of cell SOC and the charging current [45]. Table 2.2 shows the main ageing mechanisms on anode, their effects and the factors affecting ageing rates, see [9] for further details.

Ageing Effects on Cathode

The ageing of positive electrode during cycling mainly occurs due to its volume variations. The volume increases during intercalation and decreases during de-intercalation of lithium. These repeated cycles of intercalation and de-intercalation cause strain in the active material particles and they may lose contact with the conductive additive network within the composite electrode [8]. Thus, the structural degradation is believed to be the main

Table 2.2: Main Ageing Mechanisms on Lithiated Carbon Anode, See [9] for details

Cause	Effect	Leads to	Reduced by	Enhanced by
Electrolyte reduction side reaction (Electrolyte Decomposition)	Loss of Lithium, Impedance rise	Capacity fade, Power fade	Stability of SEI layer	High Temperature, High SOC
Decrease in accessible surface area due to SEI film growth	Impedance rise	Power fade	Stability of SEI layer	High Temperature, High SOC
Changes in anode porosity due volume changes and SEI film growth	Impedance rise, polarization losses	Power fade	Stability of SEI layer	High cycling rate, High SOC
Contact loss of active material particles due to volume changes during cycling	Loss of active material	Capacity fade	—	High cycling rate, High DOD
Corrosion of Current Collector	Impedance rise, polarization losses	Power fade	—	Over-discharge, Low SOC
Metallic lithium deposition and subsequent decomposition of electrolyte	Loss of lithium, loss of electrolyte	Capacity fade, Power fade	—	Charging at low temperatures, High cycling rate

ageing mechanism in cathode. In addition, the cathode also has strong oxidizing properties against the electrolyte solvent. Thus, cathode ageing may also occur due to electrochemical side oxidation reaction. The positive electrodes in LIBs normally operate close to the upper limit of thermodynamical stability of organic electrolytes. Since, during cell formation process, nothing like SEI protective layer forms on positive electrode, even the slight over-charge may trigger furious oxidation reaction between electrolyte solvent and the cathode. This may result in fire and explosion due to gas evolution, especially in lithium cobalt oxide based LIBs. The side oxidation reaction between cathode and electrolyte decomposes the electrolyte and forms the precipitates, which block the interstitial sites in the lattice of positive electrode. This leads to capacity fade due to the loss of active material in the cathode and electrolyte decomposition. The decomposition of electrolyte also forms passivation film on cathode, which increases the ohmic resistance and leads to power fade. The capacity and power fade in cathode is accelerated at higher temperature and SOC.

2.5.2 Ageing Conditions

In the view of battery's mode of utilization, the ageing can be divided into two main categories: the calendar ageing and the cycle ageing as described below. The ageing during cycling and rest are commonly considered *additive*, but complex interactions may occur as well [8].

Calendar Ageing

Calendar ageing is the proportion of irreversible capacity loss that occurs with time especially during storage. During storage, the ageing is mainly governed by the thermodynamical stability of electrodes and separator etc in the electrolyte. The loss of cyclable lithium due to side reactions and SEI film growth at anode have been reported as the main source of ageing during storage [7, 46]. Cell ageing and self-discharge rate during storage highly depends on storage conditions. Thus, the ageing of battery can be controlled by choosing optimal storage conditions. The cell storage temperature and SOC level are two main factors which strongly influence the rate of calendar ageing. The higher storage temperature accelerates side reactions on SEI and corrosion of current collectors whereas too low temperature facilitates the lithium deposition on anode. Similarly, the higher SOC level also facilitates side reactions on SEI. Thus, thermal and SOC imbalance during storage will cause nonuniform ageing of cells in a BSM. The effect of temperature and SOC on battery ageing is not additive [47,48]. The calendar ageing is a nonlinear function of time, temperature and SOC.

Cycle Ageing

The ageing of a battery also occurs with each charge/discharge cycle, so called cycle ageing. The main ageing mechanisms during cycling are changes in the porosity of electrodes [8] and the contact loss of active material particles due to volume variations of both anode and cathode. On anode, the SEI layer may crack due to volume changes during cycling, which is then automatically repaired by consuming available lithium and thus results in capacity fade [8]. On cathode, the volume variations induces the contact loss between particles of active material and the conductive additive network. Thus, the structural degradation of the active material is considered the main cause of ageing during cycling [46]. The cycle ageing is greatly influenced by battery operating temperature, SOC level, DOD, cycling frequency (or rate), and c-rate. Higher values of these variables accelerate the cycle ageing and thus reduce the cycle-life of a battery [7–9, 12].

2.5.3 Cycle-life Model

The estimation of battery ageing is quite challenging due to highly intertwined internal and external stress factors (temperature, SOC level, DOD, c-rates etc). The ageing of batteries in real xEVs during operation is complicated further by the varying operating environment and the utilization mode. There are various estimation methods including phenomenological approach, which uses electrochemical model of battery processes [10, 49–51], equivalent-circuit-model based approach [52], and the performance-based approach [53]. The performance-based approach uses battery performance metrics like energy capacity or the power capacity to assess the age of a battery. The loss in performance is indicated by either capacity loss or resistance growth (power loss). Here, we only present performance-based cycle-life model as we need it later in our analysis. It is given by [12, 54]

$$\Delta E_0 = B(c) \cdot \exp\left(\frac{-E_a(c)}{R \cdot T}\right) \cdot (A_h)^{0.55} \text{ with } B(c) = 10000 \left(\frac{15}{c}\right)^{1/3} \quad (2.8)$$

where ΔE_0 is the percentage of energy capacity loss of the cell w.r.t the cell's initial capacity $E_0(0)$, $E_a = (31700 - 370.3 \times c)\,\text{J}\,\text{mol}^{-1}$ is the electrode reaction activation energy, c is the c-rate, R is the ideal gas constant, T is the lumped cell temperature, A_h is an ampere-hour throughput which represents the total amount of charge processed (delivered or absorbed) by a battery during cycling and B is a c-rate dependent coefficient. The capacity fade model given by eq. (2.8) can be used to predict the capacity loss for a given A_h and c-rate.

Chapter 3

Thermal and SOC Balancing

The ageing of an individual cell, as discussed in the previous chapter, is greatly affected by various factors like SOC, DOD, tememperature, and various other operating conditions. This chapter discusses battery pack level issues resulting from the interconnection of individual cells. We will particularly focus on a string of series-connected cells, so-called BSM. Thermal and SOC imbalances are two major factors which have a huge negative impact on the BSM performance. Firstly, we will discuss their impact on nonuniform ageing of BSM, secondly various types of SOC balancers and their impact on BSM capacity will be discussed, thirdly causes of thermal balancing and some possible solutions will be discussed, and finally we will discuss the possibility of simultaneous thermal and SOC balancing.

3.1 Nonuniform Ageing of a BSM

The battery pack of xEVs consists of long strings of hundreds of series-connected cells in order to meet the traction power demand. In this section, we will discuss how the variations in the ageing of individual cells affect the overall ageing of such cell strings. The nonuniform ageing of cells in these strings mainly come from variations in cell parameters and performance characteristics. The variations in cell parameters and performance characteristics arise from manufacturing tolerances, which are inevitable, even for a particular batch of cells from one manufacturer. The various specifications (like actual capacity, resistance, and self-discharge rate etc.) of cells are generally assumed to have gaussian distribution [13]. The specifications of any individual cell may lie anywhere in the distribution. Even if the cells are exactly similar electrically, their ageing behavior, both during storage and cycling, may still vary due to variability in their operating conditions and the environment. The imbalance in cell characteristics may enhance

further with time due to different rates of ageing for different cells. The analysis of nonuniform ageing in LIB packs is given in [13].

These variations are not that significant for independent cells. However, when these cells are connected in a long series string, like in the case of BSM, then these variations may have significant impact on the performance of the whole string. The variations in cell actual capacities, cell leakage currents, and operating conditions cause SOC imbalance in cell strings. The SOC and capacity imbalance in turn results in depth-of-discharge (DOD) imbalance. Similarly, variations in cell internal resistance and temperature gradient in the coolant, which is not negligible in the battery packs of xEVs [3–6], causes thermal imbalance in the string. The SOC-level and temperature of each individual cell in a string during storage and cycling has a huge negative impact on its electrochemical ageing whereas the DOD affects the cycle life of a cell (see table 2.2 on page 16 and section 2.5.2). The cells in a string being stored or cycled at higher SOC, DOD and temperature age faster than those at lower SOC, DOD, and temperature. It should also be noted that nonuniform ageing and SOC and thermal imbalance are tightly coupled, imbalance cause ageing which in turn cause even more imbalance. Thus, if this situation continues unhindered it will severely affect the performance of a BSM, resulting in its premature end-of-life. In addition, SOC imbalance may also result in over-charge and over-discharge conditions for some cells in the string, which is quite dangerous for lithium-ion cells as they may explode under these conditions. Thus, the lithium-ion BSM faces serious issues of nonuniform ageing and safety hazards and requires an intelligent cell level battery management system (BMS) to address these issues.

3.2 SOC Balancing

The cell SOC balancing is one of the most important function of any advanced battery management system especially for long series string of cells. It affects not only the non-uniform ageing of a BSM, but also its total capacity (this aspect will be discussed later in this section). The significance of cell SOC balancing in large BSMs has been studied thoroughly in the literature, see [18–21].

3.2.1 Types of SOC Balancers

There are two broad classes of SOC balancers [53]: chemical cell balancer and physical cell balancer. In chemical cell balancing, the internal side reactions of a battery are exploited to achieve balancing. For example, in lead-acid and NiMH batteries the over-charging can be used to equalize

all the cells. However, this approach is not suitable for LIB as it cannot tolerate over-charge and may explode. The physical cell balancer requires an external circuit to interact with each cell in a string. In this approach, the external circuit can be dynamically reconfigured to provide the dissipative or non-dissipative alternate paths for direct energy flow between various cells in a string. In the following, we will discuss two main types of physical SOC balancers.

Passive Cell Balancers (Dissipative)

The passive methods commonly achieve cell balancing during the end of charging phase by dissipating the energy of a cell with highest SOC. The passively balanced BSM is balanced only once, during a cycle, in its fully charged state and is called a *top balanced BSM*. The passive balancing circuit only consists of resistors without any switches and thus can not be actively controlled externally. This method is very simple as it achieves balancing by over-charging and burning in resistors the excess charge of cells. Thus, it does not require any complicated control algorithm except charge control. However, it is dissipative and thus less efficient. This method can only be used for lead-acid and NiMH based batteries due to their tolerance against over-charge condition [19].

Active Cell Balancers (Non-Dissipative)

The active cell balancers use external switched circuits to actively transfer (shuttle, shuffle, shunt, or redistribute) the energy among cells of a BSM to achieve SOC balancing. The active balancing network commonly consists of semiconductor switches and some other circuit elements which provide alternate paths for energy flow. Thus, the active cell balancer can be actively controlled externally using a controller. Even though the active cell balancing method may be based on resistor shunting, the most commonly used circuit elements are lossless energy storage elements like capacitor and inductor. Therefore, the active cell balancers are commonly non-dissipative (assuming ideal transistors and ideal energy storage elements) and have high energy efficiency compared to passive cell balancers. However, the active cell balancers generally require more advanced control algorithms which may become quite complex for large battery packs. The active cell balancer is the only solution for a LIB pack, because it cannot tolerate over-charging based passive balancing method [2, 19, 55]. There are various active balancing methods like cell shunting, cell-to-cell, cell-to-pack, pack-to-cell and cell-to-pack-to-cell, see [2, 56] for further details on balancing hardware and see [57] for optimization-based thorough performance evaluation of various

balancing methods.

3.2.2 Impact of SOC Balancers on BSM Capacity

In this subsection, firstly we will show the negative impact of SOC imbalance on the total capacity of a BSM and secondly we will discuss how passive and active balancers can mitigate this impact. The capacity and SOC of a BSM is a function of cell SOCs and their capacities. Let us consider a BSM consisting of a series string of n cells, Cell_1 to Cell_n, with different capacities $(C_1 \cdots C_n)$ and SOCs $(\xi_1 \cdots \xi_n)$. Let us also assume that the leakage current of all cells is the same. Now, in the following, we will discuss the BSM capacity and SOC for three different cases.

Case 1: BSM without Balancing

Let us first consider the case of an unbalanced BSM. Since the BSM has no balancing device, it has SOC variations among its cells all the time as shown in Figure 3.1. In this case, the charging is stopped when any cell in the string reaches its fully charged state (or its EOCV) and similarly the discharging is stopped when any cell in the string reaches its fully discharged state (or its EODV). Thus, the *chargeable capacity*[1] of an unbalanced BSM, with unequal cell capacities, is given by [53, 58, 59]

$$C_{\text{BSM},C}^u = \min_i((1 - \xi_i)C_i) \qquad (3.1)$$

and the remaining *dischargeable capacity* of the unbalanced BSM is given by

$$C_{\text{BSM},D}^u = \min_i(\xi_i C_i). \qquad (3.2)$$

Thus, the maximum possible *capacity of the unbalanced BSM* is given by

$$C_{\text{BSM}}^u = C_{\text{BSM},D}^u + C_{\text{BSM},C}^u = \min_i(\xi_i C_i) + \min_i((1 - \xi_i)C_i) \qquad (3.3)$$

and its *SOC* is given by

$$\xi_{\text{BSM}}^u = \frac{C_{\text{BSM},D}^u}{C_{\text{BSM}}^u} = \frac{\min_i(\xi_i C_i)}{\min_i(\xi_i C_i) + \min_i((1 - \xi_i)C_i)} \qquad (3.4)$$

The total capacity and SOC of the BSM given by eq. (3.3) and eq. (3.4) respectively can not be easily related to the total capacity and SOC of any single cell in the BSM. Thus, in order to simplify the expressions, let us assume the BSM to be fully charged $(\xi_{\text{BSM}}^u = 1 \Rightarrow C_{\text{BSM},C}^u = 0)$ and define

$$C_{\min} = \min_i\{\xi_i C_i | \xi_{\text{BSM}}^u = 1\}. \qquad (3.5)$$

---

[1]See appendix B for various definitions of capacities and other battery related terms.

Now let us suppose that a certain Cell_k, where $k \in [1, \cdots, n]$, satisfies the eq. (3.5) then $C_{\min}$ is the minimum dischargeable capacity of this Cell_k in the fully charged state of BSM. Now the total capacity of BSM, given in eq. (3.3), is simplified to

$$C_{\text{BSM}}^u = C_{\min} \tag{3.6}$$

Similarly, assuming uniform leakage current for all cells, the remaining dischargeable capacity of the BSM is given by

$$C_{\text{BSM},D}^u = C_{k,D} = \xi_k C_k. \tag{3.7}$$

where $C_{k,D} = \xi_k C_k$ is the remaining dischargeable capacity of Cell_k at any time 't'. Now, in terms of new definitions, SOC of the BSM, given in eq. (3.4), is simplified to

$$\xi_{\text{BSM}}^u = \frac{C_{\text{BSM},D}^u}{C_{\text{BSM}}^u} = \frac{C_{k,D}}{C_{\min}} = \frac{\xi_k C_k}{C_{\min}} \tag{3.8}$$

Thus, under stated assumptions, the total capacity and SOC of the BSM depends entirely on the total capacity and SOC of the Cell_k that has minimum dischargeable capacity in the whole string at fully charged state of the BSM. Let us suppose $\xi_{k,0} = \xi_k(t_0)$ is the initial SOC of a Cell_k when BSM is in the fully charged state. The total capacity of the BSM ($C_{\text{BSM}}^u = C_{min} = \xi_{k,0} C_k$) is, then, a function of $\xi_{k,0}$ and C_k. Thus, if a Cell_k is not fully charged when BSM is fully charged (i.e. $\xi_k \neq 1$ if $\xi_{\text{BSM}}^u = 1$) then the total capacity of the BSM will only be a fraction of C_k. For example, consider a BSM having equal cell capacities but highly unbalanced SOCs ($\xi_{k,0} \ll \xi_{i,0} \, \forall i \neq k$), the total capacity of this BSM will be very low. Thus, the SOC imbalance can greatly reduce the total capacity of a BSM. Also note that the cells, in the unbalanced BSM, cycle at different DODs with some cells cycling at lower DOD and others at higher DOD.

Case 2: BSM with Passive Balancing

Let us assume that the BSM is now being balanced by a passive cell balancing device as shown in Figure 3.2(a). In passive cell balancing, all the cells in a BSM are commonly top balanced [21] and consequently a minimum capacity cell goes through full charge and discharge cycle. Thus, the total capacity of a passively balanced BSM is defined by a cell with the minimum total capacity in the BSM. Let us suppose that a certain Cell_k, where $k \in [1, \cdots, n]$, is a cell with minimum total capacity in the BSM, then the *total capacity of the passively balanced BSM* is given by [53, 58, 59]

$$C_{\text{BSM}}^p = C_k = \min_i(C_i) \tag{3.9}$$

23
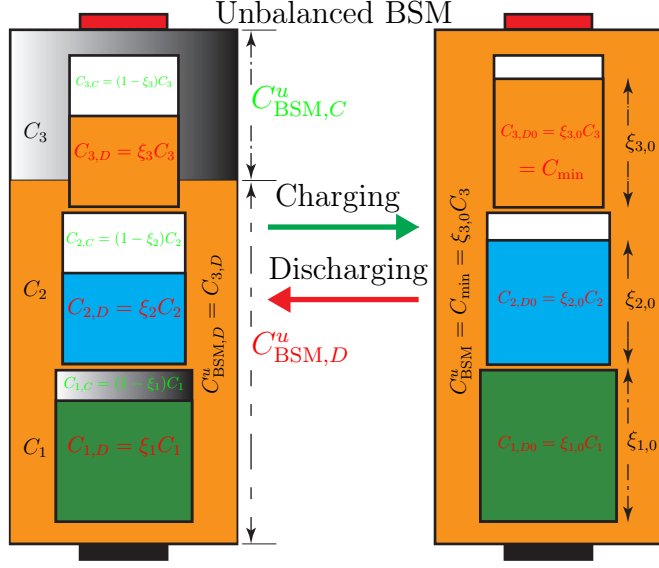
Figure 3.1: Unbalanced BSM: Illustration of the impact of SOC imbalance. Note variations in cell capacities $(C_3 < C_2 < C_1)$ and initial cell SOCs $(\xi_{2,0} < \xi_{3,0} < \xi_{1,0})$.

and the remaining *dischargeable capacity of the BSM* is given by

$$C^p_{\text{BSM},D} = \min_i(\xi_i C_i) \tag{3.10}$$

where ξ_i is the SOC of Cell$_i$. Now, the *SOC of the BSM* is given by

$$\xi^p_{\text{BSM}} = \frac{C^p_{\text{BSM},D}}{C^p_{\text{BSM}}} = \frac{\min_i(\xi_i C_i)}{\min_i(C_i)} = \frac{\min_i(\xi_i C_i)}{C_k} \tag{3.11}$$

Under the assumption of top balanced BSM and the same leakage current for all cells, a cell with minimum total capacity will also have minimum remaining capacity during the whole cycle of BSM. Thus, the eq. (3.10) is simplified to

$$C^p_{\text{BSM},D} = \xi_k \left(\min_i(C_i) \right) = \xi_k C_k \tag{3.12}$$

where ξ_k is the SOC of a Cell$_k$ with minimum total capacity. Now, eq. (3.11) is simplified to

$$\xi^p_{\text{BSM}} = \xi_k \tag{3.13}$$

Thus, the total capacity and SOC of the passively balanced BSM is, respectively, equal to the total capacity and SOC of a Cell$_k$ that has minimum total capacity in the whole BSM. Because the passive balancer does not do balancing all the time, cells will develop the SOC imbalance again during

discharging of BSM, and when Cell$_k$ becomes empty the BSM will not discharge further regardless of the charge left in other cells. Thus, the cells of the passively balanced BSM also cycles at different DODs and are therefore not fully utilized.

Case 3: BSM with Active Balancing

Now let us suppose that the BSM is perfectly balanced by a 100% efficient active cell balancer as shown in Figure 3.2(b). The *total capacity of an actively balanced BSM* is then equal to the mean of cell capacities and is given by [53, 58, 59]

$$C_{\mathrm{BSM}}^a = \frac{1}{n}\sum_{i=1}^n C_i \qquad (3.14)$$

and the remaining *dischargeable capacity of the BSM* is given by

$$C_{\mathrm{BSM},D}^a = \frac{1}{n}\sum_{i=1}^n (\xi_i C_i) \qquad (3.15)$$

where ξ_i is the SOC of Cell$_i$. Now, the *SOC of the BSM* is given by

$$\xi_{\mathrm{BSM}}^a = \frac{C_{\mathrm{BSM},D}^a}{C_{\mathrm{BSM}}^a} = \frac{\sum_{i=1}^n (\xi_i C_i)}{\sum_{i=1}^n C_i} \qquad (3.16)$$

For the case of ideal active cell balancer,

$$\xi_i(t) = \xi_j(t) = \bar{\xi}(t), \ \forall t, \ \forall i,j \in \{1, \cdots, n\}$$

so the remaining capacity of the BSM in eq. (3.15) is simplified to

$$C_{\mathrm{BSM},D}^a = \bar{\xi}\left(\frac{1}{n}\sum_{i=1}^n (C_i)\right) \qquad (3.17)$$

and the SOC of BSM in eq. (3.16) is simplified to

$$\xi_{\mathrm{BSM}}^a = \bar{\xi} \qquad (3.18)$$

Thus, the total capacity of an ideal actively balanced BSM is equal to the mean of all cell capacities and SOC of the BSM is equal to the SOC of each cell in the BSM. Also note that the active balancer keeps all the cells balanced all the time during charging and discharging which means cells become full or empty simultaneously. Thus, the cells in actively balanced BSM cycle at the same DOD and are utilized, in terms of the Ah-throughput, according to their capacities. The active cell balancer achieves continuous SOC balancing in such a way that a cell with lower capacity is utilized less than a cell with higher capacity.
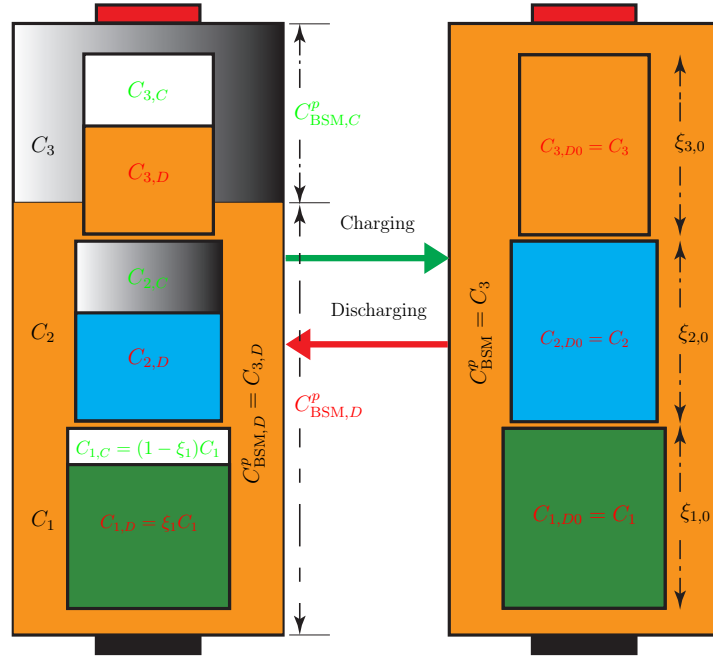
(a) Passively balanced BSM.
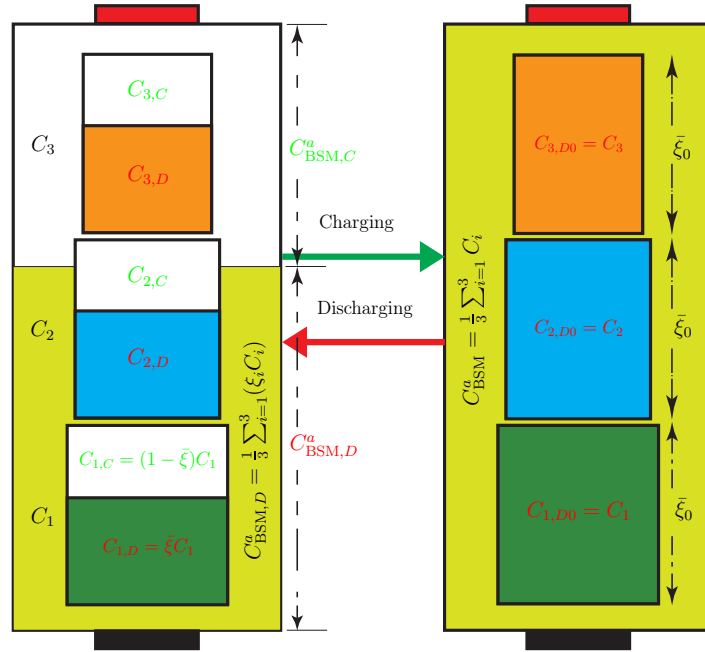
(b) Actively balanced BSM.

Figure 3.2: BSM capacity under passive and active balancing.

Summary

The unbalanced BSM is the worst case, because the total capacity of this BSM is a function of initial cell SOCs which can vary a lot (if not monitored and controlled) with battery ageing. Thus, it can greatly reduce the total capacity of a BSM even when all the cells have equal and high capacities individually. The capacity of a passively balanced BSM is entirely defined by the weakest cell in the string. If all cells in the string have the same capacities and leakage current then the total capacity of the passively balanced BSM will not be reduced by their series connection, but some energy will be wasted during balancing. On the other hand, the capacity of an ideal actively balanced BSM is always given by the mean value of the cell capacities. Therefore, the actively balanced BSM would have higher total as well as remaining dischargeable capacity at any time compared with both unbalanced and passively balanced BSM i.e.

$$C_{\mathrm{BSM}}^u < C_{\mathrm{BSM}}^p < C_{\mathrm{BSM}}^a$$

Moreover, the cells in the unbalanced and passively balanced BSMs are cycled at different DODs contrary to the cells of actively balanced BSM. Thus, cells of unbalanced and passively balanced BSMs suffer from nonuniform ageing whereas cells in the actively balanced BSM age more uniformly. Therefore, unbalanced and passively balanced BSMs may reach their end-of-life sooner, whereas the actively balanced BSM is able to deliver relatively higher Ah-throughput before its end-of-life.

Remark 3.1. *The difference in cell leakage currents causes variation in cell SOCs. Thus, a BSM with equal cell capacities and perfectly balanced SOCs initially may become unbalanced with time even on the shelf. Therefore, the difference in leakage current may also cause nonuniform ageing of the BSM. When the assumption of uniform leakage current does not hold then the relationships given by equations (3.2) and (3.10) in the last section will not be applicable. The difference in leakage current affects the remaining dischargeable capacity of the BSM. During cycling, a $Cell_i$ with higher $C_{i,D}$ at some initial time may have lower $C_{i,D}$ at some later time. Thus, the relations given by equations (3.2) and (3.10) now must include the correction factor for leakage current of each cell in order to correctly calculate the remaining dischargeable capacity $C_{\mathrm{BSM},D}$ of the BSM.*

3.3 Thermal Balancing

Thermal imbalance is another major problem in large BSMs which also needs special attention. For a more detailed critical review of thermal issues

in LIB packs in xEVs, the reader is referred to [3–5].

3.3.1 Causes of Thermal Imbalance

There are two main sources of thermal imbalance:

Variation in Cell Resistances

Fresh cells, even from the same batch, may differ in their ohmic resistance due to manufacturing tolerances. When these cells are serially connected to form a BSM, the difference may increase further with time due to nonuniform rate of resistance growth. The difference in ohmic resistance implies difference in ohmic losses which leads to temperature differences among cells.

Temperature Gradient in the Coolant

Consider a BSM consisting of n series connected cells. Now using the flow network modeling of the coolant and the forward recursion of eq. (2.6), the temperature T_{fi} of the coolant fluid node attached to any Cell$_i$ in the BSM is given by

$$T_{fi} = a_{fi1} T_{s1} + a_{fi2} T_{s2} + \cdots + a_{fii} T_{si} + b_{fi} T_{f0} \qquad (3.19)$$

where the coefficients are given by

$$a_{fii} = \left(\frac{1}{\alpha_i} \right), \quad b_{fi} = \left(\frac{\prod_{k=1}^{i} \beta_k}{\prod_{k=1}^{i} \alpha_k} \right), \quad \forall i \geq 1 \qquad (3.20)$$

$$a_{fij} = \left(\frac{\prod_{k=(j+1)}^{i} \beta_k}{\prod_{k=j}^{i} \alpha_k} \right), \quad \forall i > j, \quad a_{fij} = 0, \ \forall i < j \qquad (3.21)$$

and the coefficients α_i and β_i are defined in Table 1 in Paper 1. Thus, according to the above equation, the coolant in the BSM suffers from a temperature gradient due to build up of additive heat from cells along the coolant stream. It results in higher ambient temperature for downstream cells (cells away from the coolant inlet). It has been reported in [6] that the temperature gradient in xEV battery packs is not negligible. Thus, in addition to SOC balancing, thermal balancing of xEV packs is necessary to enhance their life-time.

Remark 3.2. *In addition to cell-to-cell temperature variations, the negative impact of temperature gradient within a single cell is also reported in [60] and [6]. However, in our study we neglect the inhomogeneities within each cell and only consider cell-to-cell variations.*

3.3.2 Potential Solutions

Thermal imbalance in large battery packs can potentially be mitigated using following two approaches.

Reciprocating Coolant Flow

Unidirectional coolant flow (UF) is commonly used in battery packs. However, this cooling scheme cannot compensate thermal imbalance due to temperature gradient in the coolant as shown in equation (3.19). Reciprocating coolant flow scheme has been suggested in [3] to solve this issue. In this scheme, the coolant flows back and forth in the battery pack at a fixed reciprocating time period. This period can be tuned to improve the balancing performance to some extent. However, RF cannot solve imbalance arising from variation in cell resistance or variation in its other parameters like thermal resistance. The performance of RF under parameter variations has been investigated in detail in Paper 1.

Load Balancing

Thermal balancing can also be achieved by load balancing/scheduling of each cell in the string. In this method, each cell in the string is used according to its *thermal condition*. Thus, this policy has a full potential to compensate thermal imbalance due to both coolant temperature gradient and parametric variations. However, this method requires a special hardware which should enable to *bypass the load current* around each cell. This thesis focuses on this method to achieve thermal balancing.

3.4 Goals of Thermal and SOC Balancing

In any large BSM, the temperature and SOC deviations among cells must simultaneously stay within certain limits in order to meet the following two major goals:

- *Capacity Maximization of BSM*: The SOC imbalance causes reduction in the total capacity of BSM and the thermal imbalance deteriorates it further. Thus, in order to maximize the total capacity of the BSM, the ideal cell balancer should *actively and simultaneously equalize* both temperature and SOC of all cells in the BSM.

- *Ageing Deceleration of BSM*: The second goal of thermal and SOC balancing is to achieve more uniform ageing of cells in the BSM and thus decelerate its overall ageing rate.

29

3.5 Simultaneous Thermal and SoC Balancing

The last section highlighted the importance of thermal and SOC balancing for enhancing the lifetime and usable capacity of a BSM. The SOC balancing can be achieved using dedicated SOC balancers whereas the thermal balancing under parameter variations can potentially be achieved using load scheduling of each cell. In our study, instead of using separate SOC and thermal balancers, we focus on achieving simultaneous thermal and SOC balancing using a single active balancer. Since SOC and thermal balancing are two tightly coupled and somewhat conflicting objectives, the question arises whether it is feasible at all to achieve both of these objectives simultaneously. Although, a theoretical feasibility analysis is still pending, however, we have shown, through case studies, in our Paper 1 that by optimally exploiting the brake regeneration phases in the drive cycle, both SOC and thermal balancing can be achieved. However, to achieve this we need an active balancing device with a very special underlying modular structure that gives us sufficient DOF to independently control each cell in a BSM. In next chapter we will present the MLC which has full potential to serve this purpose.

Chapter 4

Cascaded Multilevel Converters

The previous chapter highlighted the importance of thermal and SOC balancing for enhancing the lifetime and total capacity of a battery pack. However, a special hardware technology with modular architecture is needed to achieve these tightly coupled objectives. In this chapter, we will briefly introduce one such technology– the cascaded H-bridge (CHB) multilevel converter (MLC) which provides us enough degree-of-freedom to control the BSM at cell level to achieve our set goals. The MLC synthesizes the output voltage waveform from several dc voltage levels. We get smoother output waveform with higher number of levels. There are various other types of MLCs like neutral-point clamped (NPC) MLC, flying capacitor (FC) MLC etc. However, these MLCs use one single battery pack and are thus not suitable for battery control on a cell level. Thus, in this chapter we will only briefly review the basic architecture, functionality, merits, demerits, and a common modulation strategy of CHB MLC. For a more detailed treatment of this converter, the reader is referred to [22, 23, 61].

4.1   Two-level Converters

The two-level converter (TLC) is operated using *two-level modulation* (i.e. a PWM signal switches between two voltage levels). The conventional single-phase (1-ϕ) TLC consists of a single large BSM connected with a single H-bridge (HB) as shown in fig. 4.1(b). The HB, consisting of two half-bridges, can produce a four-quadrant controllable dc output using four switches S_1, S_2, $\bar{S}_1$, $\bar{S}_2$. For high-voltage applications, the insulated-gate bipolar transistors (IGBTs) are used for these switches inside TLC. Although, the TLC can only switch the output voltage between positive and negative poles, sinusoidal current and voltage waveforms in the output can be achieved using sine-PWM (SPWM) and low pass filtering by the load.

(a) Block diagram of a 1-ϕ MLC. Note the distributed BSM which is distributed among 'n' PCs.

(b) Block diagram of a 1-ϕ TLC. Note the single large BSM.
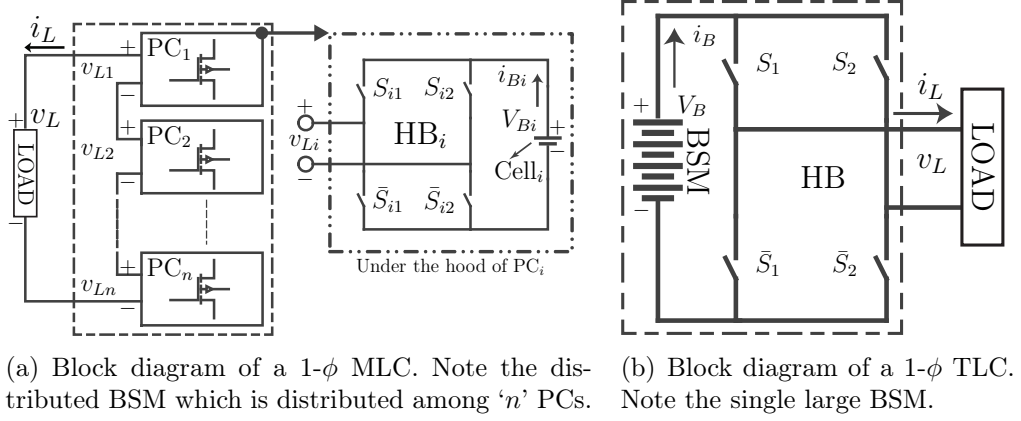
Figure 4.1: Block diagrams of 1-ϕ CHB MLC and TLC.

4.2 Basic Working Principle of MLC

The 1-ϕ CHB MLC, contrary to TLC, consists of n series-connected power cells (PCs) where each PC contains an HB and the isolated cell as shown in Figure 4.1(a). Each PC_i can be independently controlled using *three-level modulation* to produce three different output voltage-levels using four switches $S_{i1}, S_{i2}, \bar{S}_{i1}, \bar{S}_{i2}$ as shown in Figure 4.1(a). The MLC enables to split a single large high-voltage BSM (BP) into n smaller low-voltage cells (BSMs) and distribute them into PCs. Thus, low-voltage MoSFETs can be used for switches inside each PC of MLC. There are three different modes (switching states) of operation of each PC_i, depending on which switch pair is turned-on. In *Mode–1* $v_{Li} > 0$, in *Mode–2* $v_{Li} < 0$ and in *Mode–3* $v_{Li} = 0$. The switching function $s_i(t)$ for PC_i (or alternatively for $Cell_i$) is defined by

$$s_i(t) = s_{i1}(t) - s_{i2}(t) = \begin{cases} 1, & \textit{Mode–1} \\ -1, & \textit{Mode–2} \\ 0, & \textit{Mode–3} \end{cases} \tag{4.1}$$

where $s_{ij}(t) = 1$ for ON-State and $s_{ij}(t) = 0$ for OFF-State of switch S_{ij} where 'i' corresponds to PC_i and $j \in \{1, 2\}$ is used to denote one of the two half-bridges in HB. Thus, all three modes of PC_i can be defined in terms of $s_i(t)$. This allows us to independently control each PC_i using $s_i(t)$. The input and output of ideal HB_i inside each PC_i are related through the switching function $s_i(t)$. Thus, the current through $Cell_i$, the voltage output from each PC_i, and the total voltage output from the MLC are given by

$$i_{Bi}(t) = i_L(t)s_i(t), \ v_{Li}(t) = V_{Bi}(t)s_i(t), \ v_L = \sum_{i=1}^{n} v_{Li} \tag{4.2}$$

If terminal voltages of all cells are equal then the MLC can generate $L = 2\,n + 1$ different voltage levels (v_L).

4.3 Features and Applications

The CHB-MLC has vast applications, for example in transportation, active rectifiers, interface of several renewable energy sources to the utility grid etc. The MLC has a modular structure and gives extra degree-of-freedom to achieve tighter control of the battery pack at cell or BSM level. Other major advantages are: it enables the replacement of IGBTs with low-voltage MoS-FET in high-voltage applications and thus reduces the switching losses and increases efficiency, reduces harmonic distortion in the output, may enable to use the same cooling system for the battery pack and the inverter, and reduces the electromagnetic interference due to low-level voltage switching in each PC_i. The main disadvantages compared to TLI are: the higher component count and large dc-link ripple at second-order baseband harmonic which cause extra losses in the battery (see Paper 2).

4.4 Switching and Averaged Models

The CHB MLC in our study has no dynamic state other than those of a battery. In this section we will present the switching and average models of each PC_i. These models describe the switched and averaged behavior of each $Cell_i$ respectively.

Switching Model of PC_i

Now using equations (4.2) in equations (2.1)–(2.5), we get the following model of the *switched battery behavior* under the switching action of PC_i and alternatively call it a *switched model of PC_i*.

$$\dot{T}_{si} = -a_{si}T_{si} + b_{si}i_L^2 s_i^2 + a_{si}T_{fi-1}, \tag{4.3}$$

$$\dot{V}_{i1} = -a_{ei1}V_{i1} + b_{ei1}i_L s_i, \tag{4.4}$$

$$\dot{V}_{i2} = -a_{ei2}V_{i2} + b_{ei2}i_L s_i, \tag{4.5}$$

$$\dot{\xi}_i = -b_{ei3}i_L s_i, \tag{4.6}$$

$$V_{Bi} = f(\xi_i) - V_{i1} - V_{i2} - b_{ri}i_L s_i \tag{4.7}$$

The input-output relation for each PC_i of MLC is now given by

$$v_{Li} = V_{Bi}s_i = \left(f(\xi_i) - V_{i1} - V_{i2}\right)s_i - b_{ri}i_L s_i^2. \tag{4.8}$$

and the instantaneous power delivered by each PC_i (or $Cell_i$) is given by

$$P_i = v_{Li}i_L = (f(\xi_i) - V_{i1} - V_{i2}) \, i_L s_i - b_{ri}i_L^2 s_i^2. \tag{4.9}$$

Averaged State-Space Model of PC_i

The CHB MLC is a variable structure dynamical system. Each PC_i has three different possible circuit configurations depending on the value of $s_i(t)$. Thus the MLC circuit is a piece-wise linear dynamical system whereas for a given discrete value of $s_i(t)$ the system is linear time-invariant. In this study the aim is to derive the optimal control policy using convex optimization approach which need a model with real-valued control signal because such models are far easier to handle in the optimization. In order to derive the averaged-model from the switching model (4.3)–(4.9), it is required to transform $s_i(t)$ and its all dependent signals to real-valued, averaged signals. The concept of averaging can be employed by assuming $F_s \gg f_L$, where F_s is switching frequency and f_L is bandwidth of the load, and then by using the two-time scale separation principle, see [62–64]. In simple words, it is assumed that the system response is determined predominantly by the average of $s_i(t)$. Before we derive averaged signals, we need three more assumptions (cf. Assumptions 1 to 3 in Section III.B in Paper 1): $s_i(t)$ either belongs to $\{0, 1\}$ or to $\{0, -1\}$ during any switching period $\Delta t \in \{t - T_s, t\}$ (Assumption-1), the load current $i_L(t)$ and the battery internal states remain fairly constant during any switching period Δt (Assumption-2 and -3). Now, using Assumption-1, the duty-cycle of PC_i defined by the average of the switching function $s_i(t)$ is given by

$$u_i(t) = \bar{s}_i(t) = \frac{1}{T_s} \int_{t-T_s}^{t} s_i(t) \mathrm{d}t = \pm \frac{T_{on}}{T_s} \tag{4.10}$$

where $T_{on} \in [0, T_s]$ is the time duration for which $s_i(t)$ is non-zero (i.e. ± 1) during any switching period. Now it can be clearly seen from (4.10) that depending on the value of T_{on}, $u_i(t)$ can attain any continuous real value in the interval $[-1, 1]$. Also note that $u_i \in (0, 1]$ means switching between Mode–1 and Mode–3 and $u_i \in [-1, 0)$ means switching between Mode–2 and Mode–3 and $u_i = 0$ corresponds to Mode–3. An example of averaging of a switching function is shown in Figure 4.2. Now all other averaged signals can be defined in terms of $u_i(t)$ and $i_L(t)$. The average current $\bar{i}_{Bi}$ flowing through $Cell_i$ during interval T_s is given by

$$\bar{i}_{Bi}(t) = \frac{1}{T_s} \int_{t-T_s}^{t} i_{Bi}(t) \mathrm{d}t = u_i \, i_L \tag{4.11}$$
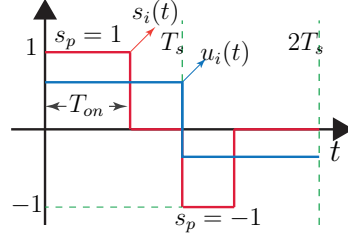
Figure 4.2: Averaging of switching function $s_i(t)$.

Similarly using assumption-3 and equation (4.7), the average terminal voltage of Cell$_i$ is given by

$$\bar{V}_{Bi} = \frac{1}{T_s} \int_0^{T_s} V_{Bi}\mathrm{d}t = f(\bar{\xi}_i) - \bar{V}_{i1} - \bar{V}_{i2} - b_{ri}i_L u_i \qquad (4.12)$$

which is now interpreted as the average voltage output of Cell$_i$ under the flow of average cell current $\bar{i}_{Bi}$. The average output voltage from PC$_i$ during period T_s of any switching cycle is now given by

$$\bar{v}_{Li} = \frac{1}{T_s} \int_0^{T_s} V_{Bi}s_i\mathrm{d}t = \left(f(\bar{\xi}_i) - \bar{V}_{i1} - \bar{V}_{i2} \right) u_i - b_{ri}i_L|u_i| \qquad (4.13)$$

and therefore the total output voltage from multi-level converter is given by

$$\bar{v}_L = \sum_{i=1}^n \left[\left(f(\bar{\xi}_i) - \bar{V}_{i1} - \bar{V}_{i2} \right) u_i - b_{ri}i_L|u_i| \right] \qquad (4.14)$$

In the switching thermal model (4.3), the quadratic quantity $i_{Bi}^2(t) = i_L^2 s_i^2$ is responsible for instantaneous heat generation inside the cell. For the averaged-model, we need to compute the corresponding average quantity which incurs the equivalent ohmic losses over one switching cycle. The root-mean-square (rms) current i_{Br_i} is that effective dc current given by

$$i_{Br_i}^2 = \frac{1}{T_s} \int_0^{T_s} i_{Bi}^2\mathrm{d}t = \frac{1}{T_s} \left(\int_0^{|u_i|T_s} s_i^2 \, i_L^2\mathrm{d}t + \int_{|u_i|T_s}^{T_s} 0\,\mathrm{d}t \right)$$

and using the assumptions, the above expression simplifies to

$$i_{Br_i}^2 = |u_i|i_L^2 = \left(\frac{T_{on}}{T_s} \right) i_L^2 \qquad (4.15)$$

Similarly, the average power being delivered by the PC$_i$ (or Cell$_i$) during the switching period T_s is now given by

$$\bar{P}_i = \bar{v}_{Li}i_L = \left(f(\bar{\xi}_i) - \bar{V}_{i1} - \bar{V}_{i2} \right) i_L u_i - b_{ri}i_L^2|u_i| \qquad (4.16)$$

35

Now using the averaged quantities (4.11) and (4.15), we get the following model of the *averaged battery behavior* in any PC_i and alternatively call it an *averaged model of PC_i*.

$$\dot{\bar{T}}_{si} = -a_{si}\bar{T}_{si} + b_{si}i_L^2|u_i| + a_{si}T_{fi-1} \tag{4.17}$$

$$\dot{\bar{V}}_{i1} = -a_{ei1}\bar{V}_{i1} + b_{ei1}i_L u_i \tag{4.18}$$

$$\dot{\bar{V}}_{i2} = -a_{ei2}\bar{V}_{i2} + b_{ei2}i_L u_i \tag{4.19}$$

$$\dot{\bar{\xi}}_i = -b_{ei3}i_L u_i \tag{4.20}$$

$$\bar{V}_{Bi} = f(\bar{\xi}_i) - \bar{V}_{i1} - \bar{V}_{i2} - b_{ri}i_L u_i \tag{4.21}$$

The average input-output relation for each PC_i of MLC is now given by

$$\bar{v}_{Li} = \left(f(\bar{\xi}_i) - \bar{V}_{i1} - \bar{V}_{i2}\right)u_i - b_{ri}i_L|u_i| \tag{4.22}$$

and the average power being delivered by each PC_i (or $Cell_i$) is given by

$$\bar{P}_i = \left(f(\bar{\xi}_i) - \bar{V}_{i1} - \bar{V}_{i2}\right)i_L u_i - b_{ri}i_L^2|u_i|. \tag{4.23}$$

4.5   Modulation Algorithms

The most common modulation strategies used for CHB MLC are multi-level carrier phase-shifted sine pulse-width modulation (PS-SPWM), SHE-PWM [23, 65–67] and SV-PWM [22, 23, 25, 68]. The modulation algorithms generate the switching function $s_{ij}(t)$ which gives the turn on/off timing instants to control the behavior of two switches of each half-bridge 'j' inside PC_i. The modulation algorithms use a reference signal (closed-loop or open-loop) to generate these switching functions. The inverter switching loss comparative analysis of these three modulation strategies for CHB MLC is given in [69]. In this section, only the multilevel PS-SPWM (PS-PWM), which is the most commonly used modulation algorithm for CHB-MLC in AC (DC) applications, will be discussed.

4.5.1   Phase-shifted SPWM Algorithm

The PS-SPWM, as shown in fig. 4.3(a) for 1-ϕ CHB MLC, is a natural extension of classical SPWM method which is widely used to operate TLCs. However, in contrast to TLCs (in which two-level modulation is used), three-level modulation is used instead for each PC_i of CHB MLC. In the constant frequency three-level SPWM method, the SPWM signal is generated for each half-bridge 'j' in each HB_i by comparing an adjustable

reference (modulating) sinusoidal signal $v_{rj}(t)$ with a constant frequency triangular carrier signal $v_{ci}(t)$ as follows

$$s_{ij}(t) = a + b\,\mathrm{sgn}(v_{rj}(t) - v_{ci}(t)), \ \forall i \in \{1, \cdots, n\}, \ \forall j \in \{1, 2\} \qquad (4.24)$$

where sgn is a signum function, a is a PWM dc-offset, b is a PWM scaling factor, $v_{rj}(t) = V_r \sin(\omega_r t + \theta_{rj})$ is a sinusoid with adjustable amplitude V_r and frequency ω_r, and $v_{ci}(t) = V_c f_t(w_c t + \theta_{ci})$ where f_t is a triangular function. In PS-SPWM scheme, the same set of $v_{rj}(t)$ are used for each PC_i with θ_{rj} given by[1]

$$\theta_{rj} = \begin{cases} 0, & \text{for } j = 1 \\ -\pi, & \text{for } j = 2 \end{cases} \qquad (4.25)$$

The carrier signals $v_{ci}(t)$ for each PC_i differ only in their phase shifts θ_{ci}. The θ_{ci} for each PC_i that gives the lowest distortion in the output stepped-waveform is given by the following relation[2] [23, 70, 71]

$$\theta_{ci} = \frac{\pi(i-1)}{n}, \ \forall i \in \{1, \cdots, n\} \qquad (4.26)$$

Thus, the complete switching function $s_i(t)$ is simply calculated using equations (4.1), (4.24) and (4.26). The PS-SPWM based $s_1(t)$ for PC_1 is shown in fig. 4.3(b). Note that the frequency ω_o of the output ac waveform will be equal to frequency ω_r of the reference waveform whereas the amplitude V_o of the output will be proportional to the amplitude V_r of the reference waveform. Thus, the reference waveform $v_{rj}(t)$ can be considered as an intermediate command or control signal. It is usually given by a high-level control block that adjusts its amplitude and frequency using some feedback information from the load. Note that in the case of dc applications, a dc-voltage control signal is used as a reference instead of sinusoidal waveform and the algorithm is called PS-PWM. Figure 4.4 shows the total output voltage waveform synthesized by CHB MLC using PS-SPWM scheme.

Remark 4.1. *Note that the PS-SPWM scheme uses a reference signal with the same frequency and amplitude and a carrier signal with the same frequency and amplitude for all PCs in each phase. In 3-ϕ applications everything else remains the same for all phases except the phase difference of $\frac{2\pi}{3}$ between reference waveforms of three phases. Thus the total average output power from CHB-MLC is evenly distributed among all PCs. In other words, each PC_i delivers/absorbs the same amount of average power during each switching cycle. Thus all switches and **cells/BSMs are uniformly used**. In this thesis, we alternatively denote PS-SPWM scheme as **UDCO** (uniform duty cycle operation) policy.*

---

[1]Note that θ_{rj} is denoted as θ_{oj} in Paper 2.

[2]Note that θ_{ci} given by (6) in Paper 2 is incorrect, but it does not affect our results.

Remark 4.2. *In this study, the analysis is done based on the assumption of natural sampling of the reference signal. The natural sampling assumes the ideal analog implementation of mathematical signum function i.e. $s_{ij}(t)$ switches its sign instantaneously at the intersection of $v_{rj}(t)$ and $v_{ci}(t)$. This type of PWM is called the naturally-sampled SPWM.*
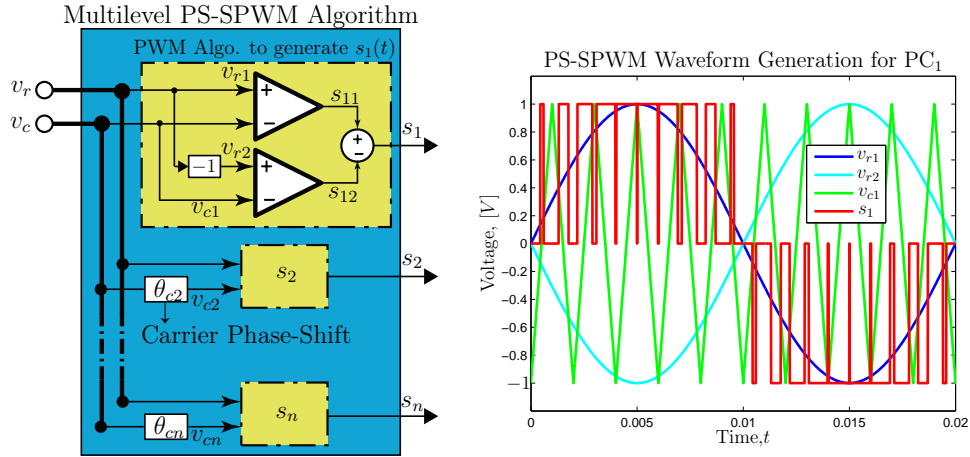
(a) Mutlilevel PS-SPWM Algorithm for MLC.

(b) Output of PS-SPWM algorithm. The waveform $s_1(t)$ along with its constituent signals is shown as an example.

Figure 4.3: PS-SPWM Generation for 1-ϕ MLC.
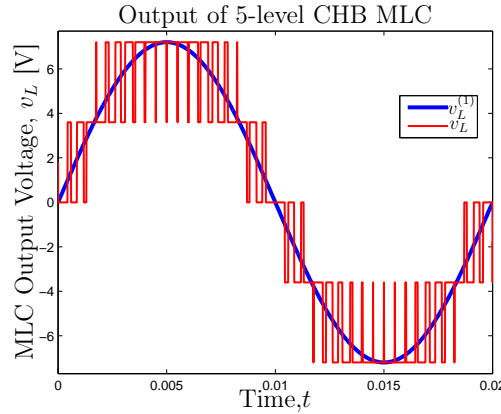
Figure 4.4: Output voltage synthesis in 5-level 1-ϕ MLC. Note that $v_L(t)$ is the PS-SPWM modulated actual output waveform whereas $v_L^{(1)}(t)$ is its fundamental sinusoidal component seen by a load acting as a low-pass filter.

Chapter 5

MLC as Integrated Cell Balancer and Motor Driver

Thermal, SOC and DOD imbalances, as discussed in Chapters 2 and 3, are inevitable in long strings of series-connected cells. Thus, *thermal and SOC balancer* is very important for large battery packs of xEVs as they are constructed from many such long strings of cells. In this thesis, we have evaluated the MLC as an integrated cell balancer and motor driver. The purpose is to drive the EM and to achieve simultaneous thermal and SOC balancing of the BSM using single hardware. The potential benefits of MLC, as an integrated cell balancer and driver, have been evaluated in particular for an application involving dc machine as a load. This study shows a great balancing potential of MLC. However, in applications involving three-phase ac machine, the MLC, in addition to its great balancing potential, also poses serious issues of extra battery heating and of extra capacity fading due to dc-link ripple current. In the following, we will give a brief snapshot of these two aspects.

5.1 DC Applications: Simultaneous Thermal and SOC Balancing Potential

The CHB-MLC provides a large redundancy in synthesizing the output voltage, which gives extra degree-of-freedom in control. The UDCO control policy, discussed in the previous Chapter, uses all cells of a BSM uniformly. However, this policy does not make the best use of extra degree-of-freedom of MLC and is thus not optimal for achieving the objectives of thermal and SOC balancing in a BSM with parametric variations. The optimal strategy is to use each cell of the BSM according to its internal state (SOC, SOH, and temperature etc.) by making the best use of the extra degree-of-freedom

to achieve the objectives of balancing as well as the satisfaction of driving constraints. This may result in a *nonuniform use of cells* depending on the *degree of nonuniformity* among them. The *first research task* in this thesis is to devise such an optimal feedback control policy (OP). In *Paper 1*, we have formulated an MLC-based OP which *uses each cell in a BSM according to its SOC level and temperature* to keep SOC and temperature deviations among cells within certain limits. The OP is computed by solving a *convex optimization problem* based on the assumption of perfect information of the SOC and temperature of each cell, as well as of the future driving. The *research task* is to investigate if OP gives a significant benefit compared to UDCO under both unidirectional and reciprocating coolant flow (UF and RF). For simplicity, in this first study the EM is assumed to be a dc machine and the cells are modeled using equivalent circuit approach. The mathematical tool of *convex optimization* is reviewed in Chapter 6.

5.1.1 Optimization Problem

The simultaneous thermal and SOC balancing problem has been formulated as the following optimization problem.

$$\text{minimize} \int_0^{t_f} \sum_{i=1}^n \sum_{j=1}^n \alpha_{ij} \big(\bar{T}_{si}(t) - \bar{T}_{sj}(t)\big)^2 \, \mathrm{d}t, \ \forall t \in [0, t_f], \ \forall i, j \in \{1, \cdots, n\}$$

subject to

$$\begin{cases}
\dot{\bar{T}}_{si}(t) = -a_{si}\bar{T}_{si}(t) + b_{si}i_L^2(t)|u_i(t)| + a_{si}T_{fi-1}, \\
\dot{\bar{V}}_{i1}(t) = -a_{ei1}\bar{V}_{i1}(t) + b_{ei1}i_L(t)u_i(t), \\
\dot{\bar{V}}_{i2}(t) = -a_{ei2}\bar{V}_{i2}(t) + b_{ei2}i_L(t)u_i(t), \\
\dot{\bar{\xi}}_i(t) = -b_{ei3}i_L(t)u_i(t), \\
\bar{v}_L(t) = \sum_{i=1}^n \Big[\big(f(\bar{\xi}_i(t)) - \bar{V}_{i1}(t) - \bar{V}_{i2}(t)\big) u_i(t) - b_{ri}|u_i(t)|i_L(t) \Big] = v_{Ld}(t), \\
-\Delta SOC \le \big(\bar{\xi}_i(t) - \bar{\xi}_j(t)\big) \le \Delta SOC, \ \bar{\xi}_i(t_f) = \bar{\xi}_j(t_f), \ \ 0 \le \bar{\xi}_i(t) \le 1, \\
-\Delta T_s \le \big(\bar{T}_{si}(t) - \bar{T}_{sj}(t)\big) \le \Delta T_s, \ \bar{T}_{si}(t) \le T_{smax}, \\
u_i(t) \in [-1, 1], \ \bar{i}_{Bi}(t) = i_L(t)u_i(t) \in [\bar{i}_{Bimin}, \bar{i}_{Bimax}], \\
\text{where} \ i_L(t), v_{Ld}(t) \ \text{and} \ T_{fi-1} \ \text{are known at each time instant.}
\end{cases}$$

(P-I)

with optimization variables $\bar{T}_{si}(t), \bar{V}_{i1}(t), \bar{V}_{i2}(t), \bar{\xi}_i(t)$, and $u_i(t)$. Note that α_{ij} is a penalty weight on each temperature deviation $\Delta \bar{T}_{sij} = \bar{T}_{si} - \bar{T}_{sj}$ and $\bar{v}_L(t) = v_{Ld}(t)$ defines an output voltage tracking constraint where $v_{Ld}(t)$ is the known demanded load voltage. The optimization problem (P-I) is originally non-convex. The non-convexity arises due to $|u_i(t)|$ term in the first

and fifth equality constraints. The multiplication of optimization variables in the fifth equality constraint is another reason for the non-convexity. The *problem has been convexified* by pre-deciding the sign of $u_i(t)$ at each time instant based on the sign of known $v_{Ld}(t)$, by neglecting the activation and concentration polarization losses ($\bar{V}_{i1}(t)$ and $\bar{V}_{i2}(t)$) in the battery, and by assuming the open-circuit voltage $V_{oci} = f(\bar{\xi}_i(t))$ as constant.

Snapshot of Some Simulation Results

Some of the simulation results are shown in Figure 5.1. Note that the internal resistance R_{s5} of Cell$_5$ is assumed in this simulation study to be almost 50% higher than other cells due to some nonuniform ageing effects in the BSM. Figure 5.1(a) shows the tracking response of average output voltage $\bar{v}_L(t)$, synthesized by the MLC, to changes of the demanded input voltage $v_{Ld}(t)$ of a dc machine. The Figure shows good tracking performance with very small error. Figure 5.1(b) and 5.1(c) show temperatures and SOC of all cells for OP under unidirectional coolant flow (UF). The average temperature $\breve{T}_{si} = \frac{1}{N}\sum_{k=0}^{N}\bar{T}_{si}(k)$ of each Cell$_i$ over entire drive cycle of length N as a function of increase in R_{s5} is also shown in Figure 5.1(d). From all these figures, it is clear that OP has achieved good thermal balancing while keeping temperatures of all cells within $\pm 2°$C zone and SOC within $\pm 10\%$ from each other. Figure 5.1(e) shows the average duty cycle $\bar{u}_i = \frac{1}{N}\sum_{k=0}^{N}u_i(k)$ of each Cell$_i$ over entire driving horizon. The horizontal dashed black line shows the average duty $\bar{u}_i^u$ for UDCO policy and colored vertical bars shows the optimal average duty cycle $\bar{u}_i^o$ for OP scheme. This figure suggests that thermal and SOC balancing has been achieved by using just *slight nonuniformity in the time-usage of cells*. However, we can get more accurate picture by looking at the *normalized average power loss per unit ohm* (denoted by $\bar{I}_i$ and defined by equation (45) in Paper 1) of any Cell$_i$ over the whole driving horizon as shown in figure 5.1(f). The horizontal dashed black line shows the average unit power loss $\bar{I}_i^{ur}$ across Cell$_i$ for UDCO policy and colored vertical bars show the optimal average unit power loss $\bar{I}_i^{or}$ across Cell$_i$ for OP scheme. This figure shows relatively *significant nonuniformity in the power loss distribution* among cells. This suggests that the OP in fact achieves thermal balancing by avoiding the use of higher resistance Cell$_5$ during peak power intervals and using the cell more frequently during low power intervals. This policy is naturally optimal as losses are quadratic in current. Thus, we can conclude that for ideal cell balancing, the *load scheduling of cells* as per their states and operating conditions is more important than just their nonuniform time-usage.
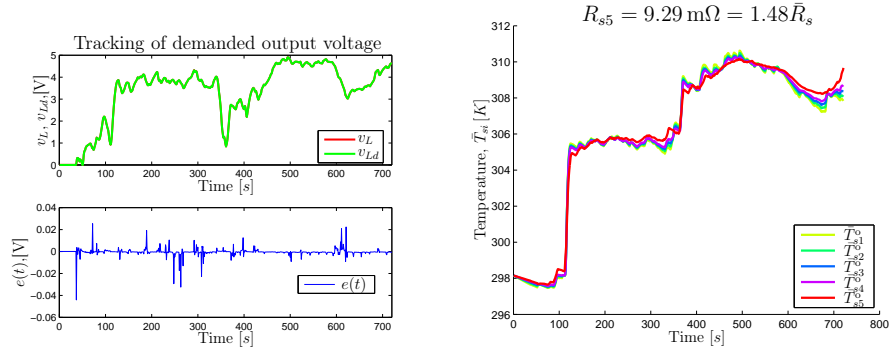
(a) Figure shows that the MLC using the optimal policy tracks the demanded output voltage $v_{Ld}(t)$ with very small error.

(b) Optimal Temperature of each cell for OP. Despite R_{s5} being 50% higher, OP has successfully achieved thermal balancing among all cells.
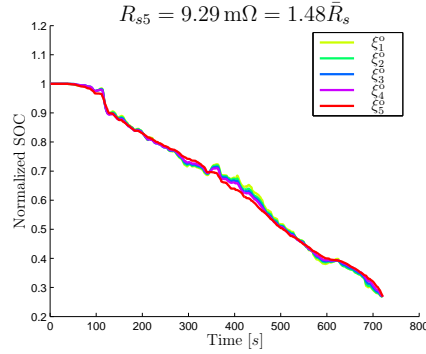
(c) Optimal SOC of each cell for OP.
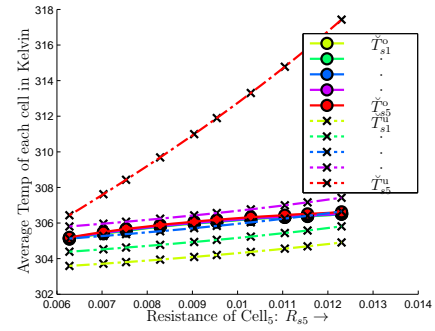
(d) Variation in average temperature, during drive cycle, of cells as a function of R_{s5} for both OP and UDCO.
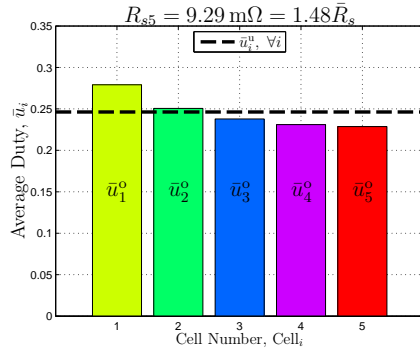
(e) Optimal average duty cycles $\bar{u}_i^o$ of each Cell_i computed by OP. The dashed horizontal black line shows the uniform average duty cycle computed by UDCO.
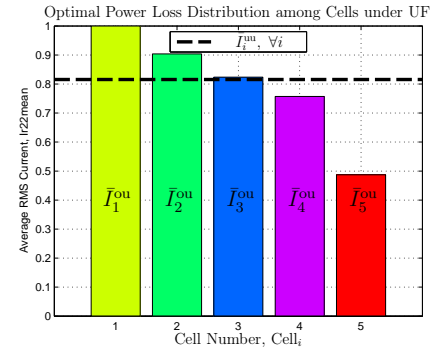
(f) Optimal normalized average power loss per unit ohm across each Cell_i for OP under UF. The dashed horizontal black line shows normalized unit power loss across each Cell_i for UDCO.

Figure 5.1: Simulation results and comparison between OP and UDCO. The plots show that despite the resistance (R_{s5}) of the most down stream Cell_5 being 50% higher compared to other cells, OP has still successfully achieved simultaneous thermal and SOC balancing among all cells whereas uniform use of cells is naturally not optimal in this situation.

5.2 Three-phase AC Applications: Issues of DC-link Ripple

In xEVs, 3-ϕ permanent magnet synchronous machines (PMSM) are generally used, requiring 3-ϕ voltage inverter. An *ideal 3-ϕ inverter, for a given load power, should only draw a constant dc current from the battery pack* as the ripple superimposed on the dc-level always increases losses in the cells. For example, an ideal 3-ϕ TLC draws almost constant power from a battery pack, see [25], [26]. Reactive power also flows in 3-ϕ TLC, however, the batteries do not see this reactive power by the virtue of topology and the symmetrical fast switching in *three phase-legs*. Under ideal conditions almost all the reactive power instantaneously shuffles between three phases and hence the bidirectional fluctuating power never flows back and forth between the battery pack and the load.

The 3-ϕ MLC has been proposed, as an alternative to 3-ϕ TLC, by [24] to directly drive 3-ϕ PMSM. The authors motivated for 3-ϕ MLC based on its benefits of relatively low harmonics for EM as well as its advantages for battery control due to the modularity offered by the MLC. This modularity and extra DOF, similar to DC and 1-ϕ applications, can indeed be exploited to achieve cell level control and optimization of battery packs in 3-ϕ applications.

However, in this thesis (see Paper 2 and Appendix A), we show analytically that the modularity in 3-ϕ MLC brings with it a big disadvantage of fluctuating power flow from each cell. This has some serious repercussions compared to the case of 3-ϕ TLC. The reason for this fluctuating power is that each HB$_i$ inside PC$_i$ consists of only *two phase-legs* which are switched 180° apart electrically and thus the current drawn from the cell cannot be constant. The fluctuating power from each Cell$_i$ originates from dc-link switching current ripple harmonics whose one major component lies at 2nd baseband harmonic frequency. The 2nd baseband ripple frequency is a *function of machine speed* and it is superimposed on the constant dc current level whose value is a function of power factor angle θ (see equation (5.5) on page 45). The dc-link ripple, *regardless of θ value*, would always incur *additional losses* in each Cell$_i$ of the BSM and increase its temperature. In addition to additional battery heating, ripple current also causes each Cell$_i$ to *process extra Ah-throughput* as soon as the fluctuating power output from Cell$_i$ becomes *bidirectional* for $\theta > 0$. The magnitude of this extra Ah-throughput is a function of θ and thus it becomes quite significant when the EM has to operate at low power factor especially in the field weakening region.

The battery operation at elevated temperature has detrimental impact

on its life-time, see Chapter 2. Similarly, the extra Ah-throughput accelerates the capacity fading as predicted by the cycle-life model (2.8). Therefore, there is a big drawback of 3-ϕ MLC circuit topology for battery life. The *second research task* in this thesis is to investigate how detrimental is this ripple for battery in 3-ϕ MLC, see Paper 2 and Appendix A respectively for detailed discussion on the impact of the ripple on battery heating and capacity fading.

In order to investigate and exactly characterize the side effect of ripple in the battery of 3-ϕ MLC, the spectrum of the ripple has been calculated first and then compensated using a dc-link capacitor. The machinery of double Fourier series has been used to analytically calculate the dc-link harmonic content. The method of double Fourier series is reviewed in Chapter 6.

DC-link Current Harmonic Analysis

In this subsection, we will give a short preview of some results of our investigation of issues related to dc-link ripple current. Let us consider a three-phase permanent magnet synchronous machine being driven by a 3-ϕ MLC. Assume the output load current in all phases is perfectly sinusoidal with frequency ω_o and the phase angle (also called power factor angle) θ with respect to the phase-voltage. Thus, the current in phase-a is given by (current in other two phases are phase-shifted by $2\pi/3$ and $-2\pi/3$)

$$i_a(t) = \sqrt{2}I_a \cos(x_a(t)) \tag{5.1}$$

where $x_a(t) = \omega_o t + \theta$. Now using the double Fourier series representation of a switching function s_i (obtained by applying eq. (6.4) in Chapter 6 for each phase-leg 1 and 2 inside each PC$_i$), the dc-link current in each PC$_i$ is given by (see Paper 2 and Appendix A for detailed derivation.)

$$i_{dci}(t) = s_i(t)i_a(t) = \frac{M_o I_a}{\sqrt{2}}\cos(\theta) + \frac{M_o I_a}{\sqrt{2}}\cos(2\omega_o t + \theta)$$

$$+ \frac{2\sqrt{2}I_a}{\pi}\left[\sum_{k=1}^{\infty}\frac{1}{k}\left\{J_1\left(a_k\right)\sin\left(b_{k,1}\right)\left[\cos(k\omega_c t - \theta) + \cos\left((k\omega_c + 2\omega_0)t - \theta\right)\right]\right.$$

$$+ J_{-1}\left(a_k\right)\sin\left(b_{k,-1}\right)\left[\cos(k\omega_c t + \theta) + \cos\left((k\omega_c - 2\omega_0)t - \theta\right)\right]\right\}$$

$$+ \sum_{k=1}^{\infty}\sum_{\substack{l=-\infty \\ l\neq 0 \\ l\neq\pm 1 \\ l=\text{odd}}}^{\infty}\left\{\frac{1}{k}J_l\left(a_k\right)\sin\left(b_{k,l}\right)\left[\cos\left((k\omega_c + (l-1)\omega_0)t - \theta\right)\right.\right.$$

$$+ \cos\left((k\omega_c + (l+1)\omega_0)t + \theta\right)\Big]\Big\}\Bigg] \tag{5.2}$$

where $a_k = (k\frac{\pi}{2}M_o)$, and $b_{k,l} = (k+l)\frac{\pi}{2}$. Since '$l$' is odd thus both '$l-1$' and '$l+1$' are even integers. It means the total carrier side-band harmonic energy is contained only by even carrier side-bands. In order to characterize the carrier harmonics we note that the coefficient

$$\frac{1}{k}J_l\left(k\frac{\pi}{2}M_o\right)\sin\left([k+l]\frac{\pi}{2}\right) = 0, \forall\,(k+l) \in 2\mathbb{Z} \tag{5.3}$$

where $\mathbb{Z}$ is the set of all integers. Since 'l' is odd thus '$k+l$' is even for all odd k:s, thus

$$\frac{1}{k}J_l\left(k\frac{\pi}{2}M_o\right)\sin\left([k+l]\frac{\pi}{2}\right) = 0, \forall k \in 2\mathbb{Z}+1 \tag{5.4}$$

Therefore, all odd carrier harmonics and their sidebands are zero. Now, it is obvious from equations (5.2) and (5.4) that the dc-link current in any PC_i of 3-ϕ MLC consists of a dc component, large 2nd baseband harmonic, and all even carrier harmonics along with their even sidebands[1]. Now, assuming a very high switching frequency, all the carrier and sideband harmonics can be easily filtered, using a very small capacitor, and can thus be neglected in the analysis. Therefore, the equation (5.2) can be further simplified to

$$i_{dci}(t) \approx \bar{I}_{dci}(\theta) + \tilde{i}_{dci}(t) = \frac{M_oI_a}{\sqrt{2}}\cos(\theta) + \frac{M_oI_a}{\sqrt{2}}\cos(2\omega_ot + \theta) \tag{5.5}$$

where $w_o = 2\omega_m$ is the electrical angular frequency being fed to a two-pole permanent magnet synchronous machine operating at the angular speed ω_m. Equation (5.5) shows that the dc-link current at the PC_i input consists of two components: the pure dc-component $\bar{I}_{dci}$ and the pure ac-component $\tilde{i}_{dci}(t)$, at second baseband harmonic frequency, with root-mean-square (rms) value $\tilde{I}_{dcir}$. Note that the amplitude of this ac-component is equal to that of dc-component at $\theta = 0$. The total dc-link current $i_{dci}(t,\theta) = \bar{I}_{dci}(\theta) + \tilde{i}_{dci}(t)$ is plotted in Figure 5.2 along with its dc-component (average value) $\bar{I}_{dci}(\theta)$, and its rms value $I_{dcir}(\theta) = \sqrt{\bar{I}_{dci}^2 + \tilde{I}_{dcir}^2}$ for various values of power factor angle θ. The average and rms values of $i_{dci}(t,\theta)$ vary at different rates as a function of θ, as shown in the figure, resulting in increase in their difference as θ increases. This also causes the flow of bidirectional current in the battery (note *micro-charging/discharging cycles* in the figure) whose magnitude increases with increase of θ. The average value of current does the actual work (or transfer the useful unidirectional power) whereas the rms value incurs the ohmic losses. Thus, the dc-link ripple current causes the MLC battery to generate *extra heat* and to process *extra*

---

[1]Note that the statement regarding carrier harmonics and sidebands was wrong in Paper 2, but it does not affect results.
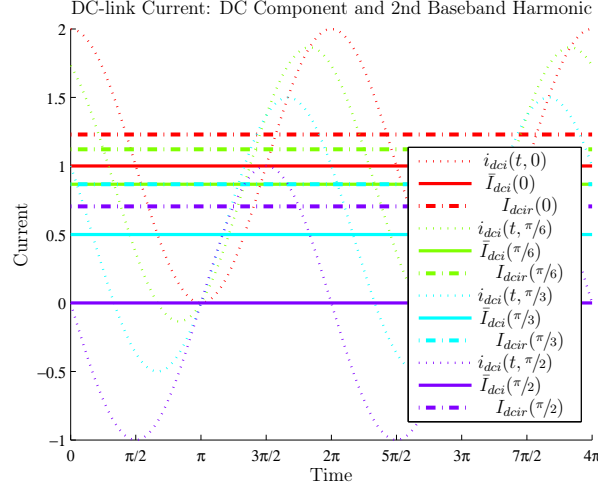
Figure 5.2: *Battery ripple without compensator.* The total dc-link current $i_{dci}(t,\theta) = \bar{I}_{dci}(\theta) + \tilde{i}_{dci}(t)$, its dc component (average value) $\bar{I}_{dci}(\theta)$, and its rms value $I_{dcir}(\theta)$ are shown as a function of power factor angle θ. Note the micro-cycles and the difference in dc and rms values of current.

Ah-throughput (due to bidirectional current flow) relative to the amount of useful work. One of these conclusions, i.e., the one regarding extra battery heating inside MLC, has also been validated experimentally in [72]. Therefore, this ripple must be compensated otherwise it would accelerate the battery ageing as predicted by the cycle-life model (2.8)[2]. In Paper 2 and Appendix A, the effectiveness of a *passive compensation* based on a dc-link shunt capacitor has been thoroughly investigated. The battery ripple as a function of passive compensation network parameters and power factor angle θ has been thoroughly analyzed. In particular, the impact of ripple on the ageing of MLC battery due to its extra ampere-hour throughput is discussed in Appendix A, which is an extension of results from Paper 2.

Remark 5.1. *Note that the passive compensation based on dc-link capacitor, as shown in Paper 2, may not be feasible in vehicles due to the need of unreasonably big dc-link capacitor. Thus, the dc-link ripple must be compensated using some other methods before promoting it as an integrated cell balancer and driver. We can use extra cooling power to compensate the extra heating generated inside battery due to the ripple. However, firstly this approach may cost extra fuel and secondly it can not compensate the extra capacity fading arising from extra Ah-throughput of the MLC battery.*

---

[2]Note that this theoretical assessment requires a careful experimental validation to ascertain the exact impact of this variable frequency ripple on battery ageing.

Chapter 6

Mathematical Tools

In this chapter, we will give a brief review of convex optimization and double Fourier series methods, which are the two main mathematical tools used for analyses in Paper 1 and 2, respectively.

6.1 Evaluation of Cell Balancing using MLC

The CHB-MLC can generate the demanded output voltage for EM at each time instant using various combinations of modes of PCs. This extra DOF may be exploited to simultaneously achieve the objective of thermal and SOC balancing. However, the natural question that arises is how to make the best use of this extra DOF. In the following we briefly review a mathematical tool of convex optimization which answers this question. We have employed this tool in Paper 1 to choose the best MLC circuit configuration at each sampling instant, using full future driving information, to evaluate the maximum cell balancing potential that MLC can offer while simultaneously satisfying the motor driving constraints.

6.1.1 Convex Optimization

Convex optimization is a mathematical tool that helps in making globally optimal decisions. Before stating the standard form of the convex problem, some related terms are defined as given below.

Convex Sets and Convex Functions

Definition 1. *The set $\mathcal{C} \subseteq \mathbb{R}^n$ is convex if for any $x, y \in \mathcal{C}$ and any $\theta \in [0, 1]$ it holds that $\theta x + (1 - \theta)y \in \mathcal{C}$.*
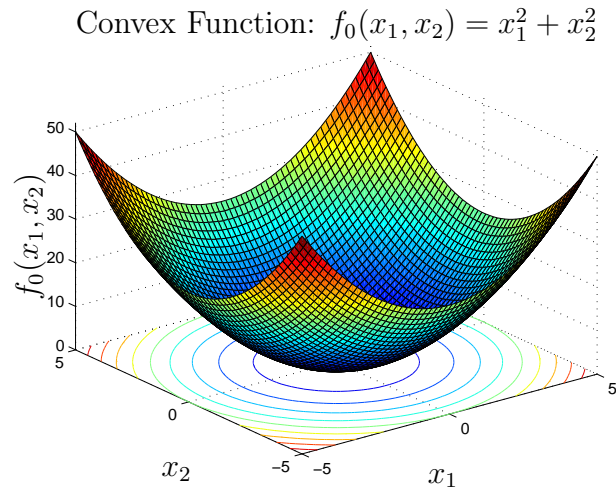
Figure 6.1: Example of convex objective function and convex sets. Note that each contour (or level curve) of $f_0(x)$ defines the boundary of a level set. The level sets of convex functions are convex.

Definition 2. *A function $f : \mathbb{R}^n \to \mathbb{R}$ is convex if $\operatorname{dom} f$ is a convex set and if for all $x, y \in \operatorname{dom} f$ and $\theta \in [0, 1]$ the following inequality holds*

$$f(\theta x + (1 - \theta)y) \leq \theta f(x) + (1 - \theta)f(y)$$

In simple terms, the convex set is a set of points such that if we connect any two points in the set using line segment then each point on that line segment should also be inside the set. The definition 2, in simple terms, says that if we connect any two points x and y on a function curve using a straight line then the chord defined by this line must be above or equal to the function curve for each point on the chord. A strictly convex function always has a global minimum and a positive curvature. An example of a convex function $f_0(x)$ in 3D is shown in fig. 6.1. Each level set, $\mathcal{C}_\alpha = \{x \in \mathcal{C} | f_0(x) \leq \alpha\}$, of $f_0(x)$ is a convex set and is also shown in fig. 6.1 where each contour (or level curve) of $f_0(x)$ defines a boundary of $\mathcal{C}_\alpha$.

Standard Form of a Convex Problem

A standard convex optimization problem is formulated on the following form

$$
\begin{aligned}
\text{minimize} \quad & f_0(x) \\
\text{subject to} \quad & f_i(x) \leq 0, \quad \forall i \in \{1, \cdots, m\} \\
& h_j(x) = 0, \quad \forall j \in \{1, \cdots, p\} \\
& x \in \mathcal{X}
\end{aligned}
\tag{P-I}
$$

where $f_0(x)$ is an objective function, $f_i(x)$ and $h_j(x)$ define inequality and equality constraints respectively, $x \in \mathbb{R}^n$ is a vector of decision variables and $\mathcal{X} \subseteq \mathbb{R}^n$ is a domain of the problem i.e. the set of all decision vectors where functions $f_i(x)$ and $h_j(x)$ are defined. The problem (P-I) is convex if $\mathcal{X}$ is convex, $f_i(x)$, $\forall i \in \{0, \cdots, m\}$ are convex and $h_j(x)$, $\forall j \in \{1, \cdots, p\}$ are affine in x. For example, in the MLC-based optimal cell balancing problem, the decision vector consists of $3nN$ variables (2 states and 1 control for each of n cells at each time instant) over the whole time horizon N, whereas the constraints and objective function come from cell balancing and driving requirements and the battery system dynamics.

Merits and Demerits of Convex Optimization

- Formulating and solving a convex optimization problem guarantees global optimality.

- Convex optimization ensures very short computation time, which is typically polynomial in the number of optimization variables.

- Convex optimization problem can be parameterized by component design parameters like size of machine, battery etc.

- It is not always possible to transform all optimization problems to the standard convex optimization form. In certain cases, some approximations are done to convexify the original problem. For example, we may have to simplify the model of a system or relax some hard equality constraints.

- Since the set of integers is not convex, integer decision variables are not allowed inside convex optimization problems. In some cases, these variables can be pre-decided by *heuristic methods* and then the remaining problem is solved as a convex sub-problem [73]. In case of binary variables, we can also employ the concept of boolean relaxation in which instead of using the discrete set $\{0, 1\}$, we do relaxation and use the real set $[0, 1]$. In MLC-based cell balancing problem, we use the averaged state-space model in order to avoid the difficulty of handling discrete switching function $s_i(t)$ in convex optimization.

6.2 DC-link Ripple Analysis

In this section, the method of double Fourier series is reviewed. The method has been used in Paper 2 to analytically characterize the nature of dc-link harmonic content.

6.2.1 Double Fourier Series Method

The double Fourier series method is a generalization of the conventional Fourier series analysis (for single-variable functions) to two-dimensional functions. The double Fourier series method was originally developed by H.S. Black [74] for the analysis of modulation processes in communication systems. This method was later adopted by S.R. Bowes et. al. [75] for the analysis of harmonic spectrum of PWM signals and that of output voltages in power converters. The double Fourier series analysis assumes a signal waveform $f(t) = f(x(t), y(t))$ which is a function of two other independently periodic signals $x(t)$ and $y(t)$. The signals $x(t)$ and $y(t)$ can be considered as either being themselves periodic or the independent variables of other periodic signals $f_c(x(t))$ and $f_r(y(t))$ respectively. The harmonic spectrum of any $f(x(t), y(t))$ is given by the following general double Fourier series representation [76]

$$f(x(t), y(t)) = \underbrace{\frac{A_{00}}{2}}_{\text{DC Offset}} + \underbrace{\sum_{l=1}^{\infty}\left[A_{0l}\cos(ly) + B_{0l}\sin(ly)\right]}_{\text{Fundamental and Baseband Harmonics}}$$

$$+ \underbrace{\sum_{k=1}^{\infty}\left[A_{k0}\cos(kx) + B_{k0}\sin(kx)\right]}_{\text{Carrier Harmonics}}$$

$$+ \underbrace{\sum_{k=1}^{\infty}\sum_{\substack{l=-\infty \\ l\neq 0}}^{\infty}\left[A_{kl}\cos(kx+ly) + B_{kl}\sin(kx+ly)\right]}_{\text{Carrier Sideband Harmonics}} \quad (6.1)$$

where 'l' is the baseband harmonic index variable, 'k' is the carrier harmonic index variable, and A_{kl} and B_{kl} are Fourier coefficients given by

$$A_{kl} = \frac{1}{2\pi^2}\int_{-\pi}^{\pi}\int_{-\pi}^{\pi} f(x(t), y(t))\cos(kx+ly)\mathrm{d}x\mathrm{d}y \quad (6.2a)$$

$$B_{kl} = \frac{1}{2\pi^2}\int_{-\pi}^{\pi}\int_{-\pi}^{\pi} f(x(t), y(t))\sin(kx+ly)\mathrm{d}x\mathrm{d}y \quad (6.2b)$$

In this study, the dc-link ripple analysis is done assuming the switches being modulated using PS-SPWM scheme, see section 4.5.1. In PS-SPWM algorithm, the switching function $s_{ij}(t) = f(v_{ci}(t), v_{rj}(t))$ is a function of two independently periodic signals namely sinusoidal reference signal $v_{rj}(t)$ and triangular carrier signal $v_{ci}(t)$ which are given by

$$v_{rj}(t) = \bar{V}_{r0} + V_r\sin(y_j(t)), \quad v_{ci}(t) = \bar{V}_{c0} + V_cf_t(x_i(t)) \quad (6.3)$$

where $x_i = \omega_c t + \theta_{ci}$ and $y_j = \omega_r t + \theta_{rj}$ have been previously defined in section 4.5.1, $\bar{V}_{r0}$ and $\bar{V}_{c0}$ are dc-offsets in the reference and carrier signals, and $f_t \in [-1, 1]$ is a triangular function. Note that the dc-offsets are defined depending on whether the PWM is unipolar or bipolar. In case of bipolar PWM, the dc-offsets are zero. The calculation of Fourier coefficients A_{kl} and B_{kl} is generally a tedious process and depends on the type of PWM scheme. However, the double Fourier series representation of a bipolar triangular SPWM is now well known and is given by, see [76–78]

$$s_{ij}(t) = \frac{M_o}{2}\cos(y_j) + \frac{2}{\pi}\sum_{k=1}^{\infty}\left[\frac{1}{k}J_0\left(k\frac{\pi}{2}M_o\right)\sin\left(k\frac{\pi}{2}\right)\cos\left(kx_i\right)\right]$$
$$+ \frac{2}{\pi}\sum_{k=1}^{\infty}\sum_{\substack{l=-\infty \\ l\neq 0}}^{\infty}\left[\frac{1}{k}J_l\left(k\frac{\pi}{2}M_o\right)\sin\left([k+l]\frac{\pi}{2}\right)\cos\left(kx_i + ly_j\right)\right] \quad (6.4)$$

where $J_l(\xi_k)$, shown in fig. 6.2 as a function of carrier harmonic index 'k', is a Bessel function of the first kind with order l and argument $\xi_k = kM_o\frac{\pi}{2}$ where $M_o = \frac{V_r}{V_c}$ is the modulation index. We have used equation (6.4) in Paper 2 to derive an expression for dc-link ripple current.
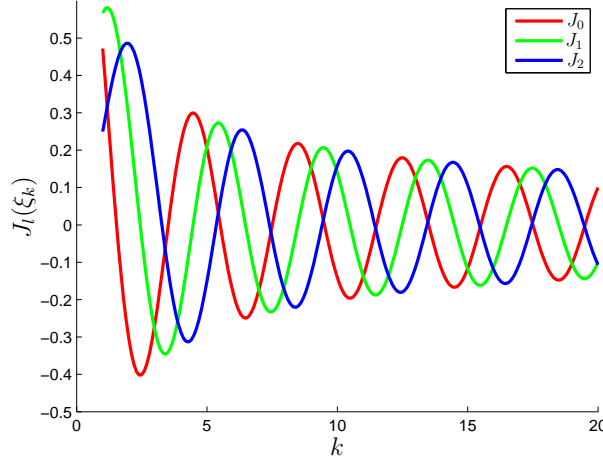
Figure 6.2: Bessel function of first kind with order 'l'.

Chapter 7

Summary of Included Papers

This chapter provides a brief summary of the papers that constitute the base for this thesis. Full versions of the papers are included in Part II. The papers have been reformatted to increase readability and to comply with the layout of the rest of the thesis.

Paper 1

> F. Altaf, L. Johannesson, B. Egardt, "On Thermal and State-of-Charge Balancing using Cascaded Multi-level Converters," *Journal of Power Electronics*, vol. 13, Issue 4, pp. 569-583, 2013.

In Chapter 3, we showed that thermal and SOC imbalance is detrimental for battery pack lifetime and its total capacity. In Chapter 4, we proposed to use CHB-MLC, which has a special modular structure and provides full DOF in cell-level battery control, to achieve simultaneous thermal and SOC balancing in the BSM. In Paper 1, we have investigated the potential benefit of optimally using this extra DOF of MLC for simultaneous thermal and SOC balancing of cells in an air-cooled BSM under both unidirectional and reciprocating air-flow (UF and RF). In this study, the electric machine is assumed to be a DC machine, the cells inside the BSM are modeled using equivalent circuit approach, and the simulation study is focused only on an air-cooled BSM with 5 series-connected cells. The coolant flow is assumed to be laminar with known inlet temperature and speed. Firstly, a control-oriented averaged state-space electro-thermal model of an air-cooled BSM is derived under the switching action of MLC. Secondly, an MLC-based optimal control policy (OP) is computed by solving a convex optimization problem based on the assumption of perfect information of the SOC and temperature of each cell, as well as of the future driving. The performance of

MLC-based OP under both UF and RF is investigated to evaluate its potential benefits compared to the control policy of uniform duty cycle operation (UDCO). These evaluations have been carried out through two simulation-based case studies in which two variants of BSMs were used. In the first variant, the higher resistance cell is located at the end of the string in the downstream of the coolant fluid, and in the second variant it is located in the middle of the string. In both variants, the resistance of the thermally exposed cell was assumed to be almost 50% higher than that of other cells.

The simulation results showed that OP , contrary to UDCO policy, optimally uses the extra DOF of MLC and significantly reduces thermal and SOC imbalance. In a nutshell, the OP achieves thermal balancing by optimally redistributing the power losses among the cells, depending on their resistance and positions in the BSM, by avoiding the use of higher resistance cells during peak power intervals and using them more frequently during low power intervals. Similarly, the SOC balancing is achieved by optimally exploiting the brake regeneration phases. This study also shows that the RF alone cannot achieve temperature uniformity under parameter variations whereas MLC-based OP can achieve this even with UF .

Paper 2

> F. Altaf, L. Johannesson, B. Egardt, "Feasibility Issues of using Three-Phase Multilevel Converter based Cell Balancer in Battery Management System for xEVs," In *IFAC Symposium on Advances in Automotive Control*, pp. 390-397, Sep. 2013, Tokyo.

In chapter 5, the possible drawback of extra heating of a BSM due to dc-link current ripple in 3-ϕ MLC was discussed. Paper 2 thoroughly investigates this issue and evaluates its practical consequences for the battery cells. A detailed harmonic analysis has been done to exactly characterize the nature of this issue and the magnitude of corresponding battery losses. Firstly, in order to characterize the losses and the size of compensating capacitor, the dc-link current is accurately computed using double Fourier series approach. Secondly, the additional battery losses due to the ripple are computed and analyzed. Thirdly, the size of the shunt-capacitor needed for the passive compensation is discussed under nominal operating conditions and lastly, the results are compared to the case of 3-ϕ TLC.

This study establishes that the ripple current on the dc-link inside each power cell (PC$_i$) of 3-ϕ MLC is significant. Consequently, a large dc-link capacitor, which is impractical to install in each PC$_i$, is required to filter the

ripple. In the absence of this capacitor, each cell of the BSM will have to provide significant extra power per unit dc power which would result in much higher additional ohmic losses and accelerated capacity fading compared to the case of 3-ϕ TLC, especially for low power factor operation. The permanent magnet synchronous machine (PMSM), that is commonly used in xEV drives, needs to operate in the field weakening region, where the power factor may become quite small, to meet the demand of high speed driving. Thus, it is concluded that, from battery's health viewpoint, it is unpromising to promote 3-ϕ MLC as an integrated cell balancer and a motor driver in xEVs unless, in addition to the dc-link capacitor, some other active compensation technique is used in order to reduce the size of the capacitor as well as the battery temperature.

Chapter 8

Conclusions

Thermal and SOC balancing is quite important to enhance the life-time of large battery packs in xEVs. SOC balancing can be achieved using various types of dedicated SOC balancers, whereas thermal balancing can be achieved using reciprocating coolant flow as suggested in the literature. However, in this thesis, the use of an MLC as an integrated cell balancer and motor driver has been investigated. The MLC has a special modular structure which enables an independent cell-level control of a battery system. This chapter concludes our investigation of using MLC for the said purpose by pointing out the potentials and pitfalls of this technology.

8.1 Potentials and Pitfalls in DC Applications

An MLC-based optimal control policy (OP) has been formulated, which uses each cell in a battery submodule according to its SOC and temperature to achieve thermal and SOC balancing. The OP is computed by solving a convex optimization problem based on the assumption of dc machine as a load and of perfect information on state of each cell and future driving. Results show that OP, while simultaneously satisfying the driving constraints, reduces temperature and SOC deviations significantly compared with the uniform use of all cells. It is also shown that the MLC-based OP has enough degree-of-freedom to optimally redistribute power losses to achieve good thermal balancing without the need of reciprocating coolant flow. In addition to efficient balancing, the modularity of MLC also makes it possible to completely bypass a faulty cell, saving a vehicle from complete crippling. Thus, MLC has many attractive features which make it a suitable candidate for dc and single-phase ac applications[1]. However, it should be noted

---

[1]Note that MLC for the said purpose can also be advocated for single-phase ac applications because the issue of dc-link ripple in this case is comparable to two-level converters.

that the MLC achieves balancing by redistributing the load current non-uniformly among cells. Thus, it can not achieve balancing when vehicle is at rest. The balancing at standstill is important, especially when vehicle has to be parked for a long period, due to differences in self-discharge current of cells. Moreover, the cell balancing works better at rest because of improvement in SOC estimation. Thus, to achieve balancing at standstill, a dummy load will be needed, which will waste some energy.

8.2 Potentials and Pitfalls in AC Applications

The potential benefits of MLC in dc applications are equally relevant in applications involving three-phase ac machine. However, in this case, 3-ϕ MLC poses a serious issue of extra cell heating due to dc-link current ripple. In addition, each cell has to process extra ampere-hours due to the demand of reactive power from a load. These effects become quite significant, especially at high speed driving when the electric machine needs to draw a lot of reactive power. These effects, if not compensated, may accelerate the battery capacity fading as predicted by the cycle-life model. However, an experimental validation is still needed to ascertain this theoretical assessment. A simple passive compensation method based on dc-link shunt-capacitor has also been investigated, but it turns out that the size of the required capacitor is too big for automotive applications. Thus, it is concluded that, from battery's health viewpoint, it seems unpromising to promote 3-ϕ MLC as an integrated cell balancer and motor driver in xEVs, unless some other more advanced active compensation technique is used.

There are couple of possible solutions to mitigate the said issues. First category of solutions is based on using alternative compensation methods. For example, a dc-dc converter can be used in the dc-link to actively filter the 2nd baseband ripple harmonic. However, this technique will require two additional switches inside every power cell of MLC, which may not be a cost-effective solution. We can also use extra cooling power to compensate the extra battery heating. However, firstly this approach will cost extra fuel and secondly it can not compensate the capacity fading due to extra ampere-hour throughput. Second category of solutions is based on modifying the configuration of the MLC balancer. For example, instead of using 3-ϕ MLC as an integrated cell balancer and driver, single-phase MLC is used only as a dedicated cell balancer in a battery pack, whereas 3-ϕ two-level inverter (TLI) is used as a motor driver. However, this configuration may not be cost effective due to high component count.

Appendices

Appendix A

Additional Analysis Related to Paper 2

In this Appendix, the results from Paper 2 are extended by adding further discussion and analysis to give some more insight to the problem of dc-link ripple in 3-ϕ MLC. A more clear picture of dc-link current spectrum is given in terms of its all harmonic components. In addition, a more thorough discussion on battery ripple as a function of compensation network parameters and power factor angle θ is added. In particular, the impact of ripple on the ageing of MLC battery due to its extra ampere-hour throughput is discussed at length.

A.1 DC-link Current Harmonic Analysis

Consider a three-phase permanent magnet synchronous machine being driven by a 3-ϕ MLC. Assume that the load current in all phases is perfectly sinusoidal with frequency ω_o and the phase angle θ (power factor angle). Thus, the current in phase-a is given by

$$i_a(t) = \sqrt{2}I_a \cos(x_a(t)) \qquad (A.1)$$

where $x_a(t) = \omega_o t + \theta$. Now using the double Fourier series representation of a switching function s_i (obtained by applying eq. (6.4) in Chapter 6 for each phase-leg 1 and 2 inside each PC$_i$), the dc-link current in each PC$_i$ is given by (see Paper 2 for detailed derivation.)

$$i_{dci}(t) = s_i(t)i_a(t) = \frac{M_o I_a}{\sqrt{2}} \cos(\theta) + \frac{M_o I_a}{\sqrt{2}} \cos(2\omega_o t + \theta)$$

$$+ \left[\frac{4}{\pi} \sum_{k=1}^{\infty} \sum_{\substack{l=-\infty \\ l \neq 0 \\ l=odd}}^{\infty} \left[\frac{1}{k} J_l(a_k) \sin(b_{k,l}) \cos(k\omega_c t + l\omega_0 t) \right] \right] \sqrt{2}I_a \cos(x_a) \quad (A.2)$$

where $a_k = (k\frac{\pi}{2}M_o), b_{k,l} = (k+l)\frac{\pi}{2}$, and $w_o = 2\omega_m$ is the electrical angular frequency being fed to a two-pole permanent magnet synchronous machine operating at the angular speed ω_m. Thus, it is obvious from (A.2) that dc-link current in any PC_i of 3-ϕ MLC consists of a dc component, a large 2nd baseband harmonic, and some carrier harmonics. To exactly characterize the nature of carrier harmonics and their side-bands, the last term in the above expression is further expanded to get

$$
\begin{aligned}
i_{dci}(t) = {}& \frac{M_o I_a}{\sqrt{2}} \cos(\theta) + \frac{M_o I_a}{\sqrt{2}} \cos(2\omega_o t + \theta) \\
& + \frac{2\sqrt{2} I_a}{\pi} \Bigg[\sum_{k=1}^{\infty} \frac{1}{k} \bigg\{ J_1\left(a_k\right) \sin\left(b_{k,1}\right) \Big[\cos(k\omega_c t - \theta) + \cos\big((k\omega_c + 2\omega_0)t - \theta\big) \Big] \\
& + J_{-1}\left(a_k\right) \sin\left(b_{k,-1}\right) \Big[\cos(k\omega_c t + \theta) + \cos\big((k\omega_c - 2\omega_0)t - \theta\big) \Big] \bigg\} \\
& + \sum_{k=1}^{\infty} \sum_{\substack{l=-\infty \\ l \neq 0 \\ l \neq \pm 1 \\ l = \text{odd}}}^{\infty} \bigg\{ \frac{1}{k} J_l\left(a_k\right) \sin\left(b_{k,l}\right) \Big[\cos\big((k\omega_c + (l-1)\omega_0)t - \theta\big) \\
& + \cos\big((k\omega_c + (l+1)\omega_0)t + \theta\big) \Big] \bigg\} \Bigg]
\end{aligned}
\tag{A.3}
$$

where $b_{k,1} = (k+1)\frac{\pi}{2}, b_{k,-1} = (k-1)\frac{\pi}{2}$. Since '$l$' is odd thus both '$l-1$' and '$l+1$' are even integers. It means the total carrier side-band harmonic energy is contained only by even carrier side-bands. In order to characterize the carrier harmonics we note that the coefficient

$$
\frac{1}{k} J_l\left(k\frac{\pi}{2}M_o\right) \sin\left([k+l]\frac{\pi}{2}\right) = 0, \ \forall\, (k+l) \in 2\mathbb{Z}
\tag{A.4}
$$

where $\mathbb{Z}$ is the set of all integers. Since 'l' is odd thus '$k+l$' is even for all odd k's, thus

$$
\frac{1}{k} J_l\left(k\frac{\pi}{2}M_o\right) \sin\left([k+l]\frac{\pi}{2}\right) = 0, \ \forall k \in 2\mathbb{Z}+1
\tag{A.5}
$$

Thus, all odd carrier harmonics and their sidebands are zero. Now, it is obvious from equations (A.3) and (A.5) that the dc-link current in any PC_i of 3-ϕ MLC consists of a dc component, large 2nd baseband harmonic, all even carrier harmonics along with their even sidebands. Figure A.1 shows the spectrum of kth carrier harmonic and its sidebands centered around $k\omega_c$.

Remark A.1. *We did not discuss the dc-link ripple for single-phase MLC because in case of single-phase applications the dc-link ripple at 2nd baseband*
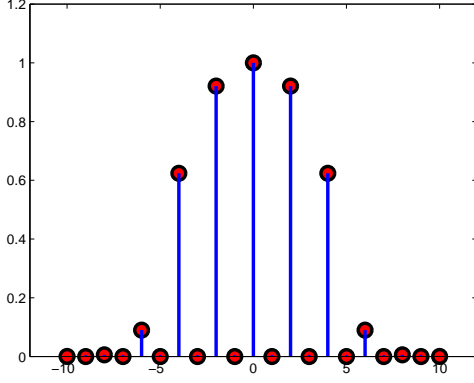
Figure A.1: The kth carrier harmonic and its side-bands.
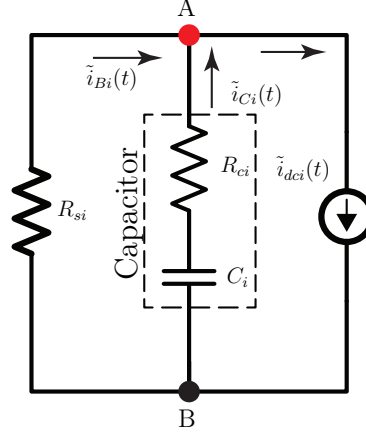
Figure A.2: DC-Link ac equivalent circuit.

frequency exists for both single-phase MLC and single-phase TLC. Thus, both topologies are comparable in terms of low frequency harmonic content in single-phase applications. However, the difference in 3-ϕ applications becomes significant due to presence of additional 2nd baseband harmonic in 3-ϕ MLC contrary to 3-ϕ TLC.

A.2 DC-link Ripple Passive Compensation

Since the carrier harmonics and their side-bands commonly lie at very high frequencies, they can be easily filtered using a small size capacitor. Hence, the higher harmonics are neglected in the following analysis. The dc-link current is now given by

$$i_{dci}(t) \approx \bar{I}_{dci}(\theta) + \tilde{i}_{dci}(t) = \frac{M_o I_a}{\sqrt{2}} \cos(\theta) + \frac{M_o I_a}{\sqrt{2}} \cos(2\omega_o t + \theta) \qquad \text{(A.6)}$$

where $\bar{I}_{dci}$ is a pure dc-component and $\tilde{i}_{dci}(t)$ is a pure ac-component with rms value $\tilde{I}_{dcir}$. Note that the amplitude of this ac-component is equal to that of dc-component at $\theta = 0$. The total dc-link current $i_{dci}(t, \theta)$ is plotted in Figure A.3 along with its dc-component (average value) $\bar{I}_{dci}(\theta)$, and its rms value $I_{dcir}(\theta) = \sqrt{\bar{I}_{dci}^2 + \tilde{I}_{dcir}^2}$ for various values of power factor angle θ. The average and rms values of $i_{dci}(t, \theta)$ vary at different rates as a function of θ, as shown in the figure, resulting in increase in their difference as θ increases. If the ripple is not compensated then it will cause the flow of bidirectional current in the battery for all positive θ (note micro-charing/discharging cycles in the figure) and its magnitude will increase with
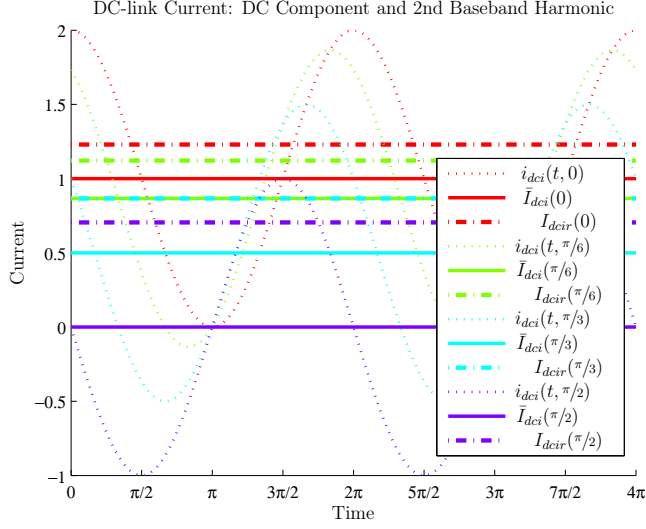
Figure A.3: *Battery ripple without compensator.* The total dc-link current $i_{dci}(t, \theta)$, its dc component $\bar{I}_{dci}(\theta)$, and its rms value $I_{dcir}(\theta)$ are shown as a function of power factor angle θ. Note the micro-charigng/discharging cycles and the difference in dc and rms values.

increase of θ. The average value of current does the actual work (or transfer the useful unidirectional power) whereas the rms value incurs the ohmic losses. Thus, the dc-link ripple current causes the MLC battery to generate *extra heat* and to process *extra Ah-throughput* (due to bidirectional current flow) relative to the amount of useful work. Therefore, the dc-link ripple must be compensated. In this study, we assume a passive compensation network which consists of a dc-link shunt-capacitor.

A.2.1 Model of DC-link Compensation Network

In the next section, the impact of ripple on each Cell$_i$ as a function of compensation *network parameters* and the *power factor angle* θ will be analyzed and for this a model of compensation network is needed. Let us consider an *ac equivalent circuit* of the dc-link compensation network as shown in Figure A.2. The state-space model of this compensation network is given by

$$\dot{\tilde{v}}_{ci}(t) = -\frac{1}{C_i(R_{ci} + R_{si})}\tilde{v}_{ci}(t) + \frac{R_{si}}{C_i(R_{ci} + R_{si})}\tilde{i}_{dci}(t) \qquad (A.7)$$

$$\tilde{i}_{Bi}(t) = \frac{1}{R_{ci} + R_{si}}\tilde{v}_{ci}(t) + \frac{R_{ci}}{R_{ci} + R_{si}}\tilde{i}_{dci}(t) \qquad (A.8)$$

where $\tilde{v}_{ci}(t)$ is capacitor voltage, $\tilde{i}_{Bi}(t)$ is battery ripple current, R_{si} is the series resistance of Cell$_i$, C_i is the capacitance of dc-link capacitor and R_{ci} is its effective series resistance (ESR). The transfer function model is given below

$$T_{dci}(s) = \frac{\tilde{I}_{Bi}(s)}{\tilde{I}_{dci}(s)} = \frac{1 + R_{ci}C_i\,s}{1 + C_i(R_{ci} + R_{si})\,s} \qquad (A.9)$$

The compensation network acts as a low-pass filter with two corner frequencies corresponding to pole and zero locations given by

$$p_{fi} = -\frac{1}{C_i(R_{ci} + R_{si})} \qquad (A.10)$$

$$z_{fi} = -\frac{1}{C_i R_{ci}} \qquad (A.11)$$

The amplitude and phase of the compensation network filter are, respectively, given by

$$|T_{dci}(\omega)| = \sqrt{\left(\frac{1 + \omega^2 R_{ci}^2 C_i^2}{1 + \omega^2 (R_{ci} + R_{si})^2 C_i^2}\right)}, \qquad (A.12)$$

$$\phi_{dci}(\omega) = \angle T_{dci}(\omega) = \arctan\left(\frac{-C_i R_{si}\omega}{1 + C_i^2 R_{ci}(R_{ci} + R_{si})\omega^2}\right) \qquad (A.13)$$

and the high frequency gain of this filter is given by

$$G_{hf} = \lim_{\omega \to \infty} |T_{dci}(\omega)| = \frac{1}{1 + \frac{R_{si}}{R_{ci}}} \qquad (A.14)$$

The filter has two corner frequencies. Note that modeling R_{ci} is necessary as it adds a zero and thus contributes in shaping the composite roll-off curve of the filter for a given C_i. In order to reduce the ripple at $\omega = 2\omega_o$ in the battery, the filter should have very low high-frequency gain with bandwidth well below $2\omega_o$. To ensure $G_{hf} \ll 1$, the zero should be placed far away from the pole in the left-half-plane which requires $R_{ci} \ll R_{si}$. In addition, the pole must be placed such that the first corner frequency is well below $2\omega_o$. Thus, the condition to get desired behavior from the filter is

$$|p_{fi}| \ll 2\omega_o \ll |z_{fi}|$$

Remark A.2. *It is pertinent to discuss the behavior of filter against various dc-link network parameters. It should be noted that keeping other parameters fixed and varying C_i affects both pole and zero locations. Also note that increasing R_{ci} may violate the above condition and consequently change the shape (or slope) of filter roll-off curve around $2\omega_o$. Therefore choosing a dc-link capacitor with just high C_i, without giving any consideration to its ESR,*

is not sufficient for desired compensation. Similarly, note that filter gain is higher for lower R_{si} and vice versa. In addition, decreasing R_{si} increases the filter corner frequency and may consequently affect the shape of filter roll-off curve. Thus, the selection of a capacitor with right combination of C_i and R_{ci} while keeping in consideration the value of R_{si} is a key to achieve better results with passive compensation method. The lower ESR capacitor will in general give better compensation.

A.3 Impact of Ripple under Compensation

In this section, the impact of battery ripple is analyzed as a function of passive compensation network parameters and the power factor angle θ. Firstly, the ripple power processed by each Cell$_i$ is determined. Secondly, the additional battery losses due to ripple are analyzed for two extreme cases: losses with no compensation capacitor and losses with infinite compensation capacitor. Finally, the extra Ah-throughput that each Cell$_i$ has to process is calculated.

A.3.1 Ripple Power Processed by Cell$_i$

The pure ac ripple current dynamic response in each Cell$_i$ is defined by

$$\tilde{I}_{Bi}(s) = T_{dci}(s)\tilde{I}_{dci}(s) \tag{A.15}$$

with steady-state response given by

$$\tilde{i}_{Bi}(t) = \tilde{I}_{Bim}(\omega)\cos(2\omega_o t + \bar{\theta}) \tag{A.16}$$

where $\tilde{I}_{Bim}(\omega) = \frac{|T_{dci}|M_o I_a}{\sqrt{2}}$ is the peak magnitude of battery ripple current and $\bar{\theta} = \theta + \phi_{dci}(\omega)$ where $\phi_{dci}(\omega)$ is the phase-shift given by the dc-link network. Thus, the total battery current at steady-state is given by

$$i_{Bi}(t) = \bar{I}_{Bi} + \tilde{i}_{Bi}(t) \tag{A.17}$$

with rms value $I_{Bir} = \sqrt{\bar{I}_{Bi}^2 + \tilde{I}_{Bir}^2}$ where $\bar{I}_{Bi} = \bar{I}_{dci}(\theta) = \frac{M_o I_a}{\sqrt{2}}\cos(\theta)$ is the battery dc current and $\tilde{I}_{Bir} = \frac{\tilde{I}_{Bim}(\omega)}{\sqrt{2}} = \frac{|T_{dci}|M_o I_a}{2}$ is rms value of $\tilde{i}_{Bi}(t)$. Similarly, the total battery terminal voltage at steady-state is given by

$$v_{Bi}(t) = \bar{V}_{Bi} + \tilde{v}_{Bi}(t) \tag{A.18}$$

where $\bar{V}_{Bi}$ is the dc component (known battery nominal voltage) and $\tilde{v}_{Bi}(t)$ is a pure ac ripple voltage superimposed on $\bar{V}_{Bi}$ and is given by

$$\tilde{v}_{Bi}(t) = \tilde{i}_{Bi}(t)R_{si} = \tilde{V}_{Bim}(\omega)\cos(2\omega_o t + \bar{\theta}) \tag{A.19}$$

where $\tilde{V}_{Bim}(\omega) = \tilde{I}_{Bim}(\omega)R_{si} = \frac{|T_{dci}|M_o I_a R_{si}}{\sqrt{2}}$ is the peak magnitude of ripple voltage. Now, using equations (A.17) and (A.18), the total power processed (delivered or absorbed) by Cell$_i$ at steady-state is given by

$$p_{Bi}(t) = v_{Bi}(t)i_{Bi}(t) = \bar{P}_{Bi} + \tilde{p}_{Bi}(t) \tag{A.20}$$

where

$$\bar{P}_{Bi} = \bar{P}_{Bi1} + \bar{P}_{Bi2} = \bar{V}_{Bi}\bar{I}_{Bi} + \tilde{P}_{Bi1m} \tag{A.21}$$

$$\tilde{p}_{Bi}(t) = \tilde{p}_{Bi1}(t) + \tilde{p}_{Bi2}(t), \text{ where} \tag{A.22}$$

$$\tilde{p}_{Bi1}(t) = \tilde{P}_{Bi1m}\cos(4\omega_o t + 2\bar{\theta}) \tag{A.23}$$

$$\tilde{p}_{Bi2}(t) = \tilde{P}_{Bi2m}\cos(2\omega_o t + \bar{\theta}) \tag{A.24}$$

are constant dc power and bi-directional fluctuating (ripple) power respectively. The power $\tilde{p}_{Bi}(t) \in [-\tilde{P}_{Bim}^-, +\tilde{P}_{Bim}^+]$ is a *non-sinusoidal* fluctuation around zero mean with $\tilde{P}_{Bim}^+(t) = \tilde{P}_{Bi1m} + \tilde{P}_{Bi2m}$ as a positive peak magnitude and $\tilde{P}_{Bim}^-(t) = \tilde{P}_{Bi2m} - \tilde{P}_{Bi1m}$ as a negative peak magnitude where $\tilde{P}_{Bi1m} = \frac{\tilde{V}_{Bim}(\omega)\tilde{I}_{Bim}(\omega)}{2}$ and $\tilde{P}_{Bi2m} = \tilde{I}_{Bim}(\omega)\left(\bar{V}_{Bi} + \bar{I}_{Bi}R_{si}\right)$ are peak magnitudes of $\tilde{p}_{Bi1}(t)$ and $\tilde{p}_{Bi2}(t)$ respectively.

A.3.2 Extra Losses in Cell$_i$

The pure ripple power loss in Cell$_i$ is caused by the rms value $\tilde{I}_{Bir}$ of $\tilde{i}_{Bi}(t)$ and the dc power loss is caused by dc current $\bar{I}_{Bi}(\theta)$. Note that under ideal conditions, the battery in an ideal inverter (like an ideal 3-ϕ TLC) would provide only the dc current and capacitor would deliver/absorb almost the whole ripple power. Thus, in order to compare battery ripple performance in 3-ϕ MLC to an ideal situation, we define the ripple power loss per unit dc (or real) power loss, as a function of network parameters and θ, as a figure of merit as follows (see Section 6 in Paper 2 for derivation)

$$\delta P_{lBqi} = \frac{P_{lBqi}}{P_{lBai}} = \left(\frac{1 + \omega^2 R_{ci}^2 C_i^2}{1 + \omega^2(R_{ci} + R_{si})^2 C_i^2}\right)\frac{1}{2\cos^2(\theta)} \tag{A.25}$$

where R_{si} is the series resistance of Cell$_i$, C_i is the capacitance of dc-link capacitor and R_{ci} is its effective series resistance (ESR). Now we compute the value of δP_{lBqi} under two extreme limits:

No DC-link Capacitor

When there is no capacitor we have

$$\delta P_{lBqi}^{uc} = \lim_{C_i \to 0} \delta P_{lBqi} = \frac{1}{2\cos^2(\theta)} = \frac{1}{2F_p^2}$$

where $F_p = \cos(\theta)$ is the power factor. Therefore, when $F_p = 1$ then $\delta P_{lBqi}^{uc} = 0.5$ and when

$$F_p \to 0 \Rightarrow \delta P_{lBqi}^{uc} \to \infty$$

Thus, in the absence of dc-link capacitor, each Cell$_i$ will suffer from minimum 50% additional losses, due to ripple power flow, compared to a case when the cell had to deliver only real power.

Infinite DC-link Capacitor

When we have infinite capacitance then we have

$$\lim_{C_i \to \infty} \delta P_{lBqi} = \left(\frac{R_{ci}^2}{(R_{ci} + R_{si})^2} \right) \frac{1}{2F_p^2}$$

which means even for the case of unity power factor and infinite capacitance, δP_{lBqi} is governed by relative values of R_{ci} and R_{si}. If we have $R_{ci} \ll R_{si}$ then $\delta P_{lBqi} \to 0$. Thus, a big, low ESR capacitor is needed to reduce the losses due to 2nd baseband ripple harmonic. These requirements for dc-link capacitor may not be easily realizable for vehicle applications. Thus, the rise in battery temperature due to extra losses is inevitable. Since the cyclic ageing is accelerated at elevated temperature (see table 2.2 on page 16 and section 2.5.2), the cycle-life of modular battery inside MLC will be compromised.

Remark A.3. *Since it is required to choose a dc-link capacitor with $R_{ci} \ll R_{si}$, it may become quite challenging to meet the requirement of low ESR capacitor for a battery with very low R_{si}.*

A.3.3 Extra Charge Processing in Cell$_i$

According to cycle-life model (2.8) (see section 2.5.3 on page 18), the capacity of a battery fades as a function of its Ah-throughput A_h. In this section we analyze the extra charge that each Cell$_i$ has to process, due to dc-link current ripple, as a function of network parameters and θ. The average value $\bar{P}_{Bi}$ of (*unidirectional*) battery power $p_{Bi}(t)$, called real or dc power, does the real work. The Cell$_i$ has to unnecessarily process extra charge as soon as the power $p_{Bi}(t)$, defined in (A.20), becomes *bidirectional*. It can be easily verified from equation (A.20) that $p_{Bi}(t)$ will be unidirectional if and only if the negative magnitude of $\tilde{p}_{Bi}(t)$ is not bigger than the dc power $\bar{P}_{Bi}$ i.e.

$$\frac{\tilde{P}_{Bim}^-}{\bar{P}_{Bi}} \leq 1 \tag{A.26}$$

Now, in order to calculate the amount of extra charge that a cell inside each PC_i has to process during bidirectional power flow, we need to calculate the times of zero crossings of $i_{Bi}(t)$ as follows

$$\bar{I}_{Bi} + \tilde{I}_{Bim}(\omega)\cos(2\omega_o t + \bar{\theta}) = 0$$

$$\Rightarrow \bar{I}_{Bi}\left(1 + \left(\frac{|T_{dci}(\omega)|}{\cos(\theta)}\right)\cos(2\omega_o t + \bar{\theta})\right) = 0 \qquad (A.27)$$

Note that the last equation gives correct zero-crossing time only for $\frac{\cos(\theta)}{|T_{dci}|} \in [0,1]$. Now, using last equation, the first zero-crossing time (in seconds) during a first cycle of battery ripple current is given by

$$t_1 = \frac{1}{2\omega_o}\left[\pi - \arccos\left(\frac{\cos(\theta)}{|T_{dci}|}\right) - \bar{\theta}\right] \qquad (A.28)$$

and the second zero-crossing is given by

$$t_2 = \frac{\pi}{2\omega_o} \qquad (A.29)$$

Now we can calculate the extra charge (in ampere-hours) that the battery has to process during each cycle (of period $T = \pi/\omega_0$) of ripple current

$$\tilde{A}_{h,i,T} = \frac{1}{3600}\int_{t_1}^{t_2}|i_{Bi}(t)|\mathrm{d}t \qquad (A.30)$$

Now let us consider 3-ϕ MLC driving an electric machine in xEV at constant power factor $F_p = \cos(\theta)$ over a whole drive cycle of length ΔT_D (in hours). Suppose, each Cell$_i$ of MLC is processing N_{cr} number of ripple cycles during full drive cycle then the *total extra charge* processed by Cell$_i$ during $\Delta T_D = \frac{N_{cr}T}{3600}$ is given by

$$\tilde{A}_{h,i} = N_{cr}\tilde{A}_{h,i,T} \qquad (A.31)$$

Similarly, the *total dc charge* processed by Cell$_i$ during ΔT_D is given by

$$\bar{A}_{h,i} = \bar{I}_{Bi}\Delta T_D \qquad (A.32)$$

Now, we define another figure of merit given by

$$\delta A_{h,i} = \frac{\tilde{A}_{h,i}}{\bar{A}_{h,i}} \qquad (A.33)$$

which we will use to analyze an extra cyclic capacity fading of battery in 3-ϕ MLC, compared with that of battery in an ideal 3-ϕ inverter, due to extra ripple charge throughput of each Cell$_i$ of MLC for a given power factor and fixed compensation network.

Case 1: Cell$_i$ Capacity Fading vs θ for Fixed C_i

The $\delta A_{h,i}$ is computed, under the assumption of the fixed compensation network with $C_i = 10\,mF$ and $R_{ci} = 1\,m\Omega$, as a function of power factor angle θ in the range $[0, 70°]$. The result is plotted in Fig. A.4(a). The figure shows that $\delta A_{h,i}$ is almost linear in θ for $\theta \in [0, 20°]$ (where the power factor $F_p \in [0.94, 1]$). However, for $\theta > 20°$ the $\delta A_{h,i}$ follows a trend of a quadratic polynomial in θ and, especially for $\theta > 50°$, the additional Ah-throughput of the Cell$_i$ of MLC becomes significant compared to the case of battery in an ideal inverter which has to process only the dc ampere-hours. Note that $\delta A_{h,i} \approx 0.22$ at $\theta = 60°$ (where $F_p = \cos(\theta) = 0.5$). Thus, the cycle-life model given by eq. (2.8) suggests that each Cell$_i$ of MLC will lose higher energy capacity compared to the case of battery connected to ideal 3-ϕ TLC.

Case 2: Cell$_i$ Capacity Fading vs C_i for Fixed θ

In this case, $\delta A_{h,i}$ is computed as a function of C_i for fixed $\theta = 60°$ ($F_p = 0.5$) and $R_{ci} = 1\,m\Omega$. The result is shown in Fig. A.4(b). The figure shows that even a capacitor as big as $100\,mF$ is not sufficient to bring any significant reduction in $\delta A_{h,i}$. Thus, it may be practically infeasible to compensate the additional ampere-hours processed by Cell$_i$ in MLC using passive compensation.

Remark A.4. *Although the cycle-life model (2.8) predicts the additional capacity fading of MLC battery, but to ascertain its actual capacity loss requires further careful experimental investigation based on post-mortem analysis of a cell micro-cycled under such conditions.*

Remark A.5. *In the above analysis, we assumed that the power factor angle θ may vary in the range $[0, 70°]$. It is motivated by the fact that permanent magnet synchronous machine (PMSM), that is commonly used in xEV drives, needs to operate in the field weakening region to meet the demand of high speed driving cycles. However, for operating points in this region, the PMSM needs to draw a lot of reactive power and the power factor $F_p = \cos(\theta)$ may easily fall below 0.5 [72]. Thus, during high speed driving, assuming the maximum value of θ around 70° is not unrealistic.*
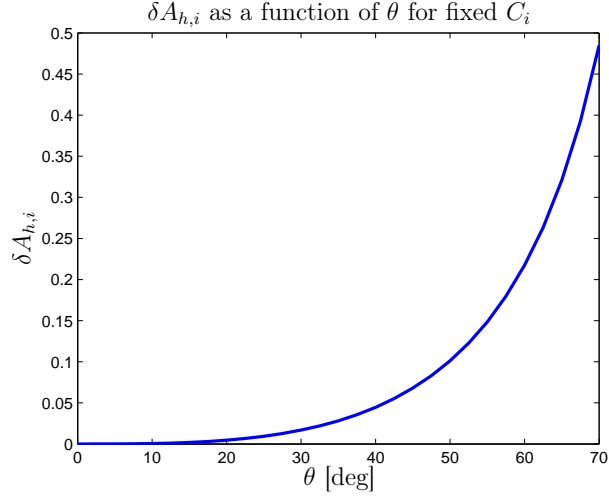
(a) Ripple ampere-hours per dc-ampere hours processed by Cell$_i$ as a function of power factor angle θ. We assumed a fixed compensation network with $C_i = 10\,mF$ and $R_{ci} = 1\,m\Omega$.
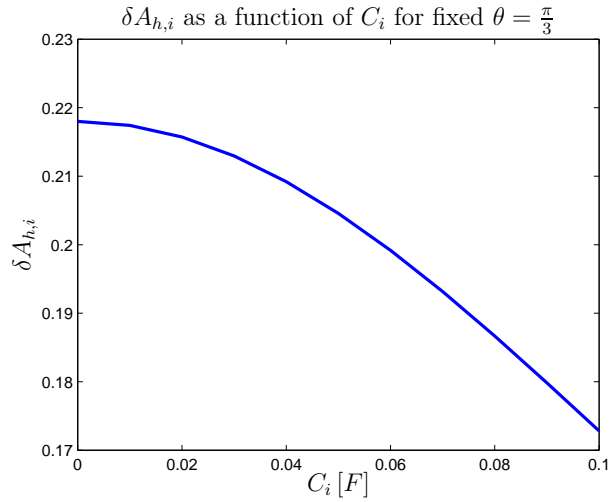
(b) Passive compensation of additional Ah-throughput. The figure shows the ripple ampere-hours per dc-ampere hours processed by Cell$_i$ as a function of C_i for fixed $\theta = \frac{\pi}{3}$ and $R_{ci} = 1\,m\Omega$.

Figure A.4: Extra ampere-hours processed by each Cell$_i$ of 3-ϕ MLC

Appendix B

Battery Glossary

This appendix reviews the basic battery terminology, see [27] for details. In section B.1 various classes of batteries are reviewed, main components of any battery and the battery terminology are discussed in section B.2 and B.3 respectively.

B.1 Classification of Batteries

The batteries can be classified in many ways. In the following, two types of classifications are given.

B.1.1 Classification 1

This classification of cells is based on their power to energy ratio.

Power Cells or Energy Cells

There is always a trade-off between power and energy of cells. The batteries can be either high-power or high-energy but not both. This limitation comes from electrode material. A high-power cell needs a large number of thinner electrodes and thicker current collector to ensure efficient electronic conduction whereas high-energy cell needs a small number of thicker electrodes and thinner current collectors to achieve higher amount of active material. The small number of thicker electrodes increase the over-all surface area of electrodes which facilitates the large number of atoms of active materials to take part in chemical redox reaction. The cell manufacturer normally categorize their cells according to this classification.

B.1.2 Classification 2

In this classification cells are classified according to their re-chargeability.

Primary Cells

Primary cells are not capable of being charged electrically. Energy is stored inside them once during cell manufacturing and they are discarded when they are fully drained. These cells normally have a quite high energy density and shelf-life.

Secondary Cells

Secondary cells (also known as rechargeable cells) are capable of being charged after they are fully drained. Secondary batteries are used for storage of electrical energy and are thus also known as "storage batteries" or "accumulators". The one of the most desired characteristic of secondary batteries is the long cycle-life. In order to achieve long cycle-life, the charge and discharge of battery should be highly efficient with minimum irreversible capacity loss during transformation of chemical energy to electrical energy and vice versa. In addition, secondary cells should also have other desired characteristics like high energy and power density, high discharge rates, low impedance, low leakage current (i.e. long shelf-life), and good performance over wide temperature range. Due to all these stringent requirements there are only few materials which can be employed in secondary cells. The most common types of secondary cells include lead-acid (PbA), nickel-cadmium (NiCd), nickel-metal hydride (NiMH) and the lithium-ion (LIB). The rechargeable batteries normally have higher power density compared to primary batteries and are thus capable of handling relatively very high discharge rates. However, the energy density and shelf-life of most secondary cells are lower than those of primary cells except rechargeable LIBs which have very high energy density, shelf-life as well as very long cycle-life.

B.2 Main Components of a Battery

A cell consists of various parts which are briefly reviewed below [27].

Anode and Cathode

Strictly speaking, in *electrochemical convention*, the anode is an electrode in a cell where oxidation takes place i.e. where atom *loses* electron and *increases* its oxidation number. Thus during discharge, the negative electrode is the anode whereas during charge the positive electrode is the anode.

Similarly, the cathode is an electrode in a cell where reduction takes place i.e. where atom *gains* electron and *reduces* its oxidation number. Thus during discharge, the positive electrode is the cathode whereas during charge the negative electrode is the cathode.

This strict naming convention may create confusion, therefore in most of the battery literature the *battery convention* is followed where the names of electrodes are fixed according to discharge process. Thus, the negative electrode is commonly called anode and positive electrode is normally called cathode.

Electrolyte

The medium inside the cell which provides the mechanism for transport of ions between anode and cathode of a cell.

Electrolyte Additives

The side reactions between electrolyte and electrodes result in capacity loss. The presence of impurity such as water inside electrolyte can also lead to capacity loss. Moreover, electrolytes may be highly flammable, like for example in LIB, and pose a great safety hazard. These problems can be mitigated by using very high-purity electrolytes as well as by using some organic or inorganic additives inside electrolytes.

Current Collectors

A part of the electrode which does not take part in chemical reaction but is a very good electronic conductor. It is used to conduct electronic current from the anode to cathode through the external circuit during discharge and the reverse during charge.

Separator

The separator is a material which is placed inside the cell as a spacer between anode and cathode to prevent the internal short-circuit between them. The separator is electronically non-conductive but it has very high permeability for ions.

B.3   Battery Terminology and Metrics

In this section, definitions of some battery related terms will be given.

B.3.1 Cell, Sub-Modules, Modules and Packs

A cell is the most basic and smallest packaged form of a battery. The voltage output from a cell normally ranges from 1.35V (NiCd) to 4V (LIB). A battery sub-module (BSM) is collection of two or more cells connected in series and a battery module (BM) is a collection of two or more BSMs connected in series or parallel to get higher energy or power or both. A battery pack (BP) is a collection of several BMs connected in series and parallel to meet voltage, energy and power requirements.

B.3.2 Battery Basic Metrics

Cell Capacity

The total amount of charge, stored inside the active mass of electrodes, that can be delivered by a cell under certain operating conditions. There are various definitions of cell capacity. These definitions differ based on the operating conditions (i.e. end-of-discharge-voltage (EODV), end-of-charge-voltage (EOCV), rate of discharge, ambient temperature etc.) of a cell.

- The theoretical capacity C_t is the maximum number of ampere-hours (charge) that can be *theoretically extracted* from a cell *based only on the amount of active material* it contains. In this rating, we do not consider the conditions under which battery is operating.

- The rated capacity C_r is the maximum number of ampere-hours that a fully charged *fresh* cell can deliver *under standard operating conditions specified by a manufacturer* (i.e. EODV, rate of discharge, ambient temperature).

- The practical (or actual) capacity C_p is the maximum number of ampere-hours (charge) that can be *actually delivered* by a *fully* charged cell while discharging *under non-standard discharge conditions* to the *standard EODV*.

- The dischargeable (or available or releasable) cell capacity C_d is the portion of practical capacity that can be obtained from a cell at the user defined discharge rates and other specified operating conditions like initial SOC level and EODV.

- The chargeable capacity C_c of a cell is the used cell capacity that can be charged. The chargeable cell capacity is also called absorbable or used cell capacity.

Cell Energy

Cell energy is obtained by multiplying cell output voltage with its capacity. As we have various metrics for cell capacity thus we have various metrics for cell energy as well like theoretical energy, rated energy, practical energy, and available energy.

Battery Pack Capacity

The pack capacity is the maximum number of available ampere-hours that can be released from a fully charged state of a $Cell_x$ in the battery pack to a fully discharged state of the same or some other $Cell_y$ in the battery pack under specified operating conditions. In other words, the pack capacity can also be defined as the sum of dischargeable and chargeable pack capacities which are defined below.

- The maximum dischargeable (or available) capacity of a BP is given by a cell in a pack with the minimum remaining cell capacity that can be discharged.

- The maximum chargeable (or Used) capacity of a BP is given by a cell in a pack with the minimum used cell capacity that can be charged.

Remark B.1. *If the battery pack is assumed to be in the fully charged state then the pack total capacity is simply given by that cell which has the minimum dischargeable capacity in the whole fully charged pack.*

Cell State-of-Charge

The cell SOC at any time 't' refers to the dischargeable cell capacity as a percentage of some reference. Most commonly, the total actual capacity of a cell is used as a reference.

$$SOC(t) = \frac{C_d(t)}{C_p(t)} \tag{B.1}$$

The SOC describes how the battery at time 't' is different, in terms of its currently available energy content, from that of its fully charged state. The SOC of a fully charged cell, whether fresh or aged, is always equal to 1.

Cell Depth-of-Discharge

The depth-of-discharge (DOD) of a cell at a given time is a ratio between the quantity of charge (ampere-hour) removed from a cell up to that time instant and the actual capacity (in some literatures rated capacity is used as

well) of a cell. It is expressed as a percentage (0% = full, 100% = empty). A cell will be considered under a deep discharge when it is discharged to at least 80% DOD.

Theoretical Cell Voltage

Theoretical cell voltage is the voltage output from a cell under equilibrium conditions i.e. when no current is being drawn or delivered from a cell. It is also called open-circuit or equilibrium voltage and is denoted by V_{oc}.

Cell Polarizations and Losses

The cell polarization is the deviation of cell output voltage from its theoretical voltage. The measure of the magnitude of the polarization is called over-potential. In a cell, ideally all the electrochemical energy should get converted to electrical energy. However, some losses occur due to polarization effects when the external load current passes through the electrodes and the electrochemical reactions (called electrode reactions) take place at electrodes. The electrode processes consist of the electrode reaction and the mass transport process (or charge transport). The electrode reaction is a solid/electrolyte interfacial reaction that involves various process but the main step is the charge transfer reaction. The polarization effects appear in a cell due to kinetic limitations of these steps in electrode reaction. These polarization effects inside a cell consumes some part of the chemical energy stored inside electrodes and dissipate it as heat. Thus, all the theoretical energy, which is calculated based on active materials in electrodes, of a cell is not converted into electrical energy and therefore the cell performance is degraded. Thus, the voltage output from a cell under operation is given by

$$V_B = V_{oc} - V_{op} - V_{cp} - V_{ap} \qquad \text{(B.2)}$$

where V_{oc} is open-circuit voltage, V_{op} is ohmic polarization (or over-potential), V_{cp} is the concentration polarization, and V_{ap} is the activation polarization of the cell which are respectively defined as follows.

- The voltage drop inside a cell due to internal ohmic resistance is called ohmic polarization. This voltage drop is proportional to load current and thus follows the ohm's law.

- The activation polarization appears due to limitation of charge-transfer reaction kinetics. The activation polarization is dynamic in nature and thus it does not develop or collapse instantly. In equivalent circuit cell models, this behavior is modeled using a parallel RC branch.

- The concentration polarization is the potential difference across the diffusion layer on the electrode/electrolyte interface (interfacial region). It develops due to concentration gradient across the diffusion layer. It develops due to limitation of charge-transport kinetics. The concentration polarization is also dynamic in nature however it has slower dynamics compared to activation polarization because the charge-transport happens through the diffusion process which is a slower process than charge transfer reaction. In equivalent circuit approach, this behavior is also modeled using a parallel RC branch.

Battery Cycle

The full battery cycle is the discharge of a fully charged battery followed or preceded by the charging process such that the battery is restored to its original initial condition. The cycle is called deep-discharged cycle if at least 80% of the battery energy is consumed otherwise it is called shallow (or micro or flat) cycle.

C-Rate

The c-rate of a charing or discharging current is the ratio of the battery current to the rated capacity of a cell

$$c = \frac{I_B}{C_r} \tag{B.3}$$

A cell discharging at 1 c-rate will be completely discharged in one hour.

Total Ah Throughput

The total amount of charge processed (delivered or absorbed) by a cell before its EOL.

B.3.3 Battery Life-time and Ageing Terms

Cell ages when they are used. There are various metrics and terms which are used in this context, some of them are defined below.

Calendar Life

Calendar ageing is the proportion of irreversible capacity loss that occurs with time especially during storage. The expected lifespan (in time) of a cell under storage (or periodic cycling) conditions is called calendar-life.

Cycle Life

Cycle life is the number of charge/discharge cycles that a cell can undergo, under specified conditions, before its end-of-life (EOL). Various performance limits can be used to mark EOL. For example, when the practical cell capacity falls below minimum desired level of 80% of rated capacity.

State-of-Health

State-of-health (SOH) is a unitless quantity used to measure the current condition of a cell *relative to a fresh cell*. There are various cell parameters which vary with cell age and thus can be used to indicate the SOH of a cell. However, the SOH based on capacity loss is normally used as given below

$$SOH = \frac{\text{Maximum capacity of an aged cell}}{\text{Maximum capacity of a fresh cell}} = \frac{C_p}{C_r} \qquad \text{(B.4)}$$

The SOH describes how a battery at time 't' is different, in terms of its fully charged energy content, from that of a fresh cell.

References

[1] C. D. Rahn and C.-Y. Wang, *Battery systems engineering.* John Wiley & Sons, 2012.

[2] J. Gallardo-Lozano, E. Romero-Cadaval, M. I. Milanes-Montero, and M. A. Guerrero-Martinez, "Battery equalization active methods," *Journal of Power Sources*, vol. 246, pp. 934–949, 2014.

[3] R. Mahamud and C. Park, "Reciprocating air flow for li-ion battery thermal management to improve temperature uniformity," *Journal of Power Sources*, vol. 196, no. 13, pp. 5685 – 5696, 2011.

[4] T. M. Bandhauer, S. Garimella, and T. F. Fuller, "A critical review of thermal issues in lithium-ion batteries," *Journal of the Electrochemical Society*, vol. 158, no. 3, pp. R1–R25, 2011.

[5] B. Wu, V. Yufit, M. Marinescu, G. J. Offer, R. F. Martinez-Botas, and N. P. Brandon, "Coupled thermal-electrochemical modelling of uneven heat generation in lithium-ion battery packs," *Journal of Power Sources*, 2013.

[6] Y. Troxler, B. Wu, M. Marinescu, V. Yufit, Y. Patel, A. J. Marquis, N. P. Brandon, and G. J. Offer, "The effect of thermal gradients on the performance of lithium-ion batteries," *Journal of Power Sources*, vol. 247, pp. 1018–1025, 2014.

[7] A. Barré, B. Deguilhem, S. Grolleau, M. Gérard, F. Suard, and D. Riu, "A review on lithium-ion battery ageing mechanisms and estimations for automotive applications," *Journal of Power Sources*, vol. 241, no. 0, pp. 680 – 689, 2013.

[8] M. Broussely, P. Biensan, F. Bonhomme, P. Blanchard, S. Herreyre, K. Nechev, and R. Staniewicz, "Main aging mechanisms in li ion batteries," *Journal of Power Sources*, vol. 146, no. 1, pp. 90–96, 2005.

REFERENCES

[9] J. Vetter, P. Novak, M. Wagner, C. Veit, K.-C. Möller, J. Besenhard, M. Winter, M. Wohlfahrt-Mehrens, C. Vogler, and A. Hammouche, "Ageing mechanisms in lithium-ion batteries," *Journal of power sources*, vol. 147, no. 1, pp. 269–281, 2005.

[10] P. Ramadass, B. Haran, P. M. Gomadam, R. White, and B. N. Popov, "Development of first principles capacity fade model for li-ion cells," *Journal of The Electrochemical Society*, vol. 151, no. 2, pp. A196–A203, 2004.

[11] P. Ramadass, B. Haran, R. White, and B. N. Popov, "Mathematical modeling of the capacity fade of li-ion cells," *Journal of Power Sources*, vol. 123, no. 2, pp. 230–240, 2003.

[12] J. Wang, P. Liu, J. Hicks-Garner, E. Sherman, S. Soukiazian, M. Verbrugge, H. Tataria, J. Musser, and P. Finamore, "Cycle-life model for graphite-LiFePO$_4$ cells," *Journal of Power Sources*, vol. 196, no. 8, pp. 3942–3948, 2011.

[13] S. Paul, C. Diegelmann, H. Kabza, and W. Tillmetz, "Analysis of ageing inhomogeneities in lithium-ion battery systems," *Journal of Power Sources*, 2013.

[14] W. C. Lee, D. Drury, and P. Mellor, "Comparison of passive cell balancing and active cell balancing for automotive batteries," in *Vehicle Power and Propulsion Conference (VPPC), 2011 IEEE*, sept. 2011, pp. 1 –7.

[15] J. Cao, N. Schofield, and A. Emadi, "Battery balancing methods: A comprehensive review," in *Vehicle Power and Propulsion Conference, 2008. VPPC '08. IEEE*, sept. 2008, pp. 1 –6.

[16] W. Bentley, "Cell balancing considerations for lithium-ion battery systems," in *Battery Conference on Applications and Advances, 1997., 12th Annual*, jan 1997, pp. 223 –226.

[17] P. Krein, "Battery management for maximum performance in plug-in electric and hybrid vehicles," in *Vehicle Power and Propulsion Conference, 2007. VPPC 2007. IEEE*, sept. 2007, pp. 2 –5.

[18] W. Bentley, "Cell balancing considerations for lithium-ion battery systems," in *Battery Conference on Applications and Advances, 1997., Twelfth Annual*.   IEEE, 1997, pp. 223–226.

[19] J. Cao, N. Schofield, and A. Emadi, "Battery balancing methods: A comprehensive review," in *Vehicle Power and Propulsion Conference, 2008. VPPC '08. IEEE*, sept. 2008, pp. 1 –6.

[20] P. A. Cassani and S. S. Williamson, "Significance of battery cell equalization and monitoring for practical commercialization of plug-in hybrid electric vehicles," in *Applied Power Electronics Conference and Exposition, 2009. APEC 2009. Twenty-Fourth Annual IEEE.* IEEE, 2009, pp. 465–471.

[21] D. Andrea, *Battery Management Systems for Large Lithium Ion Battery Packs*, 1st ed. Artech House, 9 2010.

[22] M. Malinowski, K. Gopakumar, J. Rodriguez, and M. Pérez, "A survey on cascaded multilevel inverters," *Industrial Electronics, IEEE Transactions on*, vol. 57, no. 7, pp. 2197 –2206, july 2010.

[23] J. Rodriguez, L. Franquelo, S. Kouro, J. Leon, R. Portillo, M. Prats, and M. Perez, "Multilevel converters: An enabling technology for high-power applications," *Proceedings of the IEEE*, vol. 97, no. 11, pp. 1786 –1817, nov. 2009.

[24] O. Josefsson, A. Lindskog, S. Lundmark, and T. Thiringer, "Assessment of a multilevel converter for a PHEV charge and traction application," in *Electrical Machines (ICEM), 2010 XIX International Conference on*, sept. 2010, pp. 1 –6.

[25] M. Rashid, *Power Electronics Handbook: Devices, Circuits, and Applications*, ser. Academic Press. Elsevier, 2010.

[26] N. Mohan, T. M. Undeland, and W. P. Robbins, *Power Electronics: Converters, Applications, and Design*, 3rd ed. John Wiley & Sons; 2003, 2003.

[27] T. Reddy, *Linden's Handbook of Batteries, 4th Edition*, 4th ed. McGraw-Hill Professional, 10 2010.

[28] U. A. B. Consortium *et al.*, "Usabc goals for advanced batteries for evs," *Southfield, MI: USABC*, 2006.

[29] F. USCAR, "Usabc energy storage goals for power-assist hevs."

[30] A. A. Pesaran, T. Markel, H. S. Tataria, and D. Howell, *Battery Requirements for Plug-in Hybrid Electric Vehicles–analysis and Rationale.* National Renewable Energy Laboratory, 2009.

REFERENCES

[31] E. Karden, S. Ploumen, B. Fricke, T. Miller, and K. Snyder, "Energy storage devices for future hybrid electric vehicles," *Journal of Power Sources*, vol. 168, no. 1, pp. 2–11, 2007.

[32] C. Chan and Y. S. Wong, "Electric vehicles charge forward," *Power and Energy Magazine, IEEE*, vol. 2, no. 6, pp. 24–33, 2004.

[33] S. G. Chalk and J. F. Miller, "Key challenges and recent progress in batteries, fuel cells, and hydrogen storage for clean energy systems," *Journal of Power Sources*, vol. 159, no. 1, pp. 73–80, 2006.

[34] N. Chaturvedi, R. Klein, J. Christensen, J. Ahmed, and A. Kojic, "Algorithms for advanced battery-management systems," *Control Systems, IEEE*, vol. 30, no. 3, pp. 49–68, 2010.

[35] K. A. Smith, C. D. Rahn, and C.-Y. Wang, "Control oriented 1d electrochemical model of lithium ion battery," *Energy Conversion and Management*, vol. 48, no. 9, pp. 2565–2578, 2007.

[36] S. J. Moura, "Techniques for battery health conscious power management via electrochemical modeling and optimal control," Ph.D. dissertation, Pennsylvania State University, 2011.

[37] R. Elger, "On the behaviour of the lithium ion battery in the hev application," Ph.D. dissertation, KTH Royal Institute of Technology, 2004.

[38] J. Newman and W. Tiedemann, "Porous-electrode theory with battery applications," *AIChE Journal*, vol. 21, no. 1, pp. 25–41, 1975.

[39] F. Codeca, S. Savaresi, and G. Rizzoni, "On battery state of charge estimation: A new mixed algorithm," in *Control Applications, 2008. CCA 2008. IEEE International Conference on*, sept. 2008, pp. 102 – 107.

[40] M. Chen and G. Rincon-Mora, "Accurate electrical battery model capable of predicting runtime and i-v performance," *Energy Conversion, IEEE Transactions on*, vol. 21, no. 2, pp. 504 – 511, june 2006.

[41] H. He, R. Xiong, X. Zhang, F. Sun, and J. Fan, "State-of-charge estimation of the lithium-ion battery using an adaptive extended kalman filter based on an improved thevenin model," *Vehicular Technology, IEEE Transactions on*, vol. 60, no. 4, pp. 1461 –1469, may 2011.

[42] R. Steinbrecher, A. Radmehr, K. M. Kelkar, and S. V. Patankar, "Use of flow network modeling (fnm) for the design of air-cooled

84

servers," in *Advances in Electronics Packaging, Proceedings of the Pacific RIM/ASME Intersociety Electronics and Photonic Packaging Conference*, vol. 2, 1999, pp. 1999–2008.

[43] P. Liu, J. Wang, J. Hicks-Garner, E. Sherman, S. Soukiazian, M. Verbrugge, H. Tataria, J. Musser, and P. Finamore, "Aging mechanisms of lifepo4 batteries deduced by electrochemical and structural analyses," *Journal of the Electrochemical Society*, vol. 157, no. 4, pp. A499–A507, 2010.

[44] B. Scrosati and J. Garche, "Lithium batteries: Status, prospects and future," *Journal of Power Sources*, vol. 195, no. 9, pp. 2419–2430, 2010.

[45] S. Moura, J. Forman, S. Bashash, J. Stein, and H. Fathy, "Optimal control of film growth in lithium-ion battery packs via relay switches," *Industrial Electronics, IEEE Transactions on*, vol. 58, no. 8, pp. 3555–3566, 2011.

[46] K. Smith, J. Neubauer, E. Wood, M. Jun, and A. Pesaran, "Models for battery reliability and lifetime," 2013.

[47] M. Ecker, J. B. Gerschler, J. Vogel, S. Käbitz, F. Hust, P. Dechent, and D. U. Sauer, "Development of a lifetime prediction model for lithium-ion batteries based on extended accelerated aging test data," *Journal of Power Sources*, vol. 215, pp. 248–257, 2012.

[48] M. Broussely, S. Herreyre, P. Biensan, P. Kasztejna, K. Nechev, and R. Staniewicz, "Aging mechanism in li ion cells and calendar life predictions," *Journal of Power Sources*, vol. 97, pp. 13–21, 2001.

[49] R. Darling and J. Newman, "Modeling side reactions in composite $Li_yMn_2O_4$ electrodes," *Journal of The Electrochemical Society*, vol. 145, no. 3, pp. 990–998, 1998.

[50] A. V. Randall, R. D. Perkins, X. Zhang, and G. L. Plett, "Controls oriented reduced order modeling of solid-electrolyte interphase layer growth," *Journal of Power Sources*, vol. 209, pp. 282–288, 2012.

[51] G. L. Plett, "Algebraic solution for modeling sei layer growth," *ECS Electrochemistry Letters*, vol. 2, no. 7, pp. A63–A65, 2013.

[52] D. Andre, C. Appel, T. Soczka-Guth, and D. U. Sauer, "Advanced mathematical methods of soc and soh estimation for lithium-ion batteries," *Journal of Power Sources*, 2012.

REFERENCES

[53] L. Lu, X. Han, J. Li, J. Hua, and M. Ouyang, "A review on the key issues for lithium-ion battery management in electric vehicles," *Journal of Power Sources*, vol. 226, pp. 272–288, 2013.

[54] Y. Zheng, M. Ouyang, L. Lu, J. Li, X. Han, and L. Xu, "On-line equalization for lithium-ion battery packs based on charging cell voltages: Part 1. equalization based on remaining charging capacity estimation," *Journal of Power Sources*, vol. 247, pp. 676–686, 2014.

[55] C.-H. Kim, M. young Kim, H. sun Park, and G.-W. Moon, "A modularized two-stage charge equalizer with cell selection switches for series-connected lithium-ion battery string in an hev," *Power Electronics, IEEE Transactions on*, vol. 27, no. 8, pp. 3764–3774, 2012.

[56] A. Manenti, A. Abba, A. Merati, S. Savaresi, and A. Geraci, "A new bms architecture based on cell redundancy," *Industrial Electronics, IEEE Transactions on*, vol. 58, no. 9, pp. 4314–4322, 2011.

[57] M. Preindl, C. Danielson, and F. Borrelli, "Performance evaluation of battery balancing hardware," in *Control Conference (ECC), 2013 European*.   IEEE, 2013, pp. 4065–4070.

[58] L. Zhong, C. Zhang, Y. He, and Z. Chen, "A method for the estimation of the battery pack state of charge based on in-pack cells uniformity analysis," *Applied Energy*, vol. 113, pp. 558–564, 2014.

[59] Y. Zheng, L. Lu, X. Han, J. Li, and M. Ouyang, "Lifepo4 battery pack capacity estimation for electric vehicles based on charging cell voltage curve transformation," *Journal of Power Sources*, 2013.

[60] M. Fleckenstein, O. Bohlen, M. A. Roscher, and B. Bäker, "Current density and state of charge inhomogeneities in li-ion battery cells with LiFePO$_4$ as cathode material due to temperature gradients," *Journal of Power Sources*, vol. 196, no. 10, pp. 4769–4778, 2011.

[61] M. Malinowski, K. Gopakumar, J. Rodriguez, and M. Pérez, "A survey on cascaded multilevel inverters," *Industrial Electronics, IEEE Transactions on*, vol. 57, no. 7, pp. 2197 –2206, july 2010.

[62] H. Khalil, *Nonlinear systems*.   Prentice Hall, NJ, 2002.

[63] J. Kassakian, M. Schlecht, and G. Verghese, *Principles of Power Electronics*.   Addison-Wesley, 1991.

[64] S. Sirisukprasert, "The Modeling and Control of a Cascaded-Multilevel Converter-Based STATCOM," PhD Thesis, Virginia Tech, 2004.

[65] P. M. Bhagwat and V. Stefanovic, "Generalized structure of a multilevel pwm inverter," *Industry Applications, IEEE Transactions on*, vol. IA-19, no. 6, pp. 1057–1069, 1983.

[66] L. Li, D. Czarkowski, Y. Liu, and P. Pillay, "Multilevel selective harmonic elimination pwm technique in series-connected voltage inverters," *Industry Applications, IEEE Transactions on*, vol. 36, no. 1, pp. 160–170, 2000.

[67] J. Holtz, "Pulsewidth modulation for electronic power conversion," *Proceedings of the IEEE*, vol. 82, no. 8, pp. 1194–1214, 1994.

[68] N. Celanovic and D. Boroyevich, "A fast space-vector modulation algorithm for multilevel three-phase converters," *Industry Applications, IEEE Transactions on*, vol. 37, no. 2, pp. 637–641, 2001.

[69] S. Kouro, M. Perez, H. Robles, and J. Rodriguez, "Switching loss analysis of modulation methods used in cascaded h-bridge multilevel converters," in *Power Electronics Specialists Conference, 2008. PESC 2008. IEEE*, 2008, pp. 4662–4668.

[70] B. McGrath and D. Holmes, "Multicarrier pwm strategies for multilevel inverters," *Industrial Electronics, IEEE Transactions on*, vol. 49, no. 4, pp. 858–867, 2002.

[71] D. Holmes and B. McGrath, "Opportunities for harmonic cancellation with carrier-based pwm for a two-level and multilevel cascaded inverters," *Industry Applications, IEEE Transactions on*, vol. 37, no. 2, pp. 574–582, 2001.

[72] O. Josefsson, "Energy efficiency comparison between two-level and multilevel inverters for electric vehicle applications," Ph.D. dissertation, 2013.

[73] N. Murgovski, "Optimal powertrain dimensioning and potential assessment of hybrid electric vehicles," Ph.D. dissertation, 2013.

[74] H. Black, *Modulation theory*, ser. Bell Telephone Laboratories series. Van Nostrand, 1953.

[75] S. Bowes and B. Bird, "Novel approach to the analysis and synthesis of modulation processes in power convertors," *Electrical Engineers, Proceedings of the Institution of*, vol. 122, no. 5, pp. 507–513, 1975.

[76] D. Holmes and T. Lipo, *Pulse Width Modulation for Power Converters: Principles and Practice*, ser. IEEE Press Series on Power Engineering. John Wiley & Sons, 2003.

[77] B. McGrath and D. Holmes, "A general analytical method for calculating inverter dc-link current harmonics," *Industry Applications, IEEE Transactions on*, vol. 45, no. 5, pp. 1851 –1859, sept.-oct. 2009.

[78] F. Vasca and L. Iannelli, Eds., *Dynamics and Control of Switched Electronic Systems: Advanced Perspectives for Modeling, Simulation and Control of Power Converters (Advances in Industrial Control)*, 2012th ed.   Springer, 3 2012.

Part II

Included papers

Paper 1

On Thermal and State-of-Charge Balancing
using Cascaded Multi-level Converters

Faisal Altaf, Lars Johannesson, Bo Egardt

Comment: The layout of this paper has been reformatted in
order to comply with the rest of the thesis.

On Thermal and State-of-Charge Balancing using Cascaded Multi-level Converters

Faisal Altaf, Lars Johannesson, Bo Egardt

Abstract

In this study, the simultaneous use of a multi-level converter (MLC) as a DC-motor drive and as an active battery cell balancer is investigated. MLCs allow each battery cell in a battery pack to be independently switched on and off, thereby enabling the potential non-uniform use of battery cells. By exploiting this property and the brake regeneration phases in the drive cycle, MLCs can balance both the state of charge (SoC) and temperature differences between cells, which are two known causes of battery wear, even without reciprocating the coolant flow inside the pack. The optimal control policy (OP) that considers both battery pack temperature and SoC dynamics is studied in detail based on the assumption that information on the state of each cell, the schedule of reciprocating air flow and the future driving profile are perfectly known. Results show that OP provides significant reductions in temperature and in SoC deviations compared with the uniform use of all cells even with uni-directional coolant flow. Thus, reciprocating coolant flow is a redundant function for a MLC-based cell balancer. A specific contribution of this paper is the derivation of a state-space electro-thermal model of a battery submodule for both uni-directional and reciprocating coolant flows under the switching action of MLC, resulting in OP being derived by the solution of a convex optimization problem.

1 Introduction

Although battery technology has evolved significantly during the last decade, batteries of both plug-in hybrid electric vehicles (PHEVs) and electric vehicles (EVs) contribute a large percentage of the total vehicle cost. Consequently, the success of PHEVs and of EVs depends on the development of a battery that will not wear out prematurely to avoid additional battery replacement during the expected lifespan of the vehicle. The battery

pack (BP) of EVs/HEVs/PHEVs is built from a large number of small cells connected in series and parallel to meet both the traction power demand and the electric range requirement. Depth of discharge (DoD) is one of the most important factors that determine degradation of battery cells, such as battery operation at higher DoD shorten the cycle life and vice versa [1–4]. Therefore, the cycle life of a battery is significantly short when it undergoes full charge-discharge cycles, whereas the cycle life becomes significantly longer when it only undergoes partial charge-discharge cycles [5]. In a pack with state of charge (SoC) and capacity deviations among its cells, some of the cells undergo charge-discharge cycles at higher DoD than others. Consequently, these cells may reach their end-of-life (EOL) sooner. Thus, maintaining a perfect balance between SoC and DoD of each cell in the battery pack is crucial in prolonging battery life. This balance can be achieved by either passive or active balancing schemes based on various topologies of switched capacitive and resistive circuits, as illustrated in [6–9]. The main principle of all active balancing schemes is to transfer the charge from cells with higher SoC to cells with lower SoC by using switched capacitors that act as intermediate storage banks. Passive balancing schemes typically utilize differences in cell voltage to burn excess charge in resistor banks.

Aside from DoD, cell temperature is known to have a strong effect on battery wear, such as hotter cells degrade more quickly than colder cells [10–13]. More importantly, the presence of a few overheated cells can wear out the entire battery prematurely. The temperature imbalance between cells is due to variation in internal resistances, in the temperature gradient in the coolant due to convective heat transfer inside the battery pack, and the non-uniform external local thermal disturbances [13], [14]. The lifespan of a Li-Ion cell is reportedly reduced by two months for each degree increase in operating temperature from 30 to 40°C [15]. However, when temperature increases beyond 40°C, the cycle life of a battery decreases drastically.

Forced convection cooling is typically used to maintain batteries within the recommended temperature range. However, this method cannot compensate for the temperature gradient along the coolant fluid stream. Cells that are closer to the air inlet will be cooler than those further down the coolant stream. Reciprocating air flow (RF) was proposed in [10] and in [14] as a mean to reduce the effects of the temperature gradient in the coolant stream. However, in the present study, it is shown that cells continue to suffer from non-uniform local heated spots in the presence of parameter variation and local disturbances.

Considering the aforementioned causes of battery wear, the battery management unit (BMU) should balance both SoC and temperature differences between cells. Therefore, this paper investigates the MLC-based active cell

balancing scheme that allows hot cells to be bypassed, consequently balancing both SoC and temperature without the need for RF.

Cascaded MLCs [16], [17] had been investigated for electric drives in HEVs and in EVs in [18], [19]. MLC consists of n cascaded H-bridges (HBs) with an isolated battery cell for each HB. In this paper, the combination of HB and a battery cell is referred to as a power cell (PC). MLCs in EV/HEV/PHEV application are intended to reduce inverter losses and total harmonic distortion in the generated waveform for the electric machine. The usual switching strategy in motor drive applications of MLCs is the phase-shifted pulse width modulation (PS-PWM) technique that achieves the uniform use of cascaded cells [16], [17].

However, MLC presents an additional advantage as the cells need not be uniformly used over a time window of one or several voltage waveforms. By non-uniformly using the cells and by exploiting the brake regeneration phases in the drive cycle, an MLC cell balancer can balance both SoC and temperature differences. In this study, the PS-PWM scheme is referred to as the uniform duty cycle operation (UDCO), whereas the optimal scheme that controls the duty cycle of each PC to balance both SoC and temperature is referred to as optimal control policy (OP). The potential benefit of using MLC to balance both SoC and temperature of battery cells under a unidirectional flow (UF) has been thoroughly investigated and compared with that of UDCO [20]. Thus, the main contribution of the current study is to investigate OP under RF, and then to compare the results in detail with those of OP under UF. OP is calculated based on the assumption of perfect information of the SoC and the temperature of each cell, as well as of the future driving. This paper examines whether OP provides more significant improvements compared with UDCO under UF and RF and whether RF presents any potential benefits for OP-based active cell balancing.

For simplicity, this study employs a DC machine as the electric machine and models the cells by resistive circuits. Moreover, the simulation study focuses on an air-cooled battery sub-module (BSM) with a string of five series-connected cells. The coolant flow is assumed to be laminar with known inlet temperature and speed. In [21], only one configuration of the five-cell string was studied to evaluate the performance of the MLC-based cell balancer. A similar method was adopted in the present study. However, a more thorough analysis was conducted to carefully assess the performance of the cell balancer. For purpose of evaluation, two different variants of the five-cell string were studied. In the first variant, the higher resistance cell is located at the end of the string in the downstream of the coolant fluid. In the second variant, the higher resistance cell is located in the middle of the string. The resistance of the thermally exposed cell was assumed

to be almost 50% higher than that of others cells when comparing the performance of UDCO and OP under both UF and RF.

Besides the simulation results and the evaluation of MLC as a cell balancer, another important contribution of this paper is the detailed derivation of a state-space electro-thermal model of BSM under the switching action of MLC under UF and RF. The model was formulated in such a way that a convex optimization problem yields OP under a perfectly known future driving. This model can be used in future research in deciding the duty cycle in a receding horizon model predictive control scheme [22] based on the best available prediction of future driving.

The paper is organized as follows. Section 2 introduces the basic function of MLC. Section 3 presents the detailed electro-thermal modeling of BSM under the switching action of MLC. The optimization problem and the numerical solution method are described in Section 4. Section 5 presents the simulation results and the comparison between OP and the UDCO schemes under both UF and RF. A detailed discussion on the simulation results is provided in Section 6. The conclusions are given in Section 7.

2 Multi-level Converters Overview

This section provides a short introduction on single-phase MLC. In contrast to two-level converters that consist of a single large battery connected with a single HB, MLC as shown in Fig. 1 has several series-connected PCs in which each PC contains an HB and the independent battery cell.

HB, which consists of two half-bridges, is a switch mode dc-dc power converter [23] that produces a four-quadrant controllable dc output using four switches, namely, $S_{i1}, S_{i2}, \bar{S}_{i1}, \bar{S}_{i2}$ as shown in Fig. 1. The MoSFETs are normally used for these switches. To avoid a shoot-through problem, only one of the switch pairs, $(S_{i1}, \bar{S}_{i2})$, $(S_{i2}, \bar{S}_{i1})$, (S_{i1}, S_{i2}) or $(\bar{S}_{i1}, \bar{S}_{i2})$ is switched on at a time. $(S_{i1}, \bar{S}_{i2})$ generates positive output voltage v_{Li} from PC$_i$, $(S_{i2}, \bar{S}_{i1})$ generates a negative v_{Li}, and both (S_{i1}, S_{i2}) and $(\bar{S}_{i1}, \bar{S}_{i2})$ generate $v_{Li} = 0$. Therefore, the following three modes of operation can be defined for each PC$_i$ depending on the switch pair that is switched on: *Mode–1* ($v_{Li} > 0$), *Mode–2* ($v_{Li} < 0$), and *Mode–3* ($v_{Li} = 0$). To model these three modes of operation, $s_{ij}(t) = 1$ is defined as the ON-State and $s_{ij}(t) = 0$ is defined as the OFF-State of the switch S_{ij} where 'i' corresponds to PC$_i$ and $j \in \{1, 2\}$ denotes one of the two half-bridges in HB. Therefore,
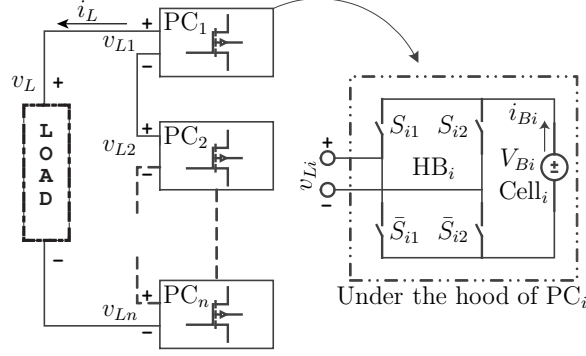
Figure 1: Block diagram of a single-phase cascaded HB MLC.

the switching function $s_i(t)$ for Cell$_i$ can be defined as

$$s_i(t) = s_{i1}(t) - s_{i2}(t) = \begin{cases} 1, & \textit{Mode–1} \\ -1, & \textit{Mode–2} \\ 0, & \textit{Mode–3} \end{cases} \tag{1}$$

Thus all three modes of HB can be defined in terms of $s_i(t)$. The switching vector $s(t) = \begin{bmatrix} s_1(t) & \cdots & s_n(t) \end{bmatrix}^T$ contains the switching functions for all n PCs inside the MLC. With the assumption of an ideal switch behavior, the ohmic and the switching losses can be ignored. Therefore, the input and the output of HB are related through the switching function $s_i(t)$, as shown in Fig. 2. Thus, the current in Cell$_i$ is given by

$$i_{Bi}(t) = i_L(t)s_i(t) \tag{2}$$

As a result of the series connection, the same load current i_L passes through
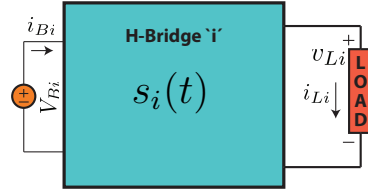
Figure 2: Switching Model of HB

each PC. However, the direction of the current passing through Cell$_i$ depends on the selection of switches and on the direction of load current i_L. Similarly the voltage output from each PC$_i$ is defined by $v_{Li}(t) = V_{Bi}(t)s_i(t)$. Hence, the total voltage output from MLC can be written as the sum of the voltage output from each PC$_i$ as given below.

$$v_L = \sum_{i=1}^{n} v_{Li} = \sum_{i=1}^{n} V_{Bi}(t)\, s_i(t) \tag{3}$$

97

The number of voltage levels that MLC generates depends on the number of PCs and on the terminal voltage V_{Bi} of Cell$_i$. If the terminal voltage of all cells is the same, MLC can then generate $L = 2\,n + 1$ different voltage levels (v_L).

3 Modeling of Cell Balancing System with RF

The block diagram of the cell balancing system for RF and for UF is shown in Fig. 3. MLC is capable of generating the same output voltage level v_L in several ways by using different combinations of the three modes for various PCs, providing redundancy in generating the same load voltage through numerous possible switch combinations. This redundancy adds an extra degree of freedom (DoF) that is utilized in this paper to design the optimal control signal u_i for Cell$_i$. Consequently, SoC and temperature differences between cells are kept within a certain zone, while satisfying all other operating requirements. In this section, a switching model and an averaged state-space model of a PC is derived based on the assumption that the load is a DC machine. Finally, the complete state-space model for n PCs is developed.
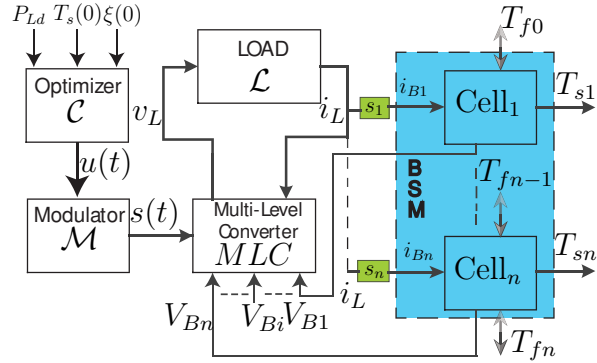
Figure 3: Conceptual block diagram of a battery cell balancing system with RF. $T_s(0)$ is a vector containing the initial temperature of all cells, and $\xi(0)$ is a vector containing the initial SoC of all cells, P_{Ld} is the demanded power for load with the known voltage and current profile, and $T_{f0}, \cdots, T_{fn}$ represent temperatures of temperature-nodes of the coolant fluid. The subsystem inside the blue box represents BSM being balanced and the green boxes contain the switching functions for the corresponding cell.

3.1 Switching Model of a Power Cell

In this subsection, the electro-thermal model of a switched battery cell under RF is derived. Each PC_i is assumed to contain only one $Cell_i$. The dynamics of cell temperature depends on several factors such as coolant properties, cell material properties, cell placement and battery pack configuration. In [14], the forced-convection cooled battery pack was modeled by the *lumped-capacitance thermal model* and by the *flow network model* (FNM). In the said study, the battery pack was configured as $n_s S n_p P$ that represents n_p parallel strings, with each string, called a battery module, containing n_s cells connected in a series. A sufficient amount of free space is present between the cells to allow streams of laminar flow of the coolant (air). A configuration of the battery pack, Li-Ion cells, and the air properties adopted in the present paper are similar to those in [14]. Various coefficients for the thermal and the physical properties of the cell and of the air used in this study are listed in Table 1. Details are provided in [14]. $C_{Ni}\,[Ah]$

Table 1: Definition of Battery Parameters

Parameters	Expression	Parameters	Expression
$a_{si}\,\left[\frac{1}{s}\right]$	$\left(\frac{1}{C_{si}R_{ui}}\right)$	$b_{ri}\,[\Omega]$	R_{si}
$a_{ei1}\,\left[\frac{1}{s}\right]$	$\left(\frac{1}{R_{i1}C_{i1}}\right)$	α_i [Unitless]	$R_{ui}c_{\mathrm{f}}$
$a_{ei2}\,\left[\frac{1}{s}\right]$	$\left(\frac{1}{R_{i2}C_{i2}}\right)$	β_i [Unitless]	$-1+\alpha_i$
$b_{si}\,\left[\frac{\Omega K}{W\,s}\right]$	$\left(\frac{R_{si}}{C_{si}}\right)$	$b_{ei2}\,\left[\frac{V}{s\,A}\right]$	$\left(\frac{1}{C_{i2}}\right)$
$b_{ei1}\,\left[\frac{V}{s\,A}\right]$	$\left(\frac{1}{C_{i1}}\right)$	$b_{ei3}\,\left[\frac{1}{A\,s}\right]$	$\left(\frac{1}{3600C_{Ni}}\right)$

represents the nominal capacity of $Cell_i$, and $R_{ui}\,[KW^{-1}]$ the convection thermal resistance for $Cell_i$ that depends on the geometry of the battery cell, on the coolant fluid properties, and on the Nusselt number, which, in turn, depends on the Reynolds number.

The coefficient $C_{si} = \rho_{si}c_{psi}V_{si}\,[JK^{-1}]$ represents *heat capacity* (amount of heat energy required to raise the temperature of $Cell_i$ by 1 Kelvin), where ρ_{si} is the density, c_{psi} is the *Specific Heat Capacity* (heat capacity per unit mass of battery), and $V_{si}\,[m^3]$ is the volume of $Cell_i$. The coefficient $c_f = \rho_f c_{pf}\dot{V}_f\,[WK^{-1}]$ is *thermal conductance* of the coolant fluid. All other quantities are shown in Fig. 4.

In this paper, only one submodule (of the battery module) that consists of n series-connected battery cells is studied. First, the thermal model is derived separately for the coolant flow in each direction. The two models

are then combined to create the model for RF. In this study, both RF and UF are examined and compared. Hence, the case of *forward flow* (i.e. from lower to higher cell index) is designated as UF for ease of reference. The thermal model proposed in [14] does not consider any power electronic switching of the battery cells. Thus, power electronic switching must be incorporated into the current framework. The previous model was modified by embedding the switching function $s_i(t)$ and subsequently combining it with the enhanced Thevenin equivalent electrical model, shown in Fig. 4 to derive the switching electro-thermal model of PC_i.

For *forward flow*, the dynamics of the surface temperature $T_{si} [K]$ of $Cell_i$ in terms of $i_L(t)$ and $s_i(t)$, after substituting the value of $i_{Bi}(t)$ from equation (2) into the model proposed in [14], is given by

$$\dot{T}_{si} = -a_{si}T_{si} + b_{si}i_L^2 s_i^2 + a_{si}T_{fi-1}, \quad \forall i = \{1, \cdots, n\} \tag{4}$$

where the $i_L^2 s_i^2$ represents the instantaneous ohmic power losses on $Cell_i$ and $T_{fi-1} [K]$ is the temperature of temperature node '$i-1$' (of the fluid element modeled by FNM) attached to $Cell_i$ in an upstream direction. Equation (4) is not that interesting in terms of control design because it explicitly depends on the fluid node temperature T_{fi-1} for $Cell_i$ that is not directly known. Therefore, this equation must be modified to remove this explicit dependency. For control design purpose, the temperature dynamics of each cell can be more appropriately modeled in terms of battery current $i_{Bi} = i_L s_i$ and of the temperature $T_{fin} \in \{T_{f0}, T_{fn}\}$ of the coolant fluid at the inlet. To achieve this T_{fi-1} is eliminated from equation (4) as follows. According to [14], the temperatures of the nodes '$i-1$' and 'i' are related by

$$T_{fi} = \frac{(T_{si} + \beta_i T_{fi-1})}{\alpha_i}, \forall i \tag{5}$$

where α_i and β_i are defined in Table 1. Given that T_{f0} is a known quantity, then by forward recursion of equation (5), any T_{fi} can be expressed as a function of the inlet fluid temperature T_{f0} and the temperatures T_{s1} to T_{si} of the battery cells, such as

$$T_{f1} = \left(\frac{1}{\alpha_1}\right) T_{s1} + \left(\frac{\beta_1}{\alpha_1}\right) T_{f0},$$

$$T_{f2} = \left(\frac{\beta_2}{\alpha_1 \alpha_2}\right) T_{s1} + \left(\frac{1}{\alpha_2}\right) T_{s2} + \left(\frac{\beta_1 \beta_2}{\alpha_1 \alpha_2}\right) T_{f0}, \tag{6}$$

$$T_{f3} = \left(\frac{\beta_2 \beta_3}{\alpha_1 \alpha_2 \alpha_3}\right) T_{s1} + \left(\frac{\beta_3}{\alpha_2 \alpha_3}\right) T_{s2} + \left(\frac{1}{\alpha_3}\right) T_{s3} + \left(\frac{\beta_1 \beta_2 \beta_3}{\alpha_1 \alpha_2 \alpha_3}\right) T_{f0},$$

and so on. Therefore, the general equation for any T_{fi} is written as follows:

$$T_{fi} = a_{fi1}^{(1)} T_{s1} + a_{fi2}^{(1)} T_{s2} + \cdots + a_{fii}^{(1)} T_{si} + b_{fi}^{(1)} T_{f0} \tag{7}$$

where:

$$a_{fii}^{(1)} = \left(\frac{1}{\alpha_i}\right), \quad b_{fi}^{(1)} = \left(\frac{\prod_{k=1}^{i} \beta_k}{\prod_{k=1}^{i} \alpha_k}\right), \quad \forall i \geq 1 \tag{8}$$

$$a_{fij}^{(1)} = \left(\frac{\prod_{k=(j+1)}^{i} \beta_k}{\prod_{k=j}^{i} \alpha_k}\right), \quad \forall i > j, \quad a_{fij}^{(1)} = 0, \quad \forall i < j \tag{9}$$

Using equation (7) in (4), the thermal dynamics of the battery cells can be re-written as follows:

$$\dot{T}_{si} = a_{ti1}^{(1)} T_{s1} + \cdots + a_{tin}^{(1)} T_{sn} + b_{si} i_L^2 s_i^2 + b_{ti}^{(1)} T_{f0} \tag{10}$$

where:

$$a_{tii}^{(1)} = -a_{si}, \quad \forall i \geq 1 \tag{11}$$

$$a_{tij}^{(1)} = \left(\frac{\prod_{k=(j+1)}^{(i-1)} \beta_k}{\prod_{k=j}^{(i-1)} \alpha_k}\right) a_{si}, \quad \forall i > j, \quad a_{tij}^{(1)} = 0, \quad \forall i < j \tag{12}$$

$$b_{ti}^{(1)} = \left(\frac{\prod_{k=1}^{(i-1)} \beta_k}{\prod_{k=1}^{(i-1)} \alpha_k}\right) a_{si}, \quad \forall i \geq 1 \tag{13}$$

Analogous to the *forward flow* case, the thermal dynamics of Cell$_i$ is derived for *reverse coolant flow* (i.e. from higher to lower cell index). The result is given below

$$\dot{T}_{si} = a_{ti1}^{(2)} T_{s1} + \cdots + a_{tin}^{(2)} T_{sn} + b_{si} i_L^2 s_i^2 + b_{ti}^{(2)} T_{fn} \tag{14}$$

where T_{fn} is the temperature of the inlet fluid entering BSM from the Cell$_n$ side. The other coefficients are defined as follows:

$$a_{tii}^{(2)} = a_{tii}^{(1)}, \quad \forall i \geq 1, \quad b_{ti}^{(2)} = b_{t(n-i+1)}^{(1)}, \quad \forall i \geq 1 \tag{15}$$

$$a_{tij}^{(2)} = a_{tji}^{(1)}, \quad \forall i < j, \quad a_{tij}^{(2)} = 0, \quad \forall i > j \tag{16}$$

The electrical equivalent model of a battery cell is shown in Fig. 4. This model is an enhanced Thevenin Model with two time constant behavior [24–26]. The dynamic model for this circuit is given by

$$\dot{V}_{i1} = -a_{ei1}V_{i1} + b_{ei1}i_L s_i, \tag{17}$$

$$\dot{V}_{i2} = -a_{ei2}V_{i2} + b_{ei2}i_L s_i, \tag{18}$$

$$\dot{\xi}_i = -b_{ei3}i_L s_i, \tag{19}$$

$$V_{Bi} = f(\xi_i) - V_{i1} - V_{i2} - b_{ri}i_L s_i \tag{20}$$

where i_{Bi} is the current flowing through Cell_i and ξ_i is the normalized SoC of Cell_i. $\xi_i \in [0, 1]$ is a unit-less quantity. V_{i1} and V_{i2} are the voltages across capacitors C_{i1} and C_{i2}, respectively, and V_{Bi} is the output voltage of Cell_i. The SoC-dependent open circuit voltage is given by $V_{oci} = f(\xi_i)$ where $f : [0, 1] \to \mathbb{R}_0^+$ is a function of SoC. Equations (10)–(20) describe the switched behavior of the battery under the switching action of MLC, in terms of the load current $i_L(t)$ and of the switching function $s_i(t)$. Therefore, this model can be considered as a *switching model* of PC_i.
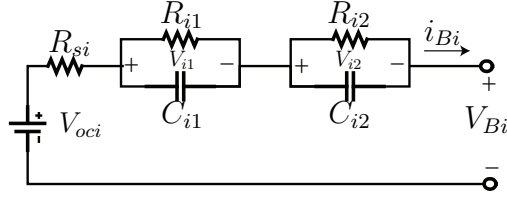

Figure 4: Electrical model of a battery cell.

3.2 Averaged-State-Space Model of PC

Cell balancing can be formulated as an optimization problem using two approaches. In the first approach, cell operation is optimized by directly using the switching function $s_i(t)$ as an optimization variable for Cell_i. The switching function $s_i(t)$ in equation (1) can only attain values from the discrete set $\{-1, 0, 1\}$. Hence, the computed optimal control is a discrete-valued signal. In this case, the system is normally modeled as a switched system with various modes of operation, and the optimization problem therefore becomes combinatorial that is normally difficult to solve because of its non-convex nature. However, the aim of this study is to evaluate OP, which necessitates a model with a real-valued control signal because such models are far easier to handle in optimization problems than those with discrete-valued signals. Hence, the second control approach is used instead, wherein the battery duty cycle $u_i \in [-1, 1]$, which is the average of the switching input function $s_i(t)$, is used as optimization variables for Cell_i. The optimizer computes a control vector signal u that contains duty cycles $u_i \in [-1, 1]$ for each PC_i. Note that the negative duty cycle means operation in *Mode–2*. The computed control u is then fed to the modulation block $\mathcal{M}$, which then generates an appropriate switching function $s_i \in s(t)$ for each PC. Given that the switching model (10)–(20) involves discrete-valued signals $s_i(t)$, these signals must be transformed into real-valued averaged signals to modify the system model (10)–(20) accordingly. The use of averaging is justified by the fact that, in most cases, the switching frequency F_s inside the

modulator $\mathcal{M}$ is significantly higher than the bandwidth f_L of the system. Thus, by assuming that $F_s \gg f_L$ and by employing the two-time scale separation principle [27], the concept of averaging can be employed, [28], [29]. In other words, the system response is assumed to be determined predominantly by the duty cycle $u_i(t) \in [-1, 1]$ or the average of the switching input function $s_i(t)$. In addition, careful derivation is required given that the switching model involves certain bilinear and quadratic terms. In this section, the averaged model is derived in detail by averaging each signal over one switching cycle. The following assumptions are made in deriving the average quantities:

Assumption 1.1. The switching function can only attain values either from set $\{0, 1\}$ or $\{0, -1\}$ during any switching cycle of period T_s. This assumption implies that it is not allowed to charge and to discharge the battery cell during the same switching cycle.

Assumption 1.2. The load current $i_L(t)$ remains fairly constant during any switching cycle. This assumption is justified based on the discussion above.

Assumption 1.3. All internal electrical states $V_{i1} = \bar{V}_{i1}$, $V_{i2} = \bar{V}_{i2}$, and $\xi_i = \bar{\xi}_i$, as well as terminal voltage V_{Bi}, remains fairly constant during the switching cycle.

Based on these assumptions, the average of the switching function $s_i(t)$, which is also called the duty-cycle, is given by

$$u_i(t) = \bar{s}_i(t) = \frac{1}{T_s} \int_{t-T_s}^{t} s_i(t)\mathrm{d}t = \pm\frac{T_{on}}{T_s} \tag{21}$$

where T_{on} is the ON time of a switch during any switching interval. This equation shows that $u_i(t)$ can attain any continuous real value in the interval $[-1, 1]$, depending on the value of T_{on}. All other averaged signals can be defined in terms of $u_i(t)$ and $i_L(t)$ as follows:

$$\bar{i}_{Bi}(t) = u_i\, i_L, \quad i_{Br_i}^2 = |u_i| i_L^2 \tag{22}$$
$$\bar{v}_{Li} = \left(f(\bar{\xi}_i) - \bar{V}_{i1} - \bar{V}_{i2}\right) u_i - b_{ri}|u_i| i_L \tag{23}$$

where $\bar{i}_{Bi}$ is the average current flowing through Cell$_i$ during interval T_s, i_{Br_i} is the root-mean-square (RMS) current that incurs equivalent ohmic loss across Cell$_i$ during one switching cycle, and $\bar{v}_{Li}$ is the average output voltage from PC$_i$ during period T_s of any switching cycle. [20] presents the detailed derivation of all the averaged variables. Using the averaged

quantities, the *averaged-model* of PC_i is written as follows:

$$\dot{\bar{T}}_{si} = a_{ti1}^{(\sigma)} \bar{T}_{s1} + \cdots + a_{tin}^{(\sigma)} \bar{T}_{sn} + b_{si} i_L^2 |u_i| + b_{ti}^{(\sigma)} T_{fin} \tag{24}$$

$$\dot{\bar{V}}_{i1} = -a_{ei1}\bar{V}_{i1} + b_{ei1}i_L u_i \tag{25}$$

$$\dot{\bar{V}}_{i2} = -a_{ei2}\bar{V}_{i2} + b_{ei2}i_L u_i \tag{26}$$

$$\dot{\bar{\xi}}_i = -b_{ei3}i_L u_i \tag{27}$$

$$\bar{V}_{Bi} = f(\bar{\xi}_i) - \bar{V}_{i1} - \bar{V}_{i2} - b_{ri}i_L u_i \tag{28}$$

where $\sigma = 1$ and $\sigma = 2$ designate the forward and the reverse coolant flow, respectively and $T_{fin} \in \{T_{f0}, T_{fn}\}$ is the known fluid temperature in one of the two inlets depending on the direction of the coolant flow. Given that $|u_i|$ in (24) is not continuously differentiable, u_i and $|u_i|$ are defined in terms of two new control variables u_{i1} and u_{i2} that are defined as $u_{i1} = \max\{0, u_i\} \in [0, 1]$ and $u_{i2} = \max\{0, -u_i\} \in [0, 1]$, respectively. Thus, $u_i = (u_{i1} - u_{i2}) \in [-1, 1]$ and $|u_i| = (u_{i1} + u_{i2}) \in [0, 1]$. u_{i1} can then be interpreted as the duty cycle for Mode–1, whereas u_{i2} can be interpreted as the duty cycle for Mode–2. In this new context, u_{i1} and u_{i2} cannot be both non-zero simultaneously (cf. assumption 1.1) at any time for safety reasons, which if violated can cause a shoot-through problem. Based on this newly defined control signal, the thermal subsystem of battery $Cell_i$ for reciprocating coolant flow is given by

$$\dot{X}_{ti} = a_{ti1}^{(\sigma)} X_{t1} + \cdots + a_{tin}^{(\sigma)} X_{tn} + \hat{g}_{ti}(x_L) \hat{u}_i + b_{ti}^{(\sigma)} T_{fin} \tag{29}$$

where $X_{ti} = \bar{T}_{si} \in \mathbb{R}$, $\hat{g}_{ti}(x_L) = \begin{bmatrix} b_{si}x_L^2 & b_{si}x_L^2 \end{bmatrix}$, $\hat{u}_i = \begin{bmatrix} u_{i1} & u_{i2} \end{bmatrix}^T \in \mathbb{R}^2$, and $x_L = i_L$. Similarly, the electrical subsystem of $Cell_i$ is given by

$$\dot{X}_{ei} = A_{ei}X_{ei} + \hat{g}_{ei}(x_L) \hat{u}_i \tag{30}$$

where $X_{ei} = \begin{bmatrix} X_{ei1} & X_{ei2} & X_{ei3} \end{bmatrix}^T \in \mathbb{R}^3$ with $X_{ei1} = \bar{V}_{i1}$, $X_{ei2} = \bar{V}_{i2}$, $X_{ei3} = \bar{\xi}_i$ and $A_{ei} = \text{diag}(-a_{ei1}, -a_{ei2}, 0) \in \mathbb{R}^{3\times3}$, $\hat{g}_{ei}(x_L) = \begin{bmatrix} b_{ei}x_L & -b_{ei}x_L \end{bmatrix} \in \mathbb{R}^{3\times2}$ with $b_{ei} = \begin{bmatrix} b_{ei1} & b_{ei2} & -b_{ei3} \end{bmatrix}^T$.

3.3 Complete Averaged State-Space Model of n-Cell MLC

An n–MLC can be represented in various state-space models depending on the number of cells and on the configuration in which they are connected inside each PC_i. In this model, each PC_i is assumed to contain only one $Cell_i$. Using equations (29) and (30) as basic building blocks, the state-space system for the thermal subsystem of n cells can be written as follows:

$$\dot{X}_t = A_t^{(\sigma)} X_t + \hat{G}_t(x_L) \hat{u} + W_t^{(\sigma)} T_{fin}, \quad Y = C_t X_t \tag{31}$$

where $A_t^{(\sigma)} \in \mathbb{R}^{n \times n}$ is the system matrix in which $A_t^{(1)}$ is the lower triangular matrix with coefficients $a_{tij}^{(1)}$ defined by equations (11) and (12) for forward coolant flow, $A_t^{(2)} = (A_t^{(1)})^T$ is the upper triangular matrix with coefficients $a_{tij}^{(2)}$ defined by equations (15) and (16) for reverse coolant flow, $\hat{G}_t(x_L) = \text{diag}\left(\hat{g}_{t1}(x_L), \cdots, \hat{g}_{tn}(x_L)\right) \in \mathbb{R}^{n \times 2n}$ is the load current-dependent input matrix for the thermal subsystem, $W_t^{(\sigma)} = \begin{bmatrix} b_{t1}^{(\sigma)} & \cdots & b_{tn}^{(\sigma)} \end{bmatrix}^T \in \mathbb{R}^n$, with coefficients $b_{ti}^{(\sigma)}$ defined by equation (13) for $\sigma = 1$ and equation (15) for $\sigma = 2$ is the scaling vector for the inlet fluid temperature, $C_t = I_n \in \mathbb{R}^{n \times n}$ is the output matrix, $X_t = \begin{bmatrix} X_{t1} & \cdots & X_{tn} \end{bmatrix}^T \in \mathbb{R}^n$ is the thermal state vector, $\hat{u} = \begin{bmatrix} \hat{u}_1^T & \cdots & \hat{u}_n^T \end{bmatrix}^T \in \mathbb{R}^{2n}$ is the input vector, $T_{fin} \in \mathbb{R}$ is the known fluid temperature (T_{f0} or T_{fn}) in one of two inlets depending on the direction of the coolant flow, and $Y \in \mathbb{R}^n$ is the output vector. Similarly, the electrical subsystem of n–cells is given by

$$\dot{X}_e = A_e X_e + \hat{G}_e(x_L)\,\hat{u} \tag{32}$$

where $A_e = \text{diag}\left(A_{e1}, \cdots, A_{en}\right) \in \mathbb{R}^{3n \times 3n}$ is the system matrix, $\hat{G}_e(x_L) = \text{diag}\left(\hat{g}_{e1}(x_L), \cdots, \hat{g}_{en}(x_L)\right) \in \mathbb{R}^{3n \times 2n}$ is the load current-dependent input matrix for the electrical subsystem, $X_e = \begin{bmatrix} X_{e1}^T & \cdots & X_{en}^T \end{bmatrix}^T \in \mathbb{R}^{3n}$ is the electrical state vector, and $\hat{u} \in \mathbb{R}^{2n}$ is the input vector. Subsequently, the two subsystems can be combined in diagonal form.

$$\underbrace{\begin{bmatrix} \dot{X}_t \\ \dot{X}_e \end{bmatrix}}_{\dot{X}} = \underbrace{\begin{bmatrix} A_t^{(\sigma)} & 0 \\ 0 & A_e \end{bmatrix}}_{A^{(\sigma)}} \underbrace{\begin{bmatrix} X_t \\ X_e \end{bmatrix}}_{X} + \underbrace{\begin{bmatrix} \hat{G}_t(x_L) \\ \hat{G}_e(x_L) \end{bmatrix}}_{\hat{G}(x_L)} \hat{u} + \underbrace{\begin{bmatrix} W_t^{(\sigma)} \\ 0 \end{bmatrix}}_{W^{(\sigma)}} T_{fin}$$

$$\dot{X} = A^{(\sigma)} X + \hat{G}(x_L)\hat{u} + W^{(\sigma)} T_{fin}, \quad Y = CX \tag{33}$$

where $A^{(\sigma)} \in \mathbb{R}^{4n \times 4n}$ is the system matrix, $\hat{G}(x_L) \in \mathbb{R}^{4n \times 2n}$ is the load current-dependent input matrix for complete system, $C = \begin{bmatrix} C_t & 0 \end{bmatrix} \in \mathbb{R}^{n \times 4n}$ is the output matrix, $X \in \mathbb{R}^{4n}$ is the state vector, $\hat{u} \in \mathbb{R}^{2n}$ is the input vector, and $W^{(\sigma)} \in \mathbb{R}^{4n}$ is the scaling vector for the inlet fluid temperature. The averaged state-space electro-thermal model under RF, as shown in equation (33), is a *piecewise affine* (PWA) system.

Remark 1.1. *The control signal u_i can be used to determine the modes of HB_i and $Cell_i$ inside each PC_i at any time 't'. The mode in which HB_i inside any PC_i is operating can be determined by algorithm 1. Similarly, algorithm 2 can be used to determine the mode of $Cell_i$ (i.e., whether it is charging or discharging) inside any PC_i.*

Algorithm 1 H-Bridge Mode Determination at any time 't'

$u_i = \begin{bmatrix} 1 & -1 \end{bmatrix} \hat{u}_i$
if $u_i(t) > 0$ **then**
    HB_i in Mode–1 at time 't'
else if $u_i(t) < 0$ **then**
    HB_i in Mode–2 at time 't'
else
    HB_i in Mode–3 at time 't'
end if

Algorithm 2 Battery Mode Determination at any time 't'

$u_i = \begin{bmatrix} 1 & -1 \end{bmatrix} \hat{u}_i$
if $x_L(t)\,u_i(t) > 0$ **then**
    $Cell_i$ is Discharging at time 't'
else if $x_L(t)\,u_i(t) < 0$ **then**
    $Cell_i$ is Charging at time 't'
else
    $Cell_i$ is Disconnected at time 't'
end if

---

4 Optimization Problem

In this section, an optimization problem is formulated for the OP scheme to achieve cell balancing in terms of both temperature and SoC. The averaged state-space model derived in the previous section is used along with an objective function and certain constraints as described below.

4.1 Definition of Objective Function

The objective of this study is to equalize SoC of all cells at the final time and to maintain both SoC and temperature deviations among the cells within a certain zone during the entire drive cycle. These objectives will be specified as constraints in the next subsection. Another aim is to minimize temperature deviations among the battery cells, as specified in the following objective function:

$$J(Y) = \int_0^{t_f} (Y_1 - Y_2)^2 + \cdots + (Y_{n-1} - Y_n)^2 dt \tag{34}$$

To transform $J(Y)$ on the quadratic form in X, $Q = C^T \bar{Q}_1 \bar{Q}_1^T C$ is defined with $\bar{Q}_1 = \mathrm{diag}\,(q_1, \cdots, q_{n-1}) \in \mathbb{R}^{n \times (n-1)}$, where $q_i = \begin{bmatrix} 1 & -1 \end{bmatrix}^T$. Therefore, the objective function (34) can be rewritten as the following standard

quadratic form:

$$J(X) = \int_0^{t_f} X^T Q X dt \qquad (35)$$

4.2 Definition of Constraints

There are some hard (operational, safety and balancing) constraints that need to be respected by OP. The objective of balancing SoC is defined in terms of the following zone and terminal constraints. During run-time, SoC of all cells must stay within a certain zone from each other, as given by

$$-\Delta SoC \leq (X_{ei3}(t) - X_{ej3}(t)) \leq \Delta SoC,$$
$$\forall t, \forall i,\, j \in \{1, 2, \cdots, n\} \qquad (36)$$

and at the final time, SoC of all cells should be equal:

$$X_{ei3}(t_f) = X_{ej3}(t_f) \quad \forall i,\, j \in \{1, 2, \cdots, n\} \qquad (37)$$

In addition, SoC of Cell$_i$ must stay within following zone:

$$0 \leq X_{ei3}(t) \leq 1 \quad \forall t, \forall i \in \{1, 2, \cdots, n\} \qquad (38)$$

To ensure tight thermal balancing, in addition to minimizing the deviations of cell temperatures, a hard constraint maintains temperature deviations among the cells in the following zone:

$$-\Delta T_s \leq (T_{si}(t) - T_{sj}(t)) \leq \Delta T_s \quad \forall t,\, \forall i,\, j \in \{1, \cdots, n\} \qquad (39)$$

Moreover, a safety constraint on the maximum operating temperature of each cell is present.

$$T_{si}(t) \leq T_{\text{smax}} \quad \forall t, \forall i \in \{1, 2, \cdots, n\} \qquad (40)$$

where T_{smax} is the maximum operating temperature allowed for Cell$_i$. The objective to track the demanded load voltage (v_{Ld}) can be written as the following constraint:

$$v_{Ld} = \sum_{i=1}^n \left[(f(X_{ei3}) - X_{ei1} - X_{ei2})\, u_i - b_{ri}|u_i|\, x_L \right] \qquad (41)$$

where v_{Ld} is normally provided by the higher supervisory block called Energy Management System (EMS) in the context of HEVs. $u_i = \begin{bmatrix} 1 & -1 \end{bmatrix} \hat{u}_i$ represents the duty cycle of Cell$_i$. In this study, $f(X_{ei3})$ is assumed to be constant, while X_{ei1} and X_{ei2} are negligible, which are normal assumptions

in developing EMS for (P)HEVs [30]. These assumptions preserve the convexity of the problem. Moreover, a constraint is identified on the maximum current that each battery cell can supply.

$$x_L\, u_i \in \left[\bar{i}_{Bimin}, \bar{i}_{Bimax}\right] \tag{42}$$

where $\bar{i}_{Bimin}$ and $\bar{i}_{Bimax}$ are the minimum and the maximum battery current limits, respectively. Certain constraints are also present on the control signal $\hat{u}_i = \begin{bmatrix} u_{i1} & u_{i2} \end{bmatrix}^T \in \mathbb{R}^2$, which are given by

$$u_{i1} \in [0,1], \quad u_{i2} \in [0,1], \quad |u_i| = (u_{i1} + u_{i2}) \in [0\,,1],$$
$$\text{and} \quad u_i = (u_{i1} - u_{i2}) \in [-1\,,1] \tag{43}$$

Based on the definitions of u_{i1} and u_{i2} in the previous section, these values cannot be nonzero simultaneously to avoid a shoot-through problem. Thus, the following constraint is imposed to ensure safety:

$$u_{i1}\, u_{i2} = 0 \tag{44}$$

However, the last constraint is non-convex and must be removed to preserve convexity of the problem.

4.3   Definition of the Optimization Problem

The optimization problem can subsequently be written as follows:

$$J^0 = \min_{\hat{u}} \int_0^{t_f} X^T Q X \mathrm{d}t \quad \text{subject to}$$
$$\begin{cases} \dot{X} = A^{(\sigma)} X + \hat{G}(x_L)\hat{u} + W^{(\sigma)} T_{f\text{in}}, \\ \text{Constraints}\ \ (36) - (44), \\ x_L(t),\ T_{f\text{in}}\ \text{and}\ \sigma\ \text{are known at each time step.} \end{cases} \tag{P-I}$$

The optimization problem (P-I) is non-convex because of the non-convex constraint $u_{i1}\, u_{i2} = 0$. In the next subsection, certain assumptions are formulated to restore convexity and to simplify the problem.

4.4   Solving the Optimization Problem Using CVX

The problem (P-I) was solved by CVX, which is a MATLAB-based package for specifying and for solving convex programs [31], [32] and uses a disciplined convex programming ruleset [33]. CVX transforms MATLAB® into a modeling language, allowing constraints and objectives to be specified using standard MATLAB expression syntax.

The non-convex constraint $(u_{i1}\,u_{i2} = 0)$ must be removed prior to establishing the optimization problem (P-I) in CVX. In this study, cell balancing is achieved by assuming that the modes of all PCs belong *either* to set {Mode–1 , Mode–3} *or* to {Mode–2 , Mode–3} *but not* to {Mode–1 , Mode–2} at any time instant. In other words, it is not allowed at any time instant to charge and to discharge cells simultaneously. Based on this assumption, the sign of u_i can be pre-decided based on the sign of a known demanded load voltage (v_{Ld}). Therefore, at $v_{Ld} \geq 0$, $u_{i2} = 0$ and $u_i = (u_{i1} - u_{i2}) \geq 0$. Otherwise $u_{i1} = 0$ and consequently, $u_i \leq 0$. Therefore, the non-convex constraint $(u_{i1}\,u_{i2} = 0)$ need not be specified. The system was discretized using Euler's approximation at sampling time $h = 1\,\mathrm{sec}$. The simulation parameters are shown in Table 2, where $\bar{R}_s$ is the nominal value of series resistance R_{si} of any Cell$_i$, N is the prediction (or driving) horizon in discrete time, and τ is the reciprocation period or the period in which the coolant completes one cycle of uniform forward and reverse flow.

Table 2: Simulation Parameters

Parameters	Value	Parameters	Value
n	5	$\bar{i}_{Bimin}$	$-200\,A$, $\forall i$
t_f	$12\,min$	$\bar{i}_{Bimax}$	$200\,A$, $\forall i$
h	$1\,sec$	ΔT_s	$2°C$
N	$t_f/h = 720$	ΔSoC	0.1
$\bar{R}_s$	$6.2770\,m\Omega$	T_{smax}	$40°C$
R_{s5} or R_{s3}	$1.48\bar{R}_s = 9.29\,\mathrm{m}\Omega$	T_{fin}	$20°C$
$T_{si}(0)$	$25°C$, $\forall i$	τ	$60\,sec$

5 Simulation Results

A few variables must be introduced before the simulation results are presented. These variables are illustrated in plots for more clarity. $\bar{X}_{ti} = \frac{1}{N}\sum_{k=0}^{N} X_{ti}(k)$ is defined as the average temperature of Cell$_i$ on the entire driving horizon N and $\bar{X}_{tb} = \frac{1}{n}\sum_{i=1}^{n} \bar{X}_{ti}$ is the average temperature of BSM. Similarly, the *normalized average power loss per unit ohm* across any Cell$_i$ on the entire driving horizon is given by

$$\bar{I}_i = \frac{\frac{1}{N}\sum_{k=1}^{N} i^2_{Br_i}(k)}{\max_j \left(\frac{1}{N}\sum_{k=1}^{N}(i^{ou}_{Br_j}(k))^2\right)} \tag{45}$$
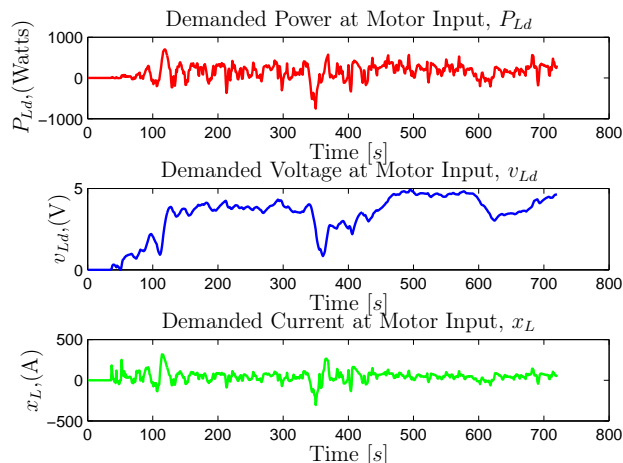
Figure 5: Drive Cycle: Demanded Power, Voltage, and Current Profile. Two short duration high power peaks exist: (1) around 120 seconds and (2) around 350 seconds.

where $i^{ou}_{Br_j}$ is the RMS current through $Cell_j$ for OP under UF, as defined by equation (22). The superscripts 'o' and 'u' distinguish the signals of OP from UDCO, whereas the superscripts 'u' and 'r' represent UF and RF, respectively. Fig. 5 shows the drive cycle data comprising the demanded power, voltage, and current profiles used in the simulations. In the following sections, the simulation results of two different cell configurations are presented to thoroughly evaluate the effectiveness of the proposed OP. In configuration-1, the cell with 50% higher resistance is assumed to be the last downstream cell ($Cell_5$) in the five-cell string, whereas in configuration-2, the cell with higher resistance is assumed to be connected in the middle (i.e., at position of $Cell_3$) of the string. Both string configurations are discussed separately below to show the implications of OP.

5.1 Configuration-1: Downstream $Cell_5$ has higher resistance

In this subsection, the performances of UDCO and OP under both UF and RF are evaluated. $Cell_5$ is assumed to have almost 50% higher series resistance because of aging or of some other effect. The temperature (X_{ti}), SoC (ξ_i), and the normalized average per unit power loss ($\bar{I}_i$) are plotted for each cell. Note that the assumption about 50% increase in internal resistance is not unrealistic as according to [34] the battery internal resistance may vary significantly as a function of its cycle-life. The simulation results are shown for both OP and UDCO in Fig. 7 for RF and Fig. 8 for UF.
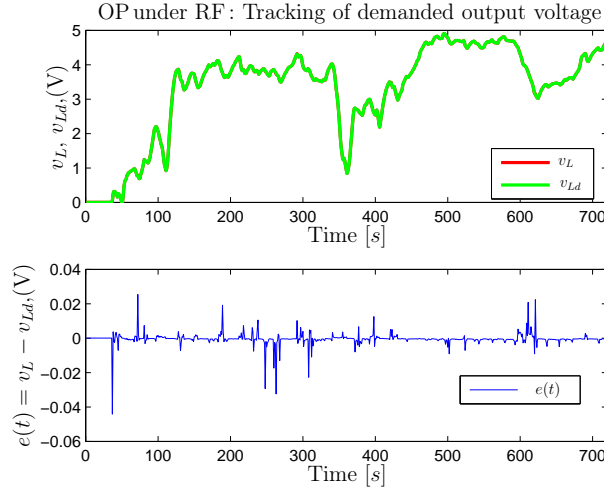
Figure 6: Tracking of demanded output voltage. The figure shows that OP tracks the demanded output voltage with significantly small error. The tracking performance is the same for string configurations 1 and 2.

OP versus UDCO under RF:

Fig. 6 shows the output voltage generated by MLC and the good tracking performance with a significantly small error for OP. The temperatures of all cells under RF are shown for OP in Fig. 1.7(a) and for UDCO policy in Fig. 1.7(b). The temperature of $Cell_5$ under RF for the UDCO policy is significantly higher than that of OP. Moreover, OP achieved good thermal balancing while maintaining the temperatures of all cells within $\pm 2°C$ and SoC within $\pm 10\%$ from each other, as shown in Fig. 1.7(c). SoC for the UDCO policy is not shown. However, a uniform decay is assumed for each cell. Fig. 1.9(b) shows the normalized average unit power loss $\bar{I}_i$ for each cell under RF. The horizontal dashed black line illustrates the average unit power loss $\bar{I}_i^{ur}$ across each cell for the UDCO policy, whereas the colored vertical bars illustrate the average unit power loss $\bar{I}_i^{or}$ across each cell for the OP scheme. The internal resistance R_{s5} of $Cell_5$ is almost 50% higher than that of other cells. Thus, as shown in Fig. 1.9(b), the naturally optimal policy is the least use of $Cell_5$ compared with others and $Cell_1$, under best thermal conditions, should be used most.

OP versus UDCO under UF:

The temperatures of all cells are shown for OP in Fig. 1.8(a) and for UDCO policy in Fig. 1.8(b) under UF. Fig. 1.9(a) shows the normalized average unit power loss for each cell under UF. OP again performs better than the UDCO policy, as demonstrated in the figure. Similar to the RF case, OP

simultaneously achieved good thermal and SoC balancing by using $Cell_5$, which is the most downstream cell with 50% higher resistance, least compared with the others whereas $Cell_1$ is used most. [20] presents a more detailed comparison between OP and UDCO under UF.

Optimal Power Loss Distributions for UF and RF:

Fig. 1.9(a) and 1.9(b) demonstrate the normalized average unit power loss for UF and RF cases, respectively. These figures demonstrate the effect of the coolant flow scheme on optimal decisions of OP. The difference between the average unit power loss in UF and that in RF should be noted, particularly the difference between the optimal power loss distributions for $Cell_5$ in the two cases. In the RF case the $Cell_5$, that is no longer a downstream cell, can benefit from coolant reciprocation. Thus, OP decides to use it almost 10% more (in terms of losses) than that of the UF case. Although the optimal power loss distribution is different in both cases, the temperature increase of the cells is the same, as shown in Figures 1.8(a) and 1.7(a). This similarity indicates that OP automatically handles the coolant flow scheme and decides on the optimal power loss distribution over each cell accordingly. OP likewise handles thermal imbalances caused by resistance variation and by the temperature gradient in the coolant. Fig. 1.9(a) shows that in the UF case, optimal power loss distribution between two adjacent cells differs by almost 10% due to the temperature gradient in the coolant. The difference in power loss distribution between two cells is almost 20% because of the resistance variation. This finding indicates that although the power loss difference due to resistance variations is large, power loss due to the coolant temperature gradient is also not negligible. Thus, active thermal balancing is still necessary to compensate for the temperature gradient in the coolant though no resistance variation occurs in the battery string. In recollection, no decision is ad hoc here, everything is handled systematically by solving the model-based optimization problem (P-I).

## 5.2   Configuration-2: Middle $Cell_3$ has higher resistance

In this subsection, the performances of UDCO and OP under both UF and RF are evaluated for configuration-2 of the five-cell string. In this case, the middle $Cell_3$, instead of $Cell_5$, is assumed to have almost 50% higher series resistance. The temperature (X_{ti}), SoC (ξ_i), and the normalized average per unit power loss ($\bar{I}_i$) are plotted for each cell. Simulation results are shown for both OP and UDCO in Fig.10 for RF and in Fig.11 for UF. The drive cycle data is the same as those presented previously (Fig. 5).
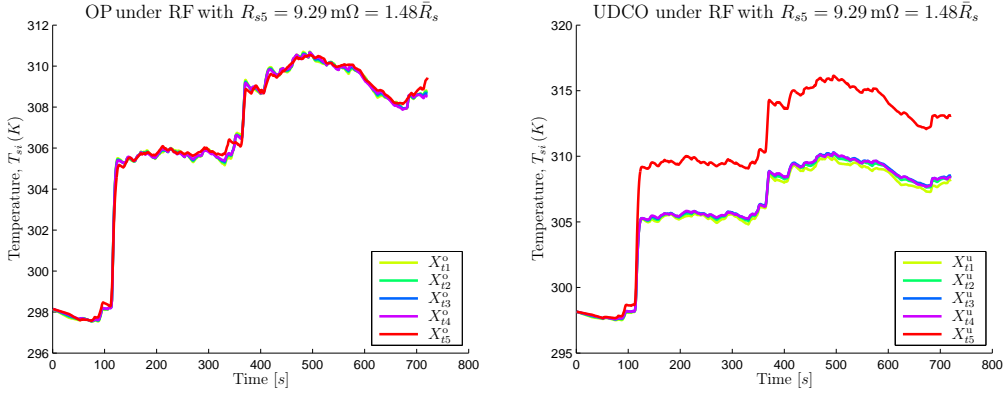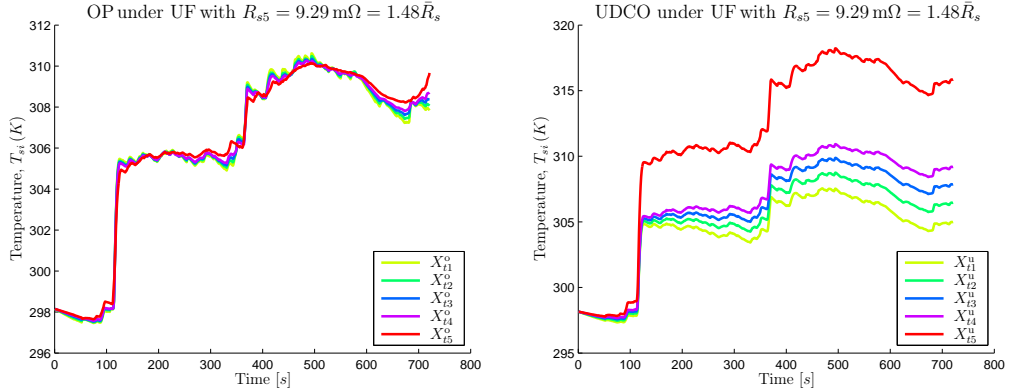
(a) Optimal Temperature of each cell for OP under RF. Despite R_{s5} being 50% higher, OP has successfully achieved thermal balancing among all cells.

(b) Temperature of each cell for UDCO under RF. Red: *Hottest Cell*, Light Green: *Coldest Cell*. Cell$_5$ suffers from thermal run away as shown in red.
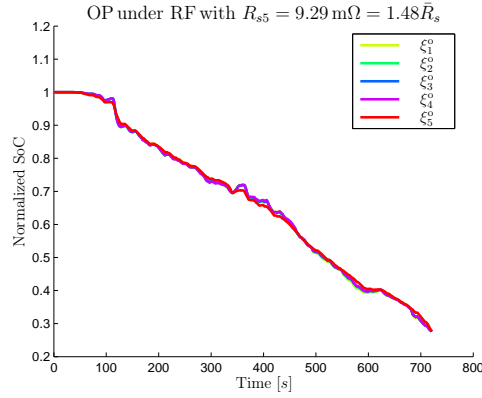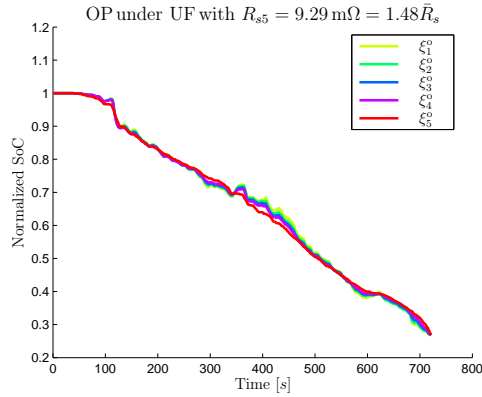

(c) Optimal SoC of each cell for OP under RF. The plot shows that OP has simultaneously achieved SoC and thermal balancing shown in Fig. 1.7(a).

Figure 7: **Configuration-1 under RF**: Simulation results and comparison between OP and UDCO for RF with the most downstream Cell5 having 50% higher resistance. The plots show that OP significantly performs better than UDCO under RF. The uniform use of cells is naturally not optimal in this situation because the resistance (R_{s5}) of the Cell$_5$ is 50% higher than that of the others. The plots also show that using RF is not highly helpful for UDCO under parameter variation. RF only helps to reduce temperature deviation in the cells with nominal resistance, while cells with higher resistance still suffer from thermal run away.

(a) Optimal Temperature of each cell for OP under UF. Despite R_{s5} being 50% higher, OP has successfully achieved thermal balancing among all cells.

(b) Temperature of each cell for UDCO under UF. Red: *Hottest Cell*, Light Green: *Coldest Cell*. Cell$_5$ suffers from thermal run away as shown in red.

(c) Optimal SoC of each cell for OP under UF. The plot shows that OP has simultaneously achieved SoC and thermal balancing shown in Fig. 1.8(a).

Figure 8: **Configuration-1 under UF**: Simulation results and comparison between OP and UDCO for UF with the most downstream Cell$_5$ having 50% higher resistance. The plots show that OP significantly performs better than UDCO under UF. The uniform use of cells is naturally not optimal in this situation because the resistance (R_{s5}) of the Cell$_5$ is 50% higher than that of others. Fig. 7 and 8 show that OP exhibits similar performance under UF and RF. Thus, RF is redundant for an MLC-based active cell balancing system when operated using OP.
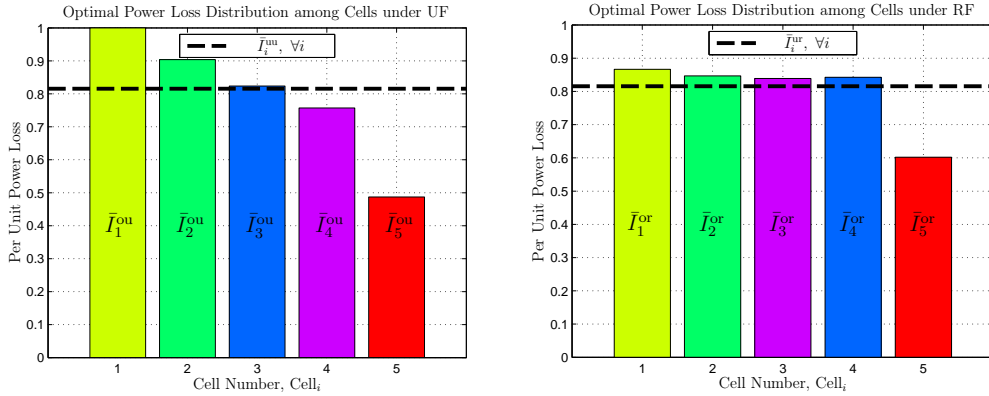
(a) Optimal normalized average power loss per unit ohm across Cell$_i$ for OP under UF. The dashed horizontal black line shows normalized unit power loss across Cell$_i$ for UDCO.

(b) Optimal normalized average power loss per unit ohm across Cell$_i$ for OP under RF. The dashed horizontal black line shows normalized unit power loss across Cell$_i$ for UDCO.
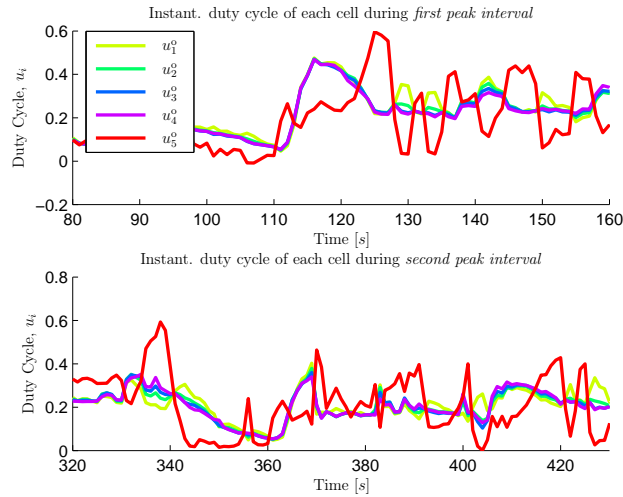
(c) Optimal instantaneous duty cycles for each cell during high current intervals for OP with RF. The plot shows that during high current intervals, OP least uses Cell$_5$ compared with other cells.

Figure 9: **Configuration-1 UF versus RF**: Optimal power loss distribution under UF and RF. These plots show that during high current intervals, OP least uses Cell$_5$ compared with other cells. Thus, Cell$_5$ provides less current during high current intervals and consequently, has less losses, as shown in Fig. 1.9(b). This is naturally optimal as losses are quadratic in current.

OP versus UDCO under RF:

Fig. 1.10(a) and 1.10(c) show the temperatures and SOC of all cells for OP under RF. Fig. 1.10(b) exhibits the temperature for the UDCO policy under RF. The temperature of $Cell_3$ for the UDCO policy is significantly higher under RF than that of OP in this configuration. Moreover, OP simultaneously achieved good thermal and SoC balancing while satisfying all constraints. Fig. 1.12(b) shows the normalized average unit power loss $\bar{I}_i$ that is optimally decided by OP for each cell. The internal resistance R_{s3} of $Cell_3$ is almost 50% higher than that of other cells. Thus, the natural OP least uses $Cell_3$ compared with other cells, and $Cell_1$ and $Cell_5$, under the best thermal conditions for the RF case, are used more.

OP versus UDCO under UF:

Fig. 1.11(a) and 1.11(b) show the temperatures of all cells for OP and for the UDCO policy, respectively. Fig. 1.12(a) presents the normalized average unit power loss for each cell under UF. As shown in the figures, OP performs better than UDCO. Similar to that in the RF case, OP simultaneously achieved good thermal and SoC balancing for this cell configuration by using $Cell_3$ least and $Cell_1$ the most compared with other cells, as shown in Fig. 1.12(a).

**Optimal Power Loss Distributions for UF and RF:**

Fig. 1.12(a) and 1.12(b) display the normalized average unit power loss for UF and for RF cases, respectively. These figures indicate the effect of the coolant flow scheme on the optimal decisions of OP. The optimal power loss distributions for $Cell_3$ in this configuration are relatively similar in both UF and RF cases. Given that $Cell_3$ is the middle cell, reciprocation has a slight influence on the optimal power loss decision of OP for this cell.

6   Discussion

In this section, some important implications of the simulation results are discussed.

6.1   Benefits of Reciprocating Air Flow

In this section, UF and RF are compared for both OP and UDCO. The temperatures of the cells for the UDCO policy under UF are shown in Fig. 1.8(b) for configuration-1 and in Fig. 1.11(b) for configuration-2. The
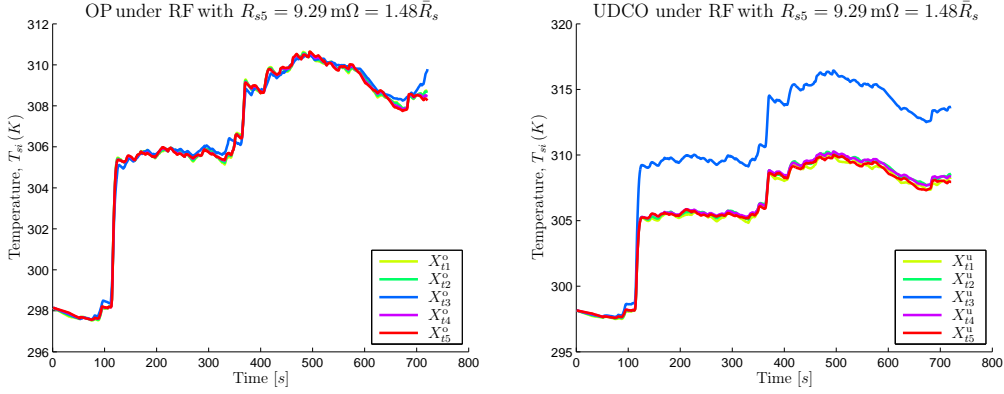
(a) Optimal Temperature of each cell for OP under RF.

(b) Temperature of cells for UDCO under RF. Cell$_3$ has higher temperature.
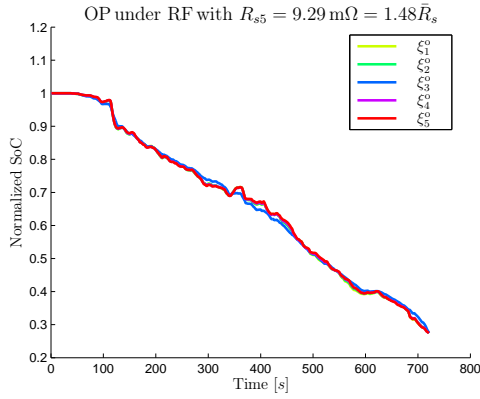
(c) Optimal SoC of each cell for OP under RF.

Figure 10: **Configuration-2 under RF**: Simulation results and comparison between OP and UDCO for RF with middle Cell$_3$ having 50% higher resistance. The plots show that OP significantly performs better than UDCO under RF. The Fig. 1.10(b) shows that using RF is not very helpful for UDCO under parameter variations.
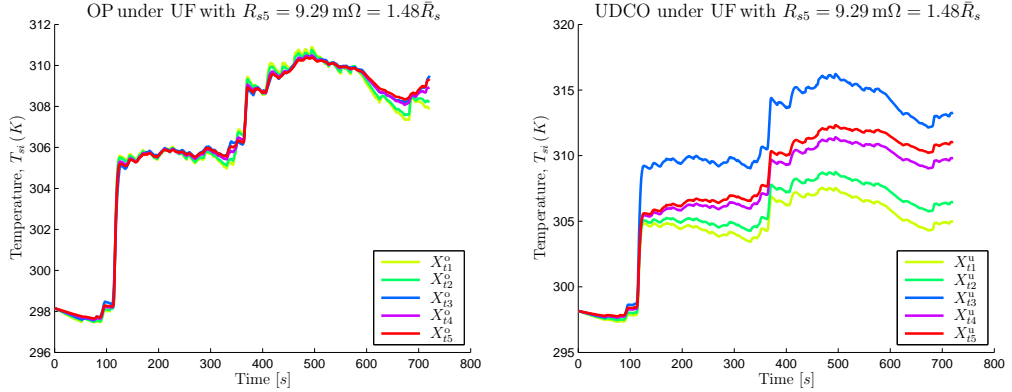
(a) Optimal Temperature of each cell for OP under UF.
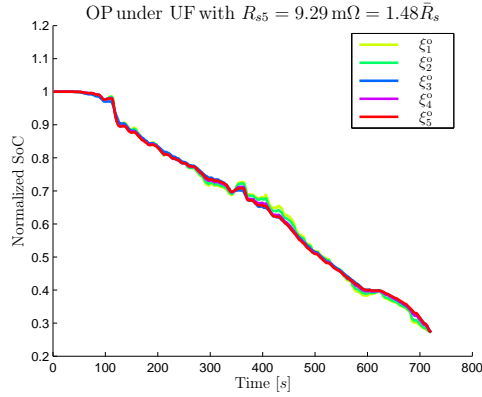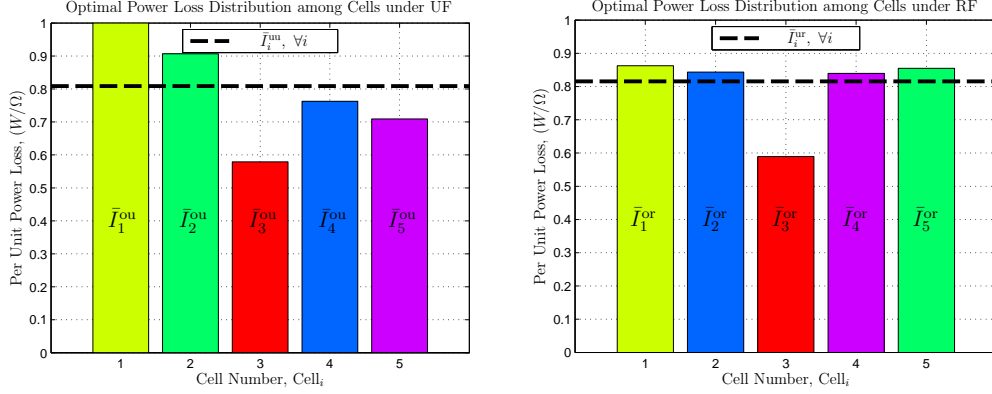

(b) Temperature of each cell for UDCO under UF.

(c) Optimal SoC of each cell for OP under UF.

Figure 11: **Configuration-2 under UF** : Simulation results and comparison between OP and UDCO for UF with middle Cell$_3$ having 50% higher resistance. The plots show that OP significantly performs better than UDCO under UF as well.

(a) Optimal normalized average power loss per unit ohm across Cell_i for OP under UF.

(b) Optimal instantaneous duty cycles for each cell during high current intervals for OP with RF.
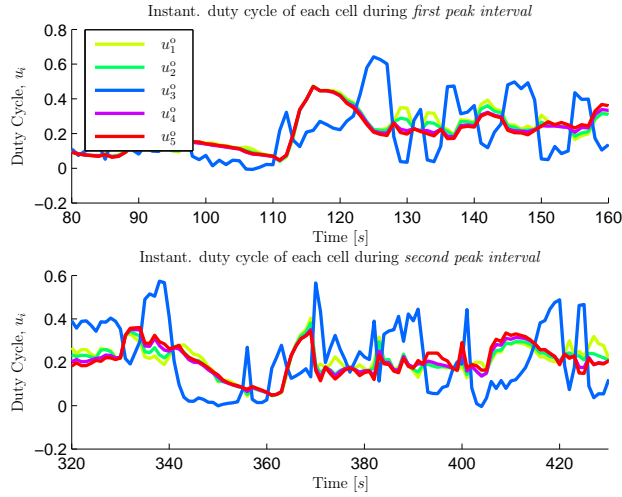
(c) Optimal instantaneous duty cycles for each cell during high current intervals for OP with RF.

Figure 12: **Configuration-2 UF versus RF** : : Optimal power loss distribution under UF and RF. These plots show that during high current intervals, OP least uses Cell_3 compared with other cells. Thus, Cell_3 sees less current during high current interval and consequently, has less losses, as shown in Fig. 1.12(b). This is naturally optimal as losses are quadratic in current.

temperatures of the cells for the UDCO policy under RF are exhibited in Fig. 1.7(b) for configuration-1 and in Fig. 1.10(b) for configuration-2. Similarly, the temperatures of the cells for OP under UF are shown in Fig. 1.8(a) for string configuration-1 and in Fig. 1.11(a) for string configuration-2. The temperatures of the cells for OP under RF are shown in Fig. 1.7(a) for string configuration-1 and in Fig. 1.10(a) for string configuration-2. These figures clearly show that OP has no significant gain when using RF, particularly for short series-connected battery string. The main purpose of RF is merely to achieve temperature uniformity. Using RF with the UDCO policy minimizes temperature deviations among cells with nominal resistance. However, it is not that useful for $Cell_5$ or $Cell_3$ that has 50% higher resistance. These figures clearly indicate that RF without OP can bring temperature uniformity only in the string having cells with same resistances. Moreover, the temperature gradient in the coolant under RF is negligible only for short strings of cells. For long strings, RF generally cannot remove this gradient completely. Thus, RF alone cannot solve the temperature non-uniformity problem in battery packs of EV/HEV/PHEV because these battery packs normally have long strings of cells with high possibility of having resistance differences. However, the temperature uniformity under said conditions can be achieved by optimally shifting the power losses among the cells using MLC-based OP even under UF. Thus in the presence of OP, RF is a redundant function.

6.2   Configuration-1 versus Configuration-2

In this subsection, the optimal power loss distribution for two string configurations is compared. Fig. 1.9(b) and 1.12(b) show that changing the position of the higher resistance cell in the string has slight influence on the power loss distribution in the RF case. However, the influence may be more noticeable in longer battery strings. In the case of UF, changing the position of the higher resistance cell always influence optimal decisions on power loss distribution. This finding can be validated by comparing the optimal power loss distributions of $Cell_5$ and $Cell_3$ in figures 1.9(a) and 1.12(a). The difference in power loss compensates for the temperature gradient in the coolant for the UF case.

A difference can be observed in the temperature dynamics for the two configurations under the UDCO policy, as illustrated in Fig. 1.11(b) and 1.8(b). This difference is due to higher resistance $Cell_3$ in the middle of the string for configuration-2, thereby generating more heat that results in higher temperature differential between $Cell_2$ and $Cell_3$. Meanwhile, temperatures of $Cell_1$ to $Cell_4$ for configuration-1 are distributed in a staircase

fashion because of uniform temperature gradient in the coolant. However, the temperature evolution of the two configurations is almost the same under OP, as shown in Fig. 1.11(a) and 1.8(a).

6.3 Working of OP in Nutshell

OP achieves thermal balancing by least using $Cell_5$ (or $Cell_3$) compared with other cells during high current intervals, as shown in Fig. 1.9(c) (or Fig. 1.12(c)). Thus, $Cell_5$ (or $Cell_3$) has less ohmic losses. This policy is naturally optimal as losses are quadratic in current. In a nutshell, OP achieves thermal balancing by avoiding the use of higher resistance cells during peak power intervals and by using the cell more frequently during low power intervals. Moreover, similarities can be observed between the optimal duty cycles of the switches in two different string configurations, as shown in Fig. 1.9(c) and 1.12(c).

7 Summary and Conclusions

This article investigated the potential benefit of optimally using the extra DoF of MLC for simultaneous balancing of SoC and temperature of cells under UF and RF. A complete state-space electro-thermal model was developed and a constrained convex optimization problem was formulated and solved based on the assumption that the state of each cell and the schedule of reciprocating air flow are perfectly known. The simulation results showed that at 50% increase in internal resistance of any cell, OP optimally uses the extra DoF of MLC, significantly reducing temperature deviation among the cells compared with the ad hoc uniform duty cycle operation. In a nutshell, OP achieves thermal balancing by optimally shifting the power losses among the cells depending on their resistance and positions in the string. Thus, OP can also achieve temperature uniformity under parameter variations even with UF, whereas RF cannot maintain temperature uniformity in such circumstances without OP. This study shows that using RF has no significant benefit when using an MLC-based OP. Thus, RF is considered a redundant function when an MLC-based active cell balancing system is operated using OP.

8 Acknowledgement

References

[1] I. Bloom, B. Cole, J. Sohn, S. Jones, E. Polzin, V. Battaglia, G. Henriksen, C. Motloch, R. Richardson, T. Unkelhaeuser *et al.*, "An accelerated calendar and cycle life study of li-ion cells," *Journal of Power Sources*, vol. 101, no. 2, pp. 238–247, 2001.

[2] B. Kuhn, G. Pitel, and P. Krein, "Electrical properties and equalization of lithium-ion cells in automotive applications," in *Vehicle Power and Propulsion, 2005 IEEE Conference*, sept. 2005, p. 5 pp.

[3] S. Lukic, J. Cao, R. Bansal, F. Rodriguez, and A. Emadi, "Energy storage systems for automotive applications," *Industrial Electronics, IEEE Transactions on*, vol. 55, no. 6, pp. 2258 –2267, june 2008.

[4] K. Smith, T. Markel, K. Gi-Heon, and A. Pesaran, "Design of electric drive vehicle batteries for long life and low cost," *Accelerated Stress Testing and Reliability (ASTR), IEE Workshop on*, Oct. 6-8 2010.

[5] T. Reddy, *Linden's Handbook of Batteries, 4th Edition*, 4th ed. McGraw-Hill Professional, 10 2010.

[6] W. C. Lee, D. Drury, and P. Mellor, "Comparison of passive cell balancing and active cell balancing for automotive batteries," in *Vehicle Power and Propulsion Conference (VPPC), 2011 IEEE*, sept. 2011, pp. 1 –7.

[7] J. Cao, N. Schofield, and A. Emadi, "Battery balancing methods: A comprehensive review," in *Vehicle Power and Propulsion Conference, 2008. VPPC '08. IEEE*, sept. 2008, pp. 1 –6.

[8] W. Bentley, "Cell balancing considerations for lithium-ion battery systems," in *Battery Conference on Applications and Advances, 1997., 12th Annual*, jan 1997, pp. 223 –226.

[9] P. Krein, "Battery management for maximum performance in plug-in electric and hybrid vehicles," in *Vehicle Power and Propulsion Conference, 2007. VPPC 2007. IEEE*, sept. 2007, pp. 2 –5.

[10] C. Park and A. Jaura, "Reciprocating battery cooling for hybrid and fuel cell vehicles," *ASME International Mechanical Engineering*

Congress and Exposition (IMECE2003), Washington, DC, USA, pp. 425–430, november 2003.

[11] ——, "Dynamic thermal model of Li-Ion battery for predictive behavior in hybrid and fuel cell vehicles," *SAE transactions*, vol. 112, no. 3, pp. 1835–1842, 2003.

[12] ——, "Transient heat transfer of 42 V Ni-MH batteries for an HEV application," *Future Car Congress*, 2002.

[13] A. Pesaran and B. S. Vlahinos, A, "Thermal performance of EV and HEV battery modules and packs," *Proceedings of the 14th International Electric Vehicle Symposium, Orlando, Florida*, December 1997.

[14] R. Mahamud and C. Park, "Reciprocating air flow for li-ion battery thermal management to improve temperature uniformity," *Journal of Power Sources*, vol. 196, no. 13, pp. 5685 – 5696, 2011.

[15] C. Motloch, J. Christophersen, J. Belt, R. Wright, G. Hunt, T. Tartamella, H. Haskins, and T. Miller, "High-Power Battery Testing Procedures and Analytical Methodologies for HEV's," *SAE 2002-01-1950*, 2002.

[16] J. Rodriguez, L. Franquelo, S. Kouro, J. Leon, R. Portillo, M. Prats, and M. Perez, "Multilevel converters: An enabling technology for high-power applications," *Proceedings of the IEEE*, vol. 97, no. 11, pp. 1786 –1817, nov. 2009.

[17] M. Malinowski, K. Gopakumar, J. Rodriguez, and M. Pérez, "A survey on cascaded multilevel inverters," *Industrial Electronics, IEEE Transactions on*, vol. 57, no. 7, pp. 2197 –2206, july 2010.

[18] L. Tolbert, F. Z. Peng, and T. Habetler, "Multilevel converters for large electric drives," *Industry Applications, IEEE Transactions on*, vol. 35, no. 1, pp. 36 –44, jan/feb 1999.

[19] O. Josefsson, A. Lindskog, S. Lundmark, and T. Thiringer, "Assessment of a multilevel converter for a PHEV charge and traction application," in *Electrical Machines (ICEM), 2010 XIX International Conference on*, sept. 2010, pp. 1 –6.

[20] F. Altaf, L. Johannesson, and B. Egardt, "Evaluating the potential for cell balancing using a cascaded multi-level converter using convex optimization," in *IFAC Workshop on Engine and Powertrain Control, Simulation and Modeling, 2012*, Oct. 2012.

[21] ——, "Performance evaluation of multilevel converter based cell balancer with reciprocating air flow," in *Vehicle Power and Propulsion Conference (VPPC), 2012 IEEE*, Oct. 2012, pp. 706–713.

[22] J. Rawlings, "Tutorial overview of model predictive control," *Control Systems, IEEE*, vol. 20, no. 3, pp. 38–52, Jun.

[23] N. Mohan, T. M. Undeland, and W. P. Robbins, *Power Electronics: Converters, Applications, and Design*, 3rd ed. John Wiley & Sons; 2003, 2003.

[24] F. Codeca, S. Savaresi, and G. Rizzoni, "On battery state of charge estimation: A new mixed algorithm," in *Control Applications, 2008. CCA 2008. IEEE International Conference on*, sept. 2008, pp. 102 – 107.

[25] M. Chen and G. Rincon-Mora, "Accurate electrical battery model capable of predicting runtime and i-v performance," *Energy Conversion, IEEE Transactions on*, vol. 21, no. 2, pp. 504 – 511, june 2006.

[26] H. He, R. Xiong, X. Zhang, F. Sun, and J. Fan, "State-of-charge estimation of the lithium-ion battery using an adaptive extended kalman filter based on an improved thevenin model," *Vehicular Technology, IEEE Transactions on*, vol. 60, no. 4, pp. 1461 –1469, may 2011.

[27] H. Khalil, *Nonlinear systems*. Prentice Hall, NJ, 2002.

[28] J. Kassakian, M. Schlecht, and G. Verghese, *Principles of Power Electronics*. Addison-Wesley, 1991.

[29] S. Sirisukprasert, "The Modeling and Control of a Cascaded-Multilevel Converter-Based STATCOM," PhD Thesis, Virginia Tech, 2004.

[30] L. Guzzella and A. Sciarretta, *Vehicle Propulsion Systems*. Springer, 2005.

[31] M. Grant and S. Boyd, "CVX: Matlab software for disciplined convex programming, version 1.21," ../../cvx, Apr. 2011.

[32] ——, "Graph implementations for nonsmooth convex programs," in *Recent Advances in Learning and Control*, ser. Lecture Notes in Control and Information Sciences, V. Blondel, S. Boyd, and H. Kimura, Eds. Springer-Verlag Limited, 2008, pp. 95–110, http://stanford.edu/~boyd/graph_dcp.html.

[33] S. Boyd and L. Vandenberghe, *Convex Optimization*. Cambridge University Press, 2006.

[34] D. Andrea, *Battery Management Systems for Large Lithium Ion Battery Packs*, 1st ed. Artech House, 9 2010.

Paper 2

Feasibility Issues of using Three-Phase
Multilevel Converter based Cell Balancer in
Battery Management System for xEVs

Faisal Altaf, Lars Johannesson, Bo Egardt

Comment: The layout of this paper has been reformatted in order to comply with the rest of the thesis.

Feasibility Issues of using Three-Phase Multilevel Converter based Cell Balancer in Battery Management System for xEVs

Faisal Altaf, Lars Johannesson, Bo Egardt

Abstract

The use of a three-phase (3-ϕ) multilevel converter (MLC) as an integrated cell balancer and motor driver is investigated for 3-ϕ AC applications in EVs/HEVs/PHEVs. The paper analyzed an issue of additional battery losses caused by the flow of reactive and/or harmonic power from each power cell of the 3-ϕ MLC battery system. The paper also investigates the size of shunt capacitor required for compensation of the losses to acceptable level. This study concludes that the size of the required capacitor is too big for the vehicle application unless some other active compensation is used as well. Another practical way to employ the MLC as a cell balancer is to use it in a cascaded connection with the conventional 3-ϕ two-level voltage source inverter however it may not be a cost-effective solution either due to high component count.

1 Introduction

The battery pack in Hybrids (HEVs) and Electric Vehicles (EVs) is built from a large number of small cells connected in series and parallel to meet both the traction power demand and electric range requirement. The Depth-of-Discharge, see [1], and the cell temperature, see [2], are the two most important factors that determine the degradation of the battery cells. Hotter cells degrade more quickly than colder cells. Therefore, even a few overheated cells may result in shortening the lifetime of the whole battery pack. Hence, the battery management system should ideally be able to both balance the state-of-charge (SoC) of the cells and keep the temperature differences between the cells less than 5°C with a maximum temperature below 40°C, see [2]. With the purpose of transfering charge from cells having higher SoC to cells having lower SoC, there are several active and passive cell balancing schemes based on various topologies of switched capacitive and resistive circuits, see for example [3], and [4].

In recent years cascaded MLCs, see [5], have been discussed for the drive of the electric motor in HEVs, see [6] and [7]. The MLC consists of n cascaded H-bridges (HBs) with an isolated battery cell for each HB. The combination of an HB and a battery cell is here called a Power Cell (PC). The MLC, other than reducing the total harmonic distortion in the generated waveform for the electric machine, also offers an additional advantage of extra degree-of-freedom (DoF) to generate the load voltages. In most of these motor drive applications of the MLCs, the usual strategy is to use a phase shifted pulse width modulation technique to achieve the uniform use of cascaded cells, see [5].

In [8] the MLC is proposed as both a cell balancer and a drive for EV/HEV/PHEVs (xEVs) equipped with DC electric motors. The extra DoF of the MLC is used to achieve simultaneous thermal and SoC balancing among the battery cells. However, in almost all xEVs, a 3-ϕ AC machine is used to power the wheels. Therefore, in [9] it is proposed to use the MLC as a cell balancer for the 3-ϕ application. In the proposed configuration, the single-phase MLC is used as a dedicated cell balancer in the battery pack and is integrated with 3-ϕ TLI (Two-Level (voltage source) Inverter) in a way such that the dc-link of 3-ϕ TLI is supplied by the cascaded MLC. This configuration works very well as a cell balancer but the component cost is likely too high. This would partly be alleviated by using the 3-ϕ MLC to directly drive the 3-ϕ AC machine as proposed by [7].

This paper investigates the configuration proposed in [7], studying the practical consequences for the battery cells when using the 3-ϕ MLC to directly drive the 3-ϕ AC machine. The paper investigates in detail the reactive/harmonic power flow which leads to a high level dc-link ripple current causing significant additional ohmic losses in batteries. The extra losses increase the operating temperature which accelerates the capacity fading of batteries, see [10].

The main contributions of the current article are as follows: Issues of using 3-ϕ MLC as an integrated cell balancer and motor drive are thoroughly studied and analyzed; in order to characterize the losses and the size of compensating capacitor, the dc-link current is accurately computed using double Fourier series approach, see [11], [12], and [13]; the additional battery losses due to dc-link current ripple are computed and analyzed and the size of shunt-capacitor needed for the passive compensation is evaluated under normal operating conditions; and the results are compared to the case of 3-ϕ TLI.

The paper is organized as follows. Section 2 gives an overview of the basic function of single-phase MLC for DC loads. The problem description and the underlying assumptions for the analysis are given in section 3. The
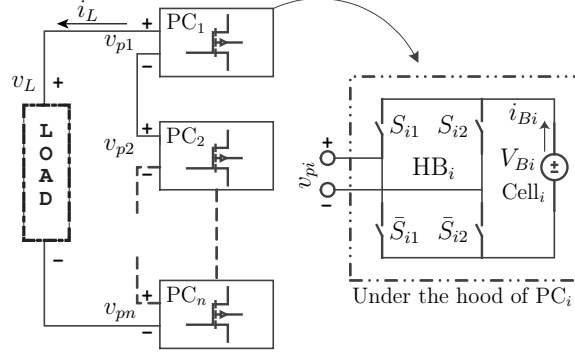
Figure 1: Block diagram of a single phase cascaded HB MLC.

dc-link current is computed based on double Fourier series approach in section 4. The capacitor sizing based on computed dc-link ripple current is done in section 5 and then the additional battery losses due to dc-link ripple current are computed in section 6. Finally the conclusions are drawn in Section 7.

2 Multi-level Converters

In this section, the single-phase MLC for a DC load is reviewed. In contrast to two-level converters, consisting of a single large battery pack connected with a single HB, the MLC consists of many series connected PCs where each PC contains an HB and the independent battery cell as shown in Figure 1. The HB is a switch mode dc-dc power converter, see [14], that produces a four-quadrant controllable dc output using four switches S_{i1}, S_{i2}, $\bar{S}_{i1}$, $\bar{S}_{i2}$ as shown in Figure 1. Therefore, depending on which switch pair is turned-on, three modes of operation can be defined for each PC_i. In *Mode–1* $v_{pi} > 0$, in *Mode–2* $v_{pi} < 0$ and in *Mode–3* $v_{pi} = 0$. To model these three modes of operation, let's define $s_{ij}(t) = 1$ for ON-State and $s_{ij}(t) = 0$ for OFF-State of switch S_{ij} where 'i' corresponds to PC_i and $j \in \{1, 2\}$. Now the switching function $s_i(t)$ for a PC_i (or $Cell_i$) can be defined by $s_i(t) = (s_{i1}(t) - s_{i2}(t)) \in \{1, -1, 0\}$ corresponding to *Mode–1*, *Mode–2* and *Mode–3* respectively. Thus all three modes of HB can be defined in terms of $s_i(t)$. The switching vector $s(t) = \begin{bmatrix} s_1(t) & s_2(t) & \cdots & s_n(t) \end{bmatrix}^T$ contains switching functions for all n PCs inside the MLC. Assuming the ideal switch behavior, the ohmic and switching losses can be ignored and, therefore, the input and output of HB, as shown in Figure 1, are related through the switching function $s_i(t)$. Thus, the current through $Cell_i$ is given by:

$$i_{Bi}(t) = s_i(t) i_L(t) \qquad (1)$$

where $i_L(t)$ is the load current. Note that due to the series connection, the same current i_L passes through each PC. However, the direction of current passing through the battery Cell$_i$ depends both on the selection of switches and the direction of load current i_L. Similarly the voltage output from each PC$_i$ is defined by $v_{pi}(t) = V_{Bi}(t)s_i(t)$ and hence the total voltage output from the MLC is given by $v_L = \sum_{i=1}^{n} v_{pi} = \sum_{i=1}^{n} V_{Bi}(t)\, s_i(t)$ with the MLC being able to generate $L = 2\,n + 1$ different voltage levels (v_L).

The MLC allows to independently switch ON/OFF each battery cell in a battery pack . This extra DoF opens up many intriguing control research problems which can be studied for various applications. In [8], the potential benefit of cell balancing using extra extra DoF of single-phase MLC has been evaluated for DC loads by formulating it as a constrained convex optimization problem. The results show that the optimal control policy, exploiting the full DoF of MLC, gives significant benefit in terms of reduction in temperature and SoC deviations, especially under parameter variations, compared to uniformly using all the cells.

Table 1: Nomenclature and List of Symbols

Symbols	Definition
n, PC$_i$	Number of Power Cells, Power Cell i
F_p, ESR	Power Factor, Effective Series Resistance
$s_i(t)$	Switching function of PC$_i$
$v_x(t)$	Instant. voltage of phase x where $x = a, b,$ or c
$i_x(t)$	Instant. current in phase $x = a, b,$ or c
θ	Phase angle between $v_x(t)$ and $i_x(t)$ in phase x
ω_o	Fundamental frequency of output AC variables
ω_m	Mechanical (angular) speed of AC machine
n_p	Number of pole pairs in AC machine: $n_p = \omega_o/\omega_m$
ω_s/ω_c	Switching/Carrier frequency where $\omega_s = \omega_c$
V_r	Amplitude of reference modulating signal in PWM
V_c	Amplitude of carrier signal in PWM
M_o	Modulation Index in PWM: $M_o = V_r/V_c$

3   Problem Description

The 3-ϕ MLC driving 3-ϕ balanced load is shown in Figure 2 for case of $n = 2$. It has been noted that, for the case of 3-ϕ AC machine, which acts as inductive load with lagging power factor, the 3-ϕ MLC has to supply
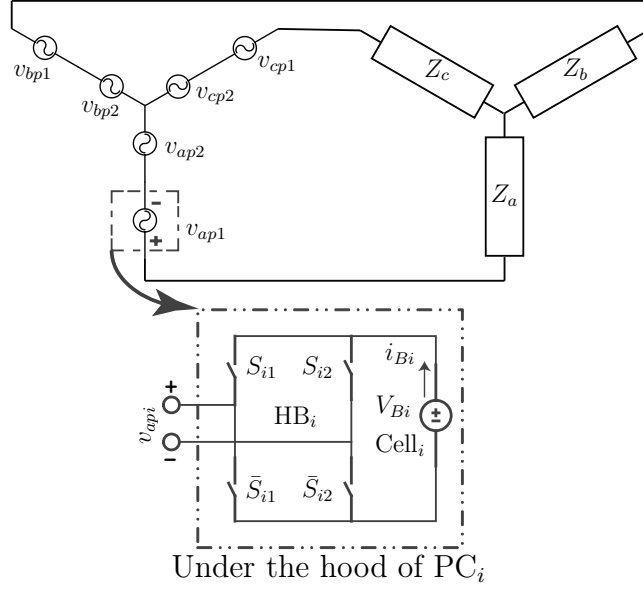
Figure 2: 3-ϕ MLC for $n = 2$.

the bidirectional fluctuating power from each PC. Though one of the major components of this fluctuating power from each PC is the reactive power whose magnitude largely depends on the power factor angle θ however there is a large contributions due to switching harmonics as well. In particular, the flow of reactive power and the switching action generates a large dc-link (i.e. DC input side of the HB) ripple current at 2nd order baseband harmonic frequency. Ideally, to minimize losses, a constant dc current should flow through the battery cell. However, the battery cells in the MLC are cascaded in series and connected across dc-link in each phase. Thus, in the absence of compensation, the battery cells at each dc-link get exposed to this very high ripple current which incurs significant additional losses on the battery cells and thus increases the battery temperature. The battery operation at elevated temperature has detrimental effect on the battery lifetime and therefore the large ripple current needs to be compensated by using a dc-link capacitor in parallel with battery. In contrast to 3-ϕ MLC, the balanced 3-ϕ TLI provides almost constant power under ideal conditions, see [15], [14]. Though the reactive power also flows in 3-ϕ TLI, the batteries do not see this reactive power by virtue of the topology and the symmetrical fast switching in three legs. Under ideal conditions almost all the reactive power instantaneously shuffles between three phases and hence never flows back to the battery pack. Thus, compared to 3-ϕ TLI, the 3-ϕ MLC, as an integrated cell balancer and motor driver, faces some serious issues which need to be carefully analyzed to check its feasibility for xEVs.

3.1   Assumptions:

The following assumptions are outlined here which will be employed later to calculate the dc-link current harmonics:

Assumption 2.1. Distortion is present only in voltage where- as the output load current in all phases is assumed perfectly sinusoidal with frequency ω_o and power factor angle θ i.e.

$$i_a(t) = \sqrt{2}I_a \cos(\omega_o t + \theta) \tag{2}$$

Assumption 2.2. Three-phase source (3-ϕ MLC or 3-ϕ TLI) is balanced i.e. all three phases have same rms voltage V and frequency ω_o. Moreover three phases are symmetrical i.e. they are shifted exactly by 120° w.r.t. each other and 3-ϕ source has counterclockwise rotating positive-sequence of phases a, b, and c, see [16].

Assumption 2.3. Inverters are driving 3-ϕ balanced inductive load i.e. all three loads connected in Y or Δ configuration have same impedance. It implies that there is no asymmetrical current flowing in the 3-ϕ circuit and thus all phase currents are equal i.e. $I_a = I_b = I_c$.

Assumption 2.4. The switching (or carrier) frequency f_s is infinite. Under this assumption, all the carrier harmonics and their sidebands can be easily filtered, using a very small capacitor, and thus can be neglected. See section 5.

Assumption 2.5. We assume Thevenin model for the battery Cell$_i$ with internal resistance $R_{si} = 6.3\,m\Omega$.

Assumption 2.6. It is assumed that naturally sampled sine-triangle PWM (SPWM) is used as a modulation strategy for switches. The SPWM uses a sinusoid, having amplitude V_r, as a reference modulating signal and a high frequency triangular waveform, having amplitude V_c, as a carrier signal. These two signals are compared to generate the PWM, see [12] for details.

Assumption 2.7. The permanent magnet synchronous machine (PMSM) with two pole pairs is assumed in this study i.e. $n_p = 2$. Thus the mechanical speed of the machine and the fed electrical frequency are related by $\omega_o = 2\omega_m$. In this study, the nominal operating speed of $\omega_m = 6$krpm is assumed for PMSM, see [17].

Assumption 2.8. The dc-link capacitor is assumed to be non-ideal i.e. it has effective series resistance (ESR) R_{ci}. This assumption is made to stay close to reality in terms of compensation potential of dc-link capacitor.

4 DC-Link Current Calculation Using Double Fourier Series Approach

The dc-link ripple current is the cause for additional battery losses. Though, the harmonic content of dc-link current can also be determined using Fast Fourier Transform analysis of time-varying switched waveforms of the *simulated* circuit but it is computationally very expensive especially for PWM systems with a high switching frequency. Thus, in this section, to exactly characterize the losses the dc-link current is *analytically* computed for both 3-ϕ MLC and 3-ϕ TLI using double Fourier series approach, see [13], and [12] for details. In high frequency PWM power converters, the dc-link current is normally a product of a switching function and the load current as shown, for example, in (2) for MLC. It is generally quite tedious to precisely determine analytically the complex waveform of this dc-link current. The determination of current waveform can be done more easily in frequency domain. If frequency spectrums of $s_{i1}(t)$, $s_{i2}(t)$, and $i_a(t)$ are known then convolution can be performed in frequency domain and then inverse fourier transform is taken to recover the time-waveform of $i_{dci}(t)$.

The spectral analysis of PWM processes is extensively researched in recent years, see [12], [11], and the frequency spectrum of commonly used switching functions is now well known from PWM theory. The switching waveform generated by PWM process is not generally periodic and is normally a function of two other periodic time-waveforms so the machinery of double Fourier series, see [13], is used to analyze the harmonic content of this complex waveform. The general solution for any switching function $s_{ij}(t)$ of any switched phase-leg[1] 'j' is given by, see [11]

$$
\begin{aligned}
s_{ij}(t) = {} & \frac{A_{00}}{2} + \sum_{l=1}^{\infty} \left[A_{0l} \cos(ly) + B_{0l} \sin(ly) \right] \\
& + \sum_{k=1}^{\infty} \left[A_{k0} \cos(kx) + B_{k0} \sin(kx) \right] \\
& + \sum_{k=1}^{\infty} \sum_{\substack{l=-\infty \\ l \neq 0}}^{\infty} \left[A_{kl} \cos(kx + ly) + B_{kl} \sin(kx + ly) \right]
\end{aligned}
\tag{3}
$$

---

[1] It refers to a leg with a switch-pair inside 3-ϕ MLC or 3-ϕ TLI. It should not be confused with the phase of 3-ϕ AC system.

where A_{kl} and B_{kl} are Fourier coefficients given by

$$A_{kl} = \frac{1}{2\pi^2} \int_{-\pi}^{\pi} \int_{-\pi}^{\pi} s_{ij}(t) \cos(kx + ly) \mathrm{d}x \mathrm{d}y \tag{4a}$$

$$B_{kl} = \frac{1}{2\pi^2} \int_{-\pi}^{\pi} \int_{-\pi}^{\pi} s_{ij}(t) \sin(kx + ly) \mathrm{d}x \mathrm{d}y \tag{4b}$$

and $x = \omega_c t + \theta_{ci}$, $y = \omega_o t + \theta_{oj}$ where ω_c is the carrier frequency, ω_o is the output fundamental frequency, θ_{ci} is the carrier phase angle for PC_i and θ_{oj} is the phase angle of the fundamental sinusoidal waveform used as a reference in PWM generation for each phase-leg 'j'.

4.1 Double Fourier Series of SPWM

In this study we use SPWM (cf. assumption-2.6) for switching the switches. The double Fourier series representation of SPWM is now well known and is given by, see [12], [11]

$$\begin{aligned}
s_{ij}(t) = \frac{1}{2} &+ \frac{M_o}{2} \cos(y) + \frac{2}{\pi} \sum_{k=1}^{\infty} \left[\frac{1}{k} J_0\left(k\frac{\pi}{2}M_o\right) \sin\left(k\frac{\pi}{2}\right) \cos(kx) \right] \\
&+ \frac{2}{\pi} \sum_{k=1}^{\infty} \sum_{\substack{l=-\infty \\ l \neq 0}}^{\infty} \left[\frac{1}{k} J_l\left(k\frac{\pi}{2}M_o\right) \sin\left([k+l]\frac{\pi}{2}\right) \cos(kx + ly) \right]
\end{aligned} \tag{5}$$

where $J_l(\xi)$ denotes a Bessel function of the first kind with order l and argument ξ. The angle

$$\theta_{ci} = \frac{2\pi(i-1)}{(n-1)}, \quad \forall i \in \{1, 2, \cdots, n-1\} \tag{6}$$

is the carrier phase angle, θ_{oj} is the phase angle of the fundamental sinusoidal waveform used as reference in PWM generation for each phase-leg, and M_o is its modulation index. The frequency of this waveform is equal to that of desired fundamental output and the value of phase-angle θ_{oj} normally depends on the number of phase-legs in the PC. Now comparing (5) with (3) we get the following Fourier coefficients for SPWM:

$$A_{00} = 1, \; A_{01} = \frac{M_o}{2} \text{ and } A_{0l} = 0, \; \forall l > 1,$$

$$A_{kl} = \left[\frac{2}{k\pi} J_l\left(k\frac{\pi}{2}M_o\right) \sin\left([k+l]\frac{\pi}{2}\right) \right], \forall k \in \mathbb{N}^+, \; \forall l \in \mathbb{Z},$$

$$B_{kl} = 0, \; \forall k \in \mathbb{N}, \; \forall l \in \mathbb{Z} \tag{7}$$

4.2 3-ϕ MLC: DC-Link Current in a Power Cell

In this subsection, the dc-link current in three-level PC$_i$ of 3-ϕ MLC is calculated. Only phase-a of 3-ϕ MLC is considered. Due to stated assumptions, the result will be same for other phases. Let us now consider the dc-link current, in PC$_i$ of phase-a, given by

$$i_{dci}(t) = s_i(t)i_a(t) = [s_{i1}(t) - s_{i2}(t)]\, i_a(t) \tag{8}$$

where $s_{i1}(t)$ and $s_{i2}(t)$ are SPWM switching function for phase-leg-1 and phase-leg-2 and $i_a(t)$ is the sinusoidal load current, as defined in (2), for phase-a of 3-ϕ MLC. The phase switching functions are given by (5) with angles θ_{oj} defined by

$$\theta_{oj} = \begin{cases} 0 & \text{if } j = 1 \\ -\pi & \text{if } j = 2 \end{cases} \tag{9}$$

Recall that in context of MLC, $s_i(t)$ is considered as a switching function for whole PC$_i$. In the following, the expression for $s_i(t)$ will be derived. For notational convenience here we assume $\theta_{ci} = 0$ but it will not change the form of final result.

Phase-leg 1:

In this case $\theta_{o1} = 0$. Now plugging in the values of x and y in (5) and doing some simple manipulations, (5) can be rewritten as follows

$$
\begin{aligned}
s_{i1}(t) = {} & \frac{1}{2} + \frac{M_o}{2}\cos(\omega_o t) \\
& + \frac{2}{\pi}\sum_{k=1}^{\infty}\left[\frac{1}{k}J_0\left(k\frac{\pi}{2}M_o\right)\sin\left(k\frac{\pi}{2}\right)\cos\left(k\omega_c t\right)\right] \\
& + \frac{2}{\pi}\sum_{k=1}^{\infty}\sum_{\substack{l=-\infty \\ l\neq 0 \\ l=even}}^{\infty}\left[\frac{1}{k}J_l\left(k\frac{\pi}{2}M_o\right)\sin\left([k+l]\frac{\pi}{2}\right)\cos\left(k\omega_c t + l\omega_0 t\right)\right] \\
& + \frac{2}{\pi}\sum_{k=1}^{\infty}\sum_{\substack{l=-\infty \\ l\neq 0 \\ l=odd}}^{\infty}\left[\frac{1}{k}J_l\left(k\frac{\pi}{2}M_o\right)\sin\left([k+l]\frac{\pi}{2}\right)\cos\left(k\omega_c t + l\omega_0 t\right)\right]
\end{aligned} \tag{10}
$$

Phase-leg 2:

In this case $\theta_{o1} = -\pi$ is used in (5) and then using the fact that $\cos(\alpha - l\pi) = \cos(\alpha)$, if l is even and $\cos(\alpha - l\pi) = -\cos(\alpha)$, if l is odd, we get the fol-

lowing double Fourier series representation of SPWM for phase-leg 2

$$
\begin{aligned}
s_{i2}(t) = {} & \frac{1}{2} - \frac{M_o}{2}\cos(\omega_o t) \\
& + \frac{2}{\pi}\sum_{k=1}^{\infty}\left[\frac{1}{k}J_0\left(k\frac{\pi}{2}M_o\right)\sin\left(k\frac{\pi}{2}\right)\cos\left(k\omega_c t\right)\right] \\
& + \frac{2}{\pi}\sum_{k=1}^{\infty}\sum_{\substack{l=-\infty \\ l\neq 0 \\ l=even}}^{\infty}\left[\frac{1}{k}J_l\left(k\frac{\pi}{2}M_o\right)\sin\left([k+l]\frac{\pi}{2}\right)\cos\left(k\omega_c t + l\omega_0 t\right)\right] \\
& - \frac{2}{\pi}\sum_{k=1}^{\infty}\sum_{\substack{l=-\infty \\ l\neq 0 \\ l=odd}}^{\infty}\left[\frac{1}{k}J_l\left(k\frac{\pi}{2}M_o\right)\sin\left([k+l]\frac{\pi}{2}\right)\cos\left(k\omega_c t + l\omega_0 t\right)\right]
\end{aligned}
\tag{11}
$$

Now using (10) and (11), the overall switching function s_i of PC_i is given by

$$
\begin{aligned}
s_i(t) = {} & s_{i1}(t) - s_{i2}(t) = \\
& M_o\cos(\omega_o t) + \frac{4}{\pi}\sum_{k=1}^{\infty}\sum_{\substack{l=-\infty \\ l\neq 0 \\ l=odd}}^{\infty}\left[\frac{1}{k}J_l\left(k\frac{\pi}{2}M_o\right)\sin\left([k+l]\frac{\pi}{2}\right)\cos\left(k\omega_c t + l\omega_0 t\right)\right]
\end{aligned}
$$

$$\tag{12}$$

Finally the dc-link current in PC_i can be computed by direct multiplication of (2) and (12) which gives

$$
\begin{aligned}
i_{dci}(t) = {} & \frac{M_o I_a}{\sqrt{2}}\cos(\theta) + \frac{M_o I_a}{\sqrt{2}}\cos(2\omega_o t + \theta) \\
& + \left[\frac{4}{\pi}\sum_{k=1}^{\infty}\sum_{\substack{l=-\infty \\ l\neq 0 \\ l=odd}}^{\infty}\left[\frac{1}{k}J_l\left(k\frac{\pi}{2}M_o\right)\sin\left([k+l]\frac{\pi}{2}\right)\cos\left(k\omega_c t + l\omega_0 t\right)\right]\right] \times \\
& \times \sqrt{2}I_a\cos(\omega_o t + \theta)
\end{aligned}
\tag{13}
$$

Thus, it is obvious from (13) that dc-link current in any PC_i of 3-ϕ MLC consists of a dc component, large 2nd baseband harmonic, and all odd carrier sidebands including triplen sideband harmonics.

4.3   3-ϕ TLI: DC-Link Current Harmonics

The 3-ϕ TLI consists of only one PC with six switches arranged in three phase-legs. Since there is only one PC so subscript 'i' will be dropped in the following mathematical development. The total dc-link current in

any 3-ϕ TLI is given by adding dc-link current contributions from all three phase-legs as follows

$$i_{dc} = i_{dc1}(t) + i_{dc2}(t) + i_{dc3}(t) \tag{14}$$

According to [11], the dc-link current contribution from any phase-leg 'j' for 3-ϕ TLI is given by

$$i_{dcj}(t) = \frac{\hat{A}_{00}}{2} + \sum_{l=1}^{\infty} \left[\hat{A}_{0l} \cos(l\omega_0 t + l\theta_{oj}) + \hat{B}_{0l} \sin(l\omega_o t + l\theta_{oj}) \right]$$

$$+ \sum_{k=1}^{\infty} \left[\hat{A}_{k0} \cos(k\omega_c t) + \hat{B}_{k0} \sin(k\omega_c t) \right] \tag{15}$$

$$+ \sum_{k=1}^{\infty} \sum_{\substack{l=-\infty \\ l \neq 0}}^{\infty} \left[\hat{A}_{kl} \cos \left((k\omega_c t + l\omega_0 t) + l\theta_{oj} \right) + \hat{B}_{kl} \sin \left((k\omega_c t + l\omega_0 t) + l\theta_{oj} \right) \right]$$

where $\theta_{oj} = 0$ for $j = 1$ (phase-a), $\theta_{oj} = -\frac{2\pi}{3}$ for $j = 2$ (phase-b), $\theta_{oj} = \frac{2\pi}{3}$ for $j = 3$ (phase-c), and the Fourier coefficients for all three phases are given by:

$$\hat{A}_{00} = \frac{M_o I_j}{4} \cos(\theta), \quad \hat{A}_{0l} = \hat{B}_{0l} = 0, \forall l > 2, \tag{16a}$$

$$\hat{A}_{01} = \frac{1}{2} I_j \cos(\theta), \quad \hat{B}_{01} = -\frac{1}{2} I_j \sin(\theta), \tag{16b}$$

$$\hat{A}_{02} = \frac{M_o}{4} I_j \cos(\theta), \quad \hat{B}_{02} = -\frac{M_o}{4} I_j \sin(\theta), \tag{16c}$$

$$\hat{A}_{kl} = \frac{I_j}{k\pi} \cos \left([k+l] \frac{\pi}{2} \right) \cos(\theta) \left[J_{l+1}(\cdot) - J_{l-1}(\cdot) \right], \forall k \in \mathbb{N}^+, \forall l \in \mathbb{Z}, \tag{16d}$$

$$\hat{B}_{kl} = \frac{I_j}{k\pi} \cos \left([k+l] \frac{\pi}{2} \right) \sin(\theta) \left[J_{l+1}(\cdot) + J_{l-1}(\cdot) \right], \forall k \in \mathbb{N}^+, \forall l \in \mathbb{Z} \tag{16e}$$

Now using above coefficients, the expression (15) for the jth phase-leg switched current gets simplified to

$$i_{dcj}(t) = \frac{M_o I_j}{8} \cos(\theta) + \frac{I_j}{2} \cos(\theta) \cos(\omega_0 t + \theta_{oj}) - \frac{I_j}{2} \sin(\theta) \sin(\omega_o t + \theta_{oj})$$

$$+ \frac{M_o I_j}{4} \cos(\theta) \cos(2\omega_0 t + 2\theta_{oj}) - \frac{M_o I_j}{4} \sin(\theta) \sin(2\omega_o t + 2\theta_{oj})$$

$$+ \sum_{k=1}^{\infty} \left[\hat{A}_{k0} \cos(k\omega_c t) + \hat{B}_{k0} \sin(k\omega_c t) \right] \tag{17}$$

$$+ \sum_{k=1}^{\infty} \sum_{\substack{l=-\infty \\ l \neq 0}}^{\infty} \left[\hat{A}_{kl} \cos \left((k\omega_c t + l\omega_0 t) + l\theta_{oj} \right) + \hat{B}_{kl} \sin \left((k\omega_c t + l\omega_0 t) + l\theta_{oj} \right) \right]$$

Using (17) for $j = 1, 2, 3$ in (14) gives a messy expression but it can be simplified by first using assumption-2.3 and then identifying the following two trigonometric identities.

$$
\begin{aligned}
\left[\cos(x) + \cos(x - l\frac{2\pi}{3}) + \cos(x + l\frac{2\pi}{3})\right] &= 0, \\
\left[\sin(x) + \sin(x - l\frac{2\pi}{3}) + \sin(x + l\frac{2\pi}{3})\right] &= 0, \\
\forall x, \quad \forall l = \{\pm 1, \pm 2, \pm 4, \pm 5, \pm 7, \cdots\}
\end{aligned}
\tag{18}
$$

Note that the above two identities are true for any angle x where $x \in \{\omega_o t, \; 2\omega_o t, \; (k\omega_c + l\omega_o)t\}$ here. Applying these two identities, the expression for total dc-link current is simplified to (19)

$$
\begin{aligned}
i_{dc} &= \frac{3M_o I_a}{8} \cos(\theta) + 3 \sum_{k=1}^{\infty} \left[\hat{A}_{k0} \cos(k\omega_c t) + \hat{B}_{k0} \sin(k\omega_c t)\right] \\
&+ 3 \sum_{k=1}^{\infty} \sum_{l \in \mathcal{L}} \left[\hat{A}_{kl} \cos(k\omega_c t + l\omega_o t) + \hat{B}_{kl} \sin(k\omega_c t + l\omega_o t)\right]
\end{aligned}
\tag{19}
$$

where $\mathcal{L} = \{-\infty, \cdots, -6, -3, 3, 6, \cdots, \infty\}$. From the expression (19) it is quite obvious that the dc-link current in 3-ϕ TLI consists of dc-component, carrier harmonics and triplen sidebands. Thus in 3-ϕ TLI, the fundamental, baseband harmonics including second, and the non-triplen harmonics are all cancelled. Thus compared to MLC the harmonic content on the dc-side of 3-ϕ TLI is much less which means the current ripple is very low in 3-ϕ TLI compared to that in each PC$_i$ of 3-ϕ MLC.

5 Dc-link Ripple Current Compensation: Shunt Capacitor Sizing

The objective is to reduce extra losses in the battery cell due to flow of ripple current. Thus, in order to achieve this objective, a shunt-capacitor with appropriate value need to be connected across Cell$_i$ in the dc-link. The capacitor acts as a compensator/filter for dc-link ripple current. In this section, the size of capacitor is determined for both 3-ϕ TLI and for each PC$_i$ in 3-ϕ MLC.

5.1 DC-Link Capacitor Size for each PC$_i$ in 3-ϕ MLC

The size of the dc-link capacitor depends either on the amount of ripple current that is shunted by the capacitor or on the amount of energy it has
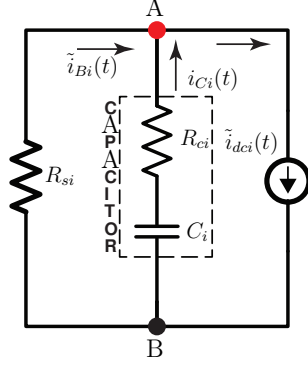
Figure 3: DC-Link ac equivalent circuit.

to store over one cycle of fundamental frequency. With infinite capacitance value, the whole oscillating power (including the reactive power) will be supplied by the capacitor C_i and the battery will only supply the active power. Since infinite capacitance is practically infeasible, some tolerable level of current/voltage ripple is allowed to determine the finite capacitance value. The ripple in the dc-link voltage appears due to the oscillating dc-link current and the battery internal resistance. The amplitude of voltage ripple depends on the amplitude of the oscillating component of the dc-link current $i_{Bi}(t)$ and the value of series resistance R_{si}. To determine these ripple variables, the dc-link ac equivalent circuit is drawn as shown in Figure 3. In the model, the capacitor is assumed to be non-ideal i.e. it has effective series resistance (ESR). Now using phasor analysis and applying Kirchhoff's current law at node-A, the ac ripple current in the battery is obtained as

$$\tilde{I}_{Bi}(\omega) = \left(\frac{1 + sR_{ci}C_i}{1 + sR_{ci}C_i + sR_{si}C_i} \right) \tilde{I}_{dci}(\omega) \tag{20}$$

where $s = j\omega$ and $\tilde{I}_{dci}(\omega)$ is the pure ac-component of the dc-link current given by (13). Under the assumption of infinite switching frequency, all the carrier and sideband harmonics can be easily filtered, using a very small capacitor, and thus can be neglected. Therefore, the equation (13) is simplified to

$$i_{dci}(t) \cong \underbrace{\frac{M_oI_a}{\sqrt{2}} \cos(\theta)}_{I_{dci}} + \underbrace{\frac{M_oI_a}{\sqrt{2}} \cos(2\omega_ot + \theta)}_{\tilde{i}_{dci}(t)} \tag{21}$$

where $w_o = 2\omega_m$ is the electrical angular frequency being fed to electrical machine. From (21) it is quite evident that the dc-link current at the PC_i input consists of two components: the pure dc-component I_{dci} and the

pure ac-component $\tilde{i}_{dci}(t)$ at second baseband harmonic frequency. Note that the amplitude of this ac-component is equal to dc-component. Using this approximation, the expression (20) can be easily evaluated for peak magnitude of the battery ripple current as given below

$$\tilde{I}_{Bim}(\omega) = \left(\sqrt{\frac{1 + \omega^2 R_{ci}^2 C_i^2}{1 + \omega^2 (R_{ci}C_i + R_{si}C_i)^2}} \right) \frac{\sqrt{2}M_o I_a}{2} \tag{22}$$

where $\omega = 2\omega_o = 4\omega_m$ is the dc-link ripple frequency. Note that in the absence of dc-link capacitor, $i_{Bi}(t) = i_{dci}(t)$. Only the dc-component transfers the real power whereas the ac-component in the absence of capacitor incurs extra losses in the internal resistance of the battery. It is well known that this ac ripple current degrades the battery life-time, see [18]. Thus it is quite important to take this thing into consideration while designing the dc-link side of each PC_i. Ideally battery should provide only the dc-component and the ac ripple should be taken by capacitor. However, the battery manufacturer normally allows certain maximum tolerable level of ripple current above which battery's life-time is significantly degraded. It is normally recommended to limit the ripple current below 10% of the rated current capacity of a battery cell, see [18]. Thus, for a graphical illustration it is more useful to show *battery ripple current peak magnitude per unit dc current component* as given below

$$\delta \tilde{I}_{Bim}(\omega) = \frac{\tilde{I}_{Bim}(\omega)}{\bar{I}_{Bi}} = \left(\sqrt{\frac{1 + \omega^2 R_{ci}^2 C_i^2}{1 + \omega^2 (R_{ci}C_i + R_{si}C_i)^2}} \right) \frac{1}{\cos(\theta)} \tag{23}$$

where $\bar{I}_{Bi} = I_{dci} = \frac{M_o I_a}{\sqrt{2}} \cos(\theta)$ is the dc component of dc-link current provided by the battery. The above relation clearly shows that the battery ripple current depends not only on capacitor size, capacitor effective series resistance (ESR) but also on the frequency ω of the ripple current component under consideration. For sake of completeness, other ripple variables are also determined as given below. The ripple current through the capacitor is given by

$$I_{Ci}(s) = \left(\frac{-sR_{si}C_i}{1 + s(R_{ci}C_i + R_{si}C_i)} \right) \tilde{I}_{dci}(s) \tag{24}$$

Similarly, the ripple voltage across capacitor is given by

$$V_{Ci}(s) = \left(\frac{R_{si}}{1 + s(R_{ci}C_i + R_{si}C_i)} \right) \tilde{I}_{dci}(s) \tag{25}$$

and the ac ripple in the dc-link voltage is given by

$$\tilde{V}_{dci}(s) = \left(\frac{1 + sR_{ci}C_i}{1 + s(R_{ci}C_i + R_{si}C_i)} \right) \tilde{I}_{dci}(s) R_{si} \tag{26}$$
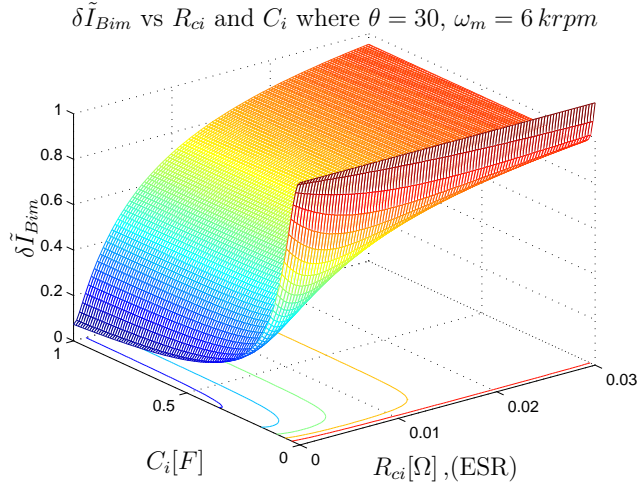
Figure 4: *Peak magnitude of battery ripple current per unit dc current* versus C_i and R_{ci}.

where $\tilde{V}_{dci}(s) = \tilde{V}_{AB}(s)$. Note that all the ripple signals involved here have frequency $\omega = 2 \cdot \omega_o$. Figure 4 shows the plot of $\delta\tilde{I}_{Bim}$ versus C_i and R_{ci} for nominal machine operation @$f_m = 100\,\mathrm{Hz}(\omega_m = 6\,\mathrm{krpm})$ which implies that the ripple frequency $f = 4f_m = 400\,\mathrm{Hz}$. All other parameters are assumed as fixed i.e. $\theta = 30°$, $M_o = 0.9$, and $R_{si} = 6.3\,\mathrm{m\Omega}$. This plot clearly shows that to achieve $\delta\tilde{I}_{Bim} < 0.1$, very large value $(> 1F)$ of capacitor with significantly low ESR value will be needed. The idea of the required capacitor size can be perceived by the size $90 \times 150\,[mm]\,(D \times L)$ of a typical $10\,mF, 350\,V$ aluminium capacitor.

5.2 Capacitor Size for 3-ϕ TLI

Under ideal conditions, i.e. infinite switching frequency, balanced linear load with harmonic free ac voltages and currents, (cf. assumptions), all the carrier and sideband harmonics can be neglected and the dc-link current given by equation (19) can then be approximated by

$$i_{dc}(t) \approx \frac{3M_oI_a}{8}\cos(\theta) \tag{27}$$

The above equation shows that the dc-link current has only pure dc component and there is no time-varying component of power output exactly like in the case of ideal 3-ϕ ac systems. Thus, for ideal 3-ϕ TLI no dc-link compensation capacitor is needed.

Remark 2.1. *Note that under non-ideal conditions i.e. when harmonics are present and/or switching frequency is finite then the dc-link current will*

contain harmonics and thus there will be a time-varying power component. However, the dc-link current harmonics in this case will be present around switching frequency f_s which is much higher than the fundamental ac frequency f_o. In this case, the reactive power will shuffle from one phase to another phase @f_s. Thus even under non-ideal conditions, the capacitor has to deliver time varying power for a very short time interval compared to the case of dc-link capacitor in PC_i of MLC. Thus the capacitor has to store very small amount of energy and consequently the size will be very small comparatively. This is the main advantage of 3-ϕ TLI.

6 Additional Battery Losses in 3-ϕ MLC

In this section, the additional power loss at the battery due to ripple current is calculated as

$$P_{lBqi} = \tilde{I}_{Bir}^2 R_{si} \tag{28}$$

where $\tilde{I}_{Bir}$ is the rms value of the battery ripple current given by

$$\tilde{I}_{Bir} = \left(\sqrt{\frac{1 + \omega^2 R_{ci}^2 C_i^2}{1 + \omega^2 (R_{ci}C_i + R_{si}C_i)^2}} \right) \frac{M_o I_a}{2} \tag{29}$$

Thus the power loss at the battery Cell$_i$, caused by the flow of ripple current $\tilde{i}_{Bi}(t)$, is given by

$$P_{lBqi} = \left(\frac{1 + \omega^2 R_{ci}^2 C_i^2}{1 + \omega^2 (R_{ci}C_i + R_{si}C_i)^2} \right) \frac{R_{si} M_o^2 I_a^2}{4} \tag{30}$$

Similarly, the power loss at the battery Cell$_i$ due to the flow of dc current component $\bar{I}_{Bi}$ corresponding to real power is given by

$$P_{lBai} = \bar{I}_{Bi}^2 R_{si} = \left(\frac{R_{si} M_o^2 I_a^2}{2} \right) \cos^2(\theta) \tag{31}$$

Now for graphical illustration, the *ripple power loss per unit real power loss* is computed

$$\delta P_{lBqi} = \frac{P_{lBqi}}{P_{lBai}} = \left(\frac{1 + \omega^2 R_{ci}^2 C_i^2}{1 + \omega^2 (R_{ci}C_i + R_{si}C_i)^2} \right) \frac{1}{2\cos^2(\theta)} \tag{32}$$

Note that the above relation is only valid for $R_{si} \neq 0$. The expression (32) shows that in the absence of dc-link compensation capacitor ($C_i = 0$), the additional power loss in the battery cell explicitly depends on the power factor $F_p = \cos(\theta)$ i.e.

$$\delta P_{lBqi}^{uc} = \frac{1}{2\cos^2(\theta)} = \frac{1}{2F_p^2} \tag{33}$$

The last relation (33) shows that for the uncompensated case as

$$F_p \to 0 \Rightarrow \delta P_{lBqi}^{uc} \to \infty \qquad (34)$$

It is now quite obvious that for low power factor operation, battery cells will see very high additional losses in the absence of a dc-link compensation capacitor. Thus, for sake of saving batteries from additional losses, the dc-link compensation capacitor is unavoidable. In the following, we will use equation (32) and graphically illustrate the effect of various factors on the losses.

6.1   Effect of C_i and R_{ci} (ESR)

In figure 2.5(a), the per unit ripple power loss δP_{lBqi} is plotted versus C_i and R_{ci} for fixed power factor angle $\theta = 30°$. It is assumed that electric machine is operating at the fixed nominal speed of $\omega_m = 6krpm$. Under these conditions, for $C_i = 0$, the battery cell will see almost 66% additional losses. The figure shows that for any fixed value of capacitor, increasing ESR will significantly increase the losses. The figure also shows that just choosing a bigger capacitor without taking ESR into consideration may not help to reduce the losses. Both capacitance and ESR value are equally important and thus capacitor must be selected properly considering both parameters. For example, to compensate for the additional losses under stated conditions, we have to use here at least $0.5\,F$ capacitor with very low ESR value ($R_{ci} \le 1\,m\Omega$).

6.2   Effect of C_i and Power Factor (F_p) Angle θ

The figures 2.5(b) and 2.5(c) show variation in δP_{lBqi} as a function of C_i and power factor angle θ where it is assumed that $R_{ci} = 10\,m\Omega$ and the electric machine is operating at the fixed nominal speed of $\omega_m = 6krpm$. The figure 2.5(b) shows that for $F_p = 0.5$ and $C_i = 10\,mF$, the battery will see almost 182% additional losses. Similarly figure 2.5(c) shows that for $F_p = 0.2$ and $C_i = 10\,mF$, the battery will see 11 times more losses. These figures show that for low power factor operation ($F_p < 0.7, \ (\theta > 45°)$), the additional battery losses due to ripple current will be significantly high even when using compensation capacitor with $C_i = 10\,mF$ and $R_{ci} = 10\,m\Omega$. These figures also show that even for unity power factor, battery cells will see 50% more losses despite using $10\,mF$ capacitor with $10\,m\Omega$ ESR.

Thus, the large dc-link ripple current in each PC_i of 3-ϕ MLC causes significant additional heating that results in rise of operating temperature of cells which is well known to have a detrimental impact on a battery lifetime.
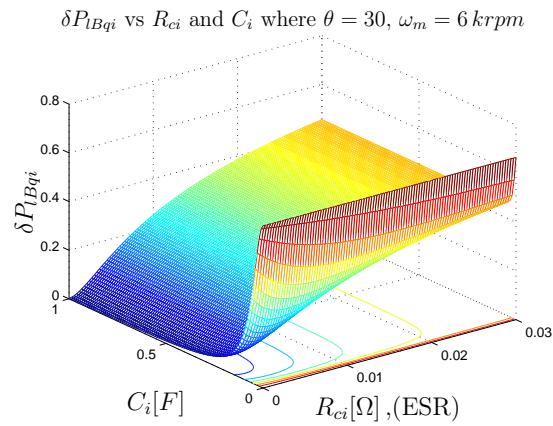
(a) *Ripple power loss δP_{lBqi} versus C_i and R_{ci} for constant power factor angle $\theta = 30°$.*
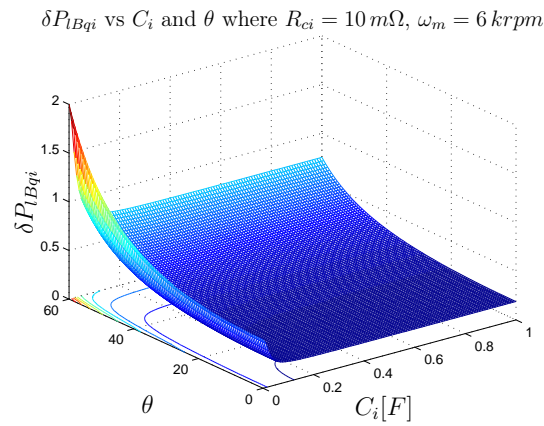
(b) *Per unit ripple power loss δP_{lBqi} versus C_i and power factor angle $\theta \in \{0, 60°\}$. Here it is assumed that $R_{ci} = 10\,m\Omega$.*
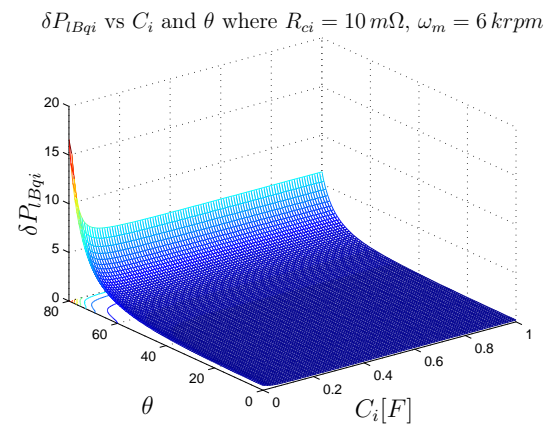
(c) *Per unit ripple power loss δP_{lBqi} versus C_i and power factor angle $\theta \in \{0, 80°\}$. Here it is assumed that $R_{ci} = 10\,m\Omega$.*

Figure 5: Per unit power loss due to ripple current and effects of various factors on the losses.

6.3 Capacitor Size Example

Let us assume that electric machine is operating at $\omega_m = 6krpm$ with power factor $F_p = 0.9$ and $R_{si} = 6.3\,m\Omega$. The objective is to reduce additional losses δP_{lBqi} below 10%. Now using equation (32), it is easy to verify that the compensation capacitor with following specifications will be needed inside each PC$_i$ of 3-ϕ MLC to achieve the objective:

$$C_i = 132\,mF, \quad R_{ci} = 1\,m\Omega \tag{35}$$

Thus, all the figures and the above capacitor size example shows that a very big capacitor with very low ESR is required inside each PC$_i$ of 3-ϕ MLC to save battery cells from significant additional losses and the accelerated capacity fading not only for low power factor but also for high power factor operation.

7 Conclusions

In this study we have theoretically established that the ripple current on the dc-link inside each PC$_i$ of 3-ϕ MLC is significantly high. Consequently, a large dc-link capacitor is required to filter the ripple. It does not seem practical to put such a big capacitor inside each PC$_i$ of MLC. We have also shown that in the absence of this capacitor, the battery will have to provide significant extra power per unit real power which would result in much higher additional ohmic losses and accelerated capacity fading compared to the case of 3-ϕ TLI especially for low power factor operation. Thus it is concluded that it is not feasible to use 3-ϕ MLC as an integrated cell balancer and a motor driver for 3-ϕ AC applications in xEVs unless, in addition to the dc-link capacitor, some other active filtering/compensation technique is used in order to reduce the size of the capacitor and/or the battery temperature. The alternative is to use single-phase MLC as a dedicated cell balancer inside a battery pack with 3-ϕ TLI at front as a dedicated 3-ϕ AC motor driver but such a solution does not seem cost-effective due to high component count.

8 Acknowledgments

References

[1] B. Kuhn, G. Pitel, and P. Krein, "Electrical properties and equalization of lithium-ion cells in automotive applications," in *Vehicle Power and Propulsion, 2005 IEEE Conference*, sept. 2005, p. 5 pp.

[2] C. Park and A. Jaura, "Dynamic thermal model of Li-Ion battery for predictive behavior in hybrid and fuel cell vehicles," *SAE transactions*, vol. 112, no. 3, pp. 1835–1842, 2003.

[3] W. C. Lee, D. Drury, and P. Mellor, "Comparison of passive cell balancing and active cell balancing for automotive batteries," in *Vehicle Power and Propulsion Conference (VPPC), 2011 IEEE*, sept. 2011, pp. 1 –7.

[4] P. Krein, "Battery management for maximum performance in plug-in electric and hybrid vehicles," in *Vehicle Power and Propulsion Conference, 2007. VPPC 2007. IEEE*, sept. 2007, pp. 2 –5.

[5] J. Rodriguez, L. Franquelo, S. Kouro, J. Leon, R. Portillo, M. Prats, and M. Perez, "Multilevel converters: An enabling technology for high-power applications," *Proceedings of the IEEE*, vol. 97, no. 11, pp. 1786 –1817, nov. 2009.

[6] L. Tolbert, F. Z. Peng, and T. Habetler, "Multilevel converters for large electric drives," *Industry Applications, IEEE Transactions on*, vol. 35, no. 1, pp. 36 –44, jan/feb 1999.

[7] O. Josefsson, A. Lindskog, S. Lundmark, and T. Thiringer, "Assessment of a multilevel converter for a PHEV charge and traction application," in *Electrical Machines (ICEM), 2010 XIX International Conference on*, sept. 2010, pp. 1 –6.

[8] F. Altaf, L. Johannesson, and B. Egardt, "Evaluating the potential for cell balancing using a cascaded multi-level converter using convex optimization," in *IFAC Workshop on Engine and Powertrain Control, Simulation and Modeling, 2012*, Oct. 2012.

[9] K. Wilkie, D. Stone, C. Bingham, and M. Foster, "Integrated multilevel converter and battery management," in *Power Electronics, Electrical Drives, Automation and Motion, 2008. SPEEDAM 2008. International Symposium on*, june 2008, pp. 756 –759.

[10] I. Bloom, B. Cole, J. Sohn, S. Jones, E. Polzin, V. Battaglia, G. Henriksen, C. Motloch, R. Richardson, T. Unkelhaeuser *et al.*, "An accelerated

calendar and cycle life study of li-ion cells," *Journal of Power Sources*, vol. 101, no. 2, pp. 238–247, 2001.

[11] B. McGrath and D. Holmes, "A general analytical method for calculating inverter dc-link current harmonics," *Industry Applications, IEEE Transactions on*, vol. 45, no. 5, pp. 1851 –1859, sept.-oct. 2009.

[12] D. Holmes and T. Lipo, *Pulse Width Modulation for Power Converters: Principles and Practice*, ser. IEEE Press Series on Power Engineering. John Wiley & Sons, 2003.

[13] H. Black, *Modulation theory*, ser. Bell Telephone Laboratories series. Van Nostrand, 1953.

[14] N. Mohan, T. M. Undeland, and W. P. Robbins, *Power Electronics: Converters, Applications, and Design*, 3rd ed. John Wiley & Sons; 2003, 2003.

[15] M. Rashid, *Power Electronics Handbook: Devices, Circuits, and Applications*, ser. Academic Press. Elsevier, 2010.

[16] J. Glover, M. Sarma, J. Mulukutla S. Sarma, and T. Overbye, *Power System Analysis and Design*. Thomson, 2008.

[17] A. Rabiei, T. Thiringer, and J. Lindberg, "Maximizing the energy efficiency of a pmsm for vehicular applications using an iron loss accounting optimization based on nonlinear programming," in *Electrical Machines (ICEM), 2012 XXth International Conference on*, sept. 2012, pp. 1001 –1007.

[18] H. Wen, W. Xiao, X. Wen, and P. Armstrong, "Analysis and evaluation of dc-link capacitors for high-power-density electric vehicle drive systems," *Vehicular Technology, IEEE Transactions on*, vol. 61, no. 7, pp. 2950 –2964, sept. 2012.